Czech Technical University in Prague
Faculty of Nuclear Sciences and Physical Engineering

Dissertation thesis

Positive ion extraction system design for the U-120M cyclotron

Prague 2023 Tomáš Matlocha

Bibliografický záznam

Autor	**Ing. Tomáš Matlocha** České vysoké učení technické v Praze, Fakulta jaderná a fyzikálně inženýrská, Katedra dozimetrie a aplikace ionizujícího záření Ústav jaderné fyziky AV ČR, v. v. i., Oddělení urychlovačů
Název práce	Návrh soustavy pro vývod kladných iontů z cyklotronu U-120M
Studijní program	Aplikace přírodních věd
Studijní obor	Jaderné inženýrství
Školitel	**Prof. Ing. Ladislav Musílek, CSc.** České vysoké učení technické v Praze, Fakulta jaderná a fyzikálně inženýrská, Katedra dozimetrie a aplikace ionizujícího záření
Školitel specialista	**Ing. Jan Štursa** Ústav jaderné fyziky AV ČR, v. v. i., Oddělení urychlovačů
Akademický rok	2022/2023
Počet stran	131
Klíčová slova	cyklotron, extrakční soustava, deflektor, magnetický kanál magnetické měření, simulace dynamiky urychlených částic

Bibliografic entry

Author	**Ing. Tomáš Matlocha** Czech Technical University in Prague, Faculty of Nuclear Sciences and Physical Engineering, Department of Dosimetry and Application of Ionizing Radiation Nuclear Pysics Institute of the CAS, Accelerators department
Title of Dissertation	Positive ion extraction system design for the U-120M cyclotron
Degree Programme	Applications of Natural Sciences
Field of Study	Nuclear Engineering
Supervisor	**Prof. Ing. Ladislav Musílek, CSc.** Czech Technical University in Prague, Faculty of Nuclear Sciences and Physical Engineering, Department of Dosimetry and Application of Ionizing Radiation
Supervisor specialist	**Ing. Jan Štursa** Nuclear Physics Institute of the CAS, Accelerators department
Academic Year	2022/2023
Number of Pages	131
Keywords	cyclotron, extraction system, deflector, magnetic channel magnetic field measurement, beam dynamics simulation

Abstrakt

Cílem této disertační práce je návrh nové extrakční soustavy pro vývod kladných iontů z cyklotronu U-120M. Za tímto účelem byla provedena přesná měření rozložení intenzity magnetického pole cyklotronu pomocí zrekonstruovaného aparátu, pro který autor této práce navrhl novou měřící část a napsal ovládací software. Autor dále provedl magnetická měření, na jejichž základě byla minimalizována porucha v magnetickém poli cyklotronu. Pro analýzu fungování původního extrakčního systému byl autorem vytvořen CAD model originálních extrakčních prvků a byla provedena simulace, která potvrdila nízkou účinnost této konfigurace. Pro novou extrakční soustavu autor navrhl nové vnější harmonické cívky, které byly v rámci odstávky urychlovače v roce 2022 nainstalovány do magnetického systému cyklotronu. Tyto cívky do značné míry kompenzují negativní vliv poruchové první harmonické složky magnetického pole a umožňují navýšení výstupní energie cyklotronu v režimu záporných iontů. Tyto cívky hrají také důležitou roli i v nově navržené extrakční soustavě pro kladné ionty, která nyní sestává ze dvou deflektorů a dvou magnetických kanálů. Tento systém vyžaduje nižší provozní napětí deflektorů oproti původnímu systému a umožňuje tak jejich dlouhodobý provoz i v protonovém režimu 36.7 MeV, kde původní extrakční soustava není použitelná. Práce také ukazuje možnost, jak zvýšit extrakční účinnost pro částice nižších energií vhodnou úpravou geometrie extrakčních elektrod, která může být s výhodou využita i v případě stávajícího extrakčního systému.

Abstract

The goal of this dissertation is the design of a new extraction system for the extraction of positive ions from the U-120M cyclotron. For this purpose, precise measurements of the distribution of the cyclotron's magnetic field were made using a reconstructed apparatus, for which the author of this work designed a new measuring part and wrote the control software. The author also performed magnetic measurements, based on which the disturbance amplitude in the magnetic field of the cyclotron was minimized. To analyze the operation of the original extraction system, the author created a CAD model of the original extraction elements and performed simulations that confirmed the low efficiency of this configuration. For the new extraction system, the author designed new external harmonic coils, which were installed in the magnetic system of the cyclotron during the accelerator shutdown in 2022. These coils largely compensate for the negative influence of the disturbed first harmonic component of the magnetic field and enable an increase in the output energy of the cyclotron in the negative ion mode. These coils also play an important role in the newly designed extraction system for positive ions, which now consists of two deflectors and two magnetic channels. This system requires a lower operating voltage of the deflectors compared to the original system and thus enables their long-term operation even in the proton mode of 36.7 MeV, where the original extraction system is not applicable. The work also shows the possibility of increasing the extraction efficiency for particles of lower energies by appropriate modification of the geometry of the extraction electrodes, which can be advantageously used even in the case of the existing extraction system.

Acknowledgment

I would like to express my deepest gratitude to my colleague Ing. Milan Čihák CSc. for invaluable discussions and moral support, without which this work would not have been possible.

Words cannot express my gratitude to my supervisor Prof. Ing. Ladislav Musílek, CSc. for his patience and academic guidance during the work.

I could not have undertaken this journey without the support of my supervisor specialist Ing. Jan Štursa, who created the conditions enabling the realization of this work.

I am extremely grateful to RNDr. Filip Křížek, Ph.D. for his stimulating comments and careful proofreading.

Many thanks belongs to all the colleagues from the accelerator department, whose continuous and diligent work enables the operation of the cyclotron.

This work is dedicated to my family
for their immense support

Contents

1 Introduction

This work aims to increase the efficiency of the extraction of positive ions from the isochronous cyclotron U-120M at the Nuclear Physics Institute in Řež near Prague. The efficiency of the currently used system depends on the specific operating mode of the cyclotron and varies in the range of 5–15% only. The prospect of future use of the accelerator for the production of positive ion beams is conditioned by the construction of a new system with significantly higher efficiency. The efficiency of the extraction largely depends on the design of the deflection system, which ensures the separation of the particle orbits at the final acceleration radii and the extraction of the beam from the accelerator space with a minimum of losses.

Although the primary consequence of the successful design of the new deflection system will be an increase in the maximum available flux of charged particles at the exit of the cyclotron, the side effect of reducing the transport losses of the accelerated beam is no less important. Losses of the positively charged particle beam occur mainly in the deflection system and then result in radioactive activation of the material. Thus another important side effect of the successful design will also be significant reduction in the radiation load of the operating personnel.

At the beginning of the work, it was known about the existence of a disturbance in the magnetic field of the U-120M cyclotron, which prevented acceleration to radii higher than 50 cm and significantly complicated the extraction of positive ions. Since the extraction of protons was only possible up to an energy of approximately 25 MeV, the goals of the thesis can be summarized as follows:

- confirm the presence of a cyclotron magnetic field disturbance by detailed magnetic field measurements,
- identify the cause of this disturbance and minimize its magnitude to an acceptable level,
- design such an extraction system that will be able to efficiently extract protons of the highest energies.

In the following paragraphs, the basic principles of cyclotron operation will be briefly described and an overview of phenomena that affect the properties of an accelerated beam of charged particles will be discussed. Chapter 2 deals with theory of beam extraction and overviews for recommended procedures for successful extraction of ions from the cyclotron magnetic field. In chapter 3, the individual technological blocks of the accelerator and the likely cause of a significant disturbance in the magnetic field will be briefly described together with the method of its minimization using detailed measurement of the magnetic field of the cyclotron. Chapter 4 presents software tools which were used to find the optimal design and analysis of the extraction system. The steps in preparing the configuration of the electromagnetic fields for simulations of the extraction process will be summarized in chapter 5. For a specific acceleration mode, losses in the central area

of the accelerator and during the extraction will be estimated. In the final chapter, the achieved results will be summarized, the limitation of their validity will be discussed and outlook for future work will be provided.

2 Theory of cyclotron operation

Over the course of more than ninety years of history, a cyclotron has evolved from a wax-sealed brass box [43], through high-end, large-scale scientific equipment [31, 12], to a regular part of every major hospital or research center [63]. Thousands of cyclotrons around the world are used every day to produce a number of different radionuclides for preparation of radio-pharmaceuticals [57], to irradiate patients as part of proton therapy, or for scientific experiments of various focuses. The cyclotron thus became a workhorse in the field of nuclear medicine and in fields using accelerated beams of charged particles.

A detailed overview of the characteristics and theoretical analysis of the cyclotron function can be found in the literature of the last century [42], from the latest publications it should be mentioned, for example [64], which solve practical tasks associated with the design of a cyclotron and the use of modern computer procedures.

2.1 Acceleration process

The cyclotron is a circular particle accelerator with a constant acceleration frequency and a stationary, spatially variable magnetic field. Acceleration occurs between the pole extensions of the electromagnet and the accelerated particles move along a trajectory similar to a spiral.

This work will be dealing with an isochronous cyclotron. This type of cyclotron, unlike the classical Lawrence-type cyclotron, compensates for the relativistic increase in the mass of the accelerated particle and thus enables significantly higher energies to be achieved. Although classical cyclotrons of the Lawrence type are used today rather exceptionally, in recent years there have been attempts to use them as cheap substitutes for isochronous cyclotrons for the production of radio-pharmaceuticals, e.g. for PET tomography, where low output energy is not a problem [25].

A particle with charge q and mass m, moving at a constant speed v in a homogeneous magnetic field with induction B, moves in this magnetic field along a circle with radius r. The centrifugal force mv^2/r acting on the particle is mediated by the Lorentz force qvB

$$\frac{mv^2}{r} = qvB. \tag{2.1}$$

Hence, the angular frequency of the particle ω will be equal to

$$\omega = \frac{v}{r} = \frac{qB}{m} \tag{2.2}$$

and will be independent of the radius and velocity of the particle. The angular frequency and therefore also the period of rotation depends only on the ratio of charge and mass of the particle q/m and on the magnitude of the magnetic field.

The function of the classical cyclotron, constructed by Lawrence and Livingston in 1932 at the University of Berkeley [40], is based on the above-mentioned principle. The acceleration takes place in a homogeneous circularly symmetrical magnetic field between

two hollow cylindrical electrodes, so called *dees*, to which a high-frequency voltage is applied. The frequency of the accelerating voltage ω_{RF} is related to the magnetic field according to the relation 2.2. The accelerated particles move in a spiral from the center of the accelerator so that their angular frequency ω and the frequency of the accelerating voltage ω_{RF} are the same

$$\omega = \omega_{RF}. \tag{2.3}$$

2.1.1 Particle stability

In a perfectly homogeneous magnetic field, the motion of particles is not vertically stable. A small initial component of the vertical velocity, which is always present, for example, due to the repulsive force of identically charged particles, causes the particle to sooner or later reach the wall of the dee and is lost for acceleration. The solution consists in the introduction of a magnetic field component that generates a force stabilizing the vertical movement of particles. If such a force exists, particles that deviated from the vertical direction are pushed back and perform harmonic oscillations around an equilibrium position. The equilibrium position are located at a closed circle in the magnetic field, the so-called *equlibrium orbit* or *closed orbit* and the oscillations around this equilibrium position are called *betatron* or forced *oscillations*. We distinguish between radial and axial betatron oscillations. The frequency of betatron oscillations can be expressed as their ratio to the basic circular frequency of the particle, i.e. in terms of the number of oscillations that the particle completes around its equilibrium orbit in one revolution. The betatron frequency is denoted in the literature by ν_r or Q_r for the frequency of radial oscillations and ν_z or Q_z for the frequency of axial oscillations. The situation is shown in Fig. 2.1, where r denotes the equilibrium orbit radius and x a deviation from it.

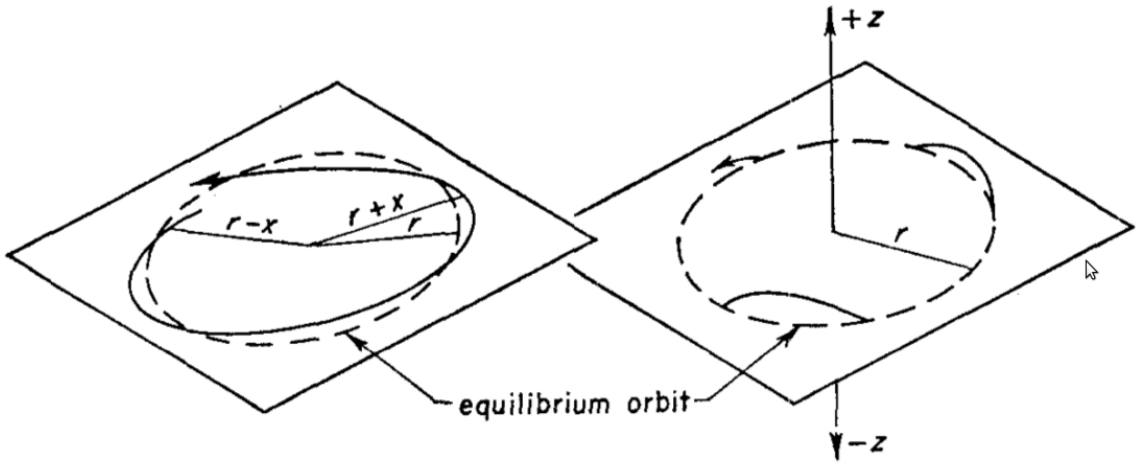

Figure 2.1: Representation of betatron oscillations around the equilibrium orbit. Reproduced from [42].

To investigate the stability of particles around an equilibrium orbit, the magnetic field index n is introduced, expressing the variation of the magnetic field B along the radius r

$$n = -\frac{\mathrm{d}B}{\mathrm{d}r}\frac{r}{B}. \tag{2.4}$$

In Ref. [42] it is shown that for a particle in a magnetic field, the axial stability is ensured for fields with the index $n > 0$ and the radial stability for fields with the index $n < 1$. Therefore, to ensure stability, the magnetic field must gradually decrease with increasing radius. In such a field, there is a radial component B_r, which generates a stabilizing force component F_z, always directed to the median plane between the poles of the magnet, and this is the principle of *weak focusing*. The magnetic field with the index $n > 0$ and the corresponding stabilizing force F are shown in Fig. 2.2.

According to [42], the following relations apply to the frequencies of betatron oscillations

$$\nu_z = \sqrt{n} \qquad \text{and} \qquad \nu_r = \sqrt{1-n}. \tag{2.5}$$

The movement of the particle in the horizontal and vertical planes can be expressed according to Ref. [14] as

$$x(t) = x_m \cos(\nu_r \omega_0 t), \tag{2.6}$$

$$z(t) = z_m \cos(\nu_z \omega_0 t), \tag{2.7}$$

where ω_0 is the angular frequency of the particle on the equilibrium orbit, r denotes the radius, and x_m and z_m are the amplitudes of oscillations in horizontal and vertical plane respectively.

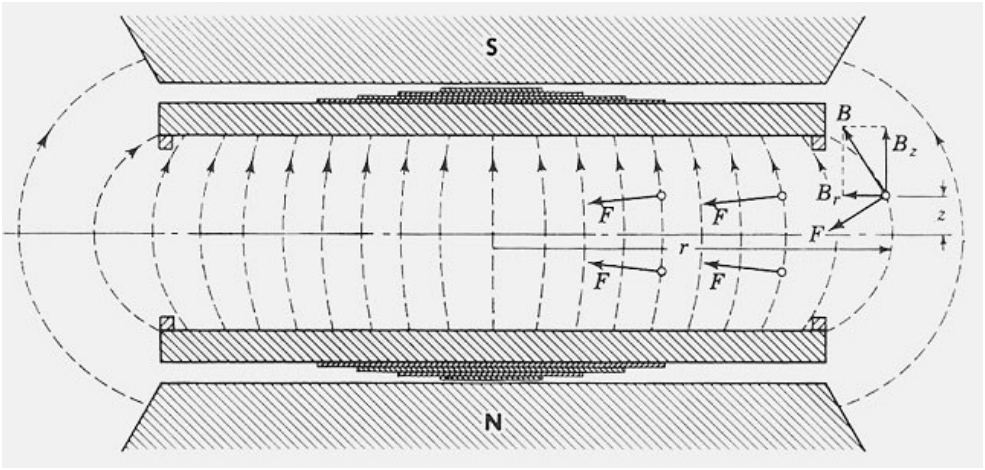

Figure 2.2: Illustration of the weak focusing principle. See text for further details. Reproduced from [59].

In a classical cyclotron, beam stability is achieved precisely by means of weak focusing. The maximum energy to which a classical cyclotron is able to accelerate particles is limited by the fact that if the speed of a particle v approaches the speed of light in vacuum c, its mass grows according to the relation $m = \gamma m_0$, where $\gamma = 1/\sqrt{1-(v/c)^2}$ and m_0 is the particle rest mass. The angular frequency of a particle in a homogeneous magnetic field will then not be constant, but it will be affected by the relativistic increase in mass according to the relation

$$\omega = \frac{qB}{m_0}\sqrt{1-\left(\frac{v}{c}\right)^2}. \tag{2.8}$$

With increasing energy, the particle begins to lag behind the accelerating voltage, its phase delay (*phase slip*) increases and the particle ceases to be synchronous. The phase

delay has a cumulative character and if it increases above the value $\pi/2$, the particle starts to be slowed down. This property limits the maximum energy achievable in a classical cyclotron to about 2% of its rest energy, which is about 18 MeV for protons. To achieve higher energies, it would be necessary to compensate for the relativistic increase in the mass of the particle by increasing the magnetic field radially. In this case, however, the value of the field index n according to (2.4) is negative, which violates the condition of axial stability.

The solution to this problem was proposed independently by V.Veksler [73] in 1944 and E.M.McMillan [49] in 1945 in the form of a synchrocyclotron. Its principle consists in gradually decreasing the frequency of the accelerating voltage ω_{RF} during acceleration such that the particle remains in phase with the accelerating voltage and the relation (2.3) is valid up to relativistic energies. For protons, the limit is about 1 GeV [78]. Unlike the classical cyclotron, the synchrocyclotron operates in a pulse acceleration mode and the intensity of the beam current is significantly lower. The axial stability of the beam is ensured in the same way as in the classical cyclotron by the radial decrease of the magnetic field, i.e. weak focusing. Veksler and McMillan have introduced also the principle of phase stability, which had a major influence on the expansion of the energy ranges achievable with circular accelerators.

Another solution enabling to achieve higher energies in a circular accelerator was proposed and published already in 1938 by L.H. Thomas [69]. His idea was to introduce an azimuthally varying magnetic field, or *AVF - azimuthally varying field*. The strong focusing properties of the azimuthally shaped field enable its radial increase and therefore the compensation of the relativistic increase in the mass of the accelerated particle while maintaining a constant frequency of the accelerating voltage. However, this method seemed mathematically too complicated for that time and was far ahead of the general understanding of the cyclotron problem. Thomas's solution thus remained unnoticed [42] for twelve years.

An azimuthally varying magnetic field is created between rotationally symmetric pole extensions of the magnet with alternately repeating regions with lower and higher profile. The areas with a smaller gap between the pole attachments, where the magnetic field intensity is higher, are called *hills* and areas with a larger gap and a lower magnetic field are called *valleys*. Accelerators with such a field profile are called *sector focused*. The particle orbits in such an azimuthally profiled field are no longer circular, but have a shape forced by the field of magnetic sectors. The particles acquire the radial component of the velocity v_r, which interacts with the azimuthal component of the magnetic field B_θ, and the resulting force acts on the particle in the direction to the midplane. This focusing power is independent of the radial gradient of the field and is unrelated to the weak focusing. The focusing properties of the azimuthally varying field are further enhanced if the sectors have a spiral shape [64]. A computer model of a spiral sector cyclotron together with its magnetic field is shown in Fig. 2.3.

The degree of azimuthal variation of the magnetic field $F(r)$, so-called *Flutter*, can be expressed as a function of the radius as the amplitude of the deviation of the field from the mean field at a specific radius

$$F(r) = \frac{\overline{B(r)^2} - (\overline{B(r)})^2}{(\overline{B(r)})^2}, \tag{2.9}$$

where $\overline{B}$ expresses the mean value of the field averaged over azimuth 0 – 360° and $\overline{B^2}$ expresses the mean value of the square of this field. The magnetic field in the median

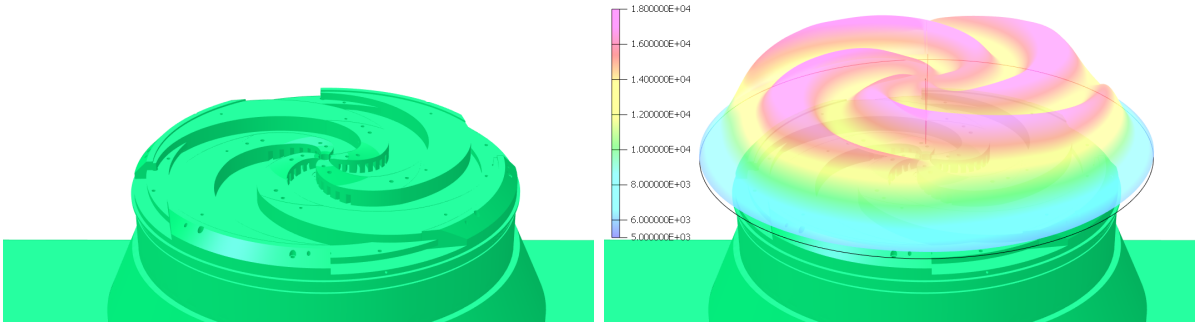

(a) CAD model. (b) Magnetic field. The color scale is in Gauss.

Figure 2.3: U-120M cyclotron 3D Opera [66] model and its simulated magnetic field.

plane can be represented by decomposition into Fourier components A_n and B_n

$$B(r,\theta) = \overline{B}\left[1 + \sum_{n=1}^{\infty} A_n(r)\cos n\theta + B_n(r)\sin n\theta\right], \tag{2.10}$$

where $B(r,\theta)$ is the magnetic field in the midplane at radius r and azimuth θ. Flutter F can then be expressed using these components as

$$F = \sum_{n=1}^{\infty} \frac{A_n^2 + B_n^2}{2}. \tag{2.11}$$

For the magnetic field with azimuthal variation, radial dependence of the corresponding mean field can be characterized analogously to Eq. 2.4 by introduction index k and expressing in terms of the mean value of the field at the radius $\overline{B}$ as

$$k = \frac{\mathrm{d}\overline{B}}{\mathrm{d}r}\frac{r}{\overline{B}}. \tag{2.12}$$

Another important parameter which is used to describe geometry of the magnetic field in cyclotrons with spiral-shaped sectors is the degree of spirality ξ. Fig. 2.4 shows that ξ characterizes curvature of the spiral sectors edges

$$\tan\xi = r\frac{\mathrm{d}\psi}{\mathrm{d}r}. \tag{2.13}$$

According to Ref. [78], the frequency of radial and axial betatron oscillations can be expressed using the field index k, the periodicity of the structure N, the flutter F and the spirality angle ξ as

$$\nu_z^2 = k + \frac{N^2}{N^2-1}F(1+2\tan^2\xi), \tag{2.14}$$

$$\nu_r^2 = (1-k) + \frac{3N^2}{(N^2-1)(N^2-4)}F(1+2\tan^2\xi). \tag{2.15}$$

The cyclotron magnetic field can be considered isochronous if the the field index fulfils

$$k = \frac{\beta^2}{1-\beta^2}, \tag{2.16}$$

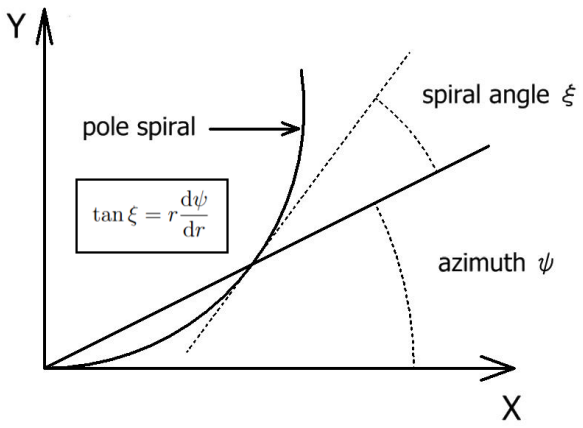

Figure 2.4: Spiral angle ξ definition.

where $\beta = v/c$.

An example of the mean isochronous magnetic field of the cyclotron U-120M for several particle species is shown in Fig. 3.7.

2.1.2 Resonances

The horizontal and vertical betatron oscillations of the orbiting beam are not fully independent of each other. During the acceleration, the beam passes through regions of integer and parametric resonances, during which the amplitude of oscillations can be transferred from one type of oscillation to another and vice versa [42]. Resonances can have a significant effect on the vertical dimension of the beam, which can result in losses of the beam on the upper and lower walls of the dees, or on the position of the center of the orbits. For example, if ν_r is very close to 1 after a significant number of turns, any imperfection in the magnetic field has a cumulative effect and the center of the orbit moves independently of the center of the magnetic field, again leading to beam losses. To limit the negative influence of these resonances on beam stability, it is necessary to ensure a fast transition of betatron frequencies through the critical region. The resonances $\nu_z = 0.5$ and $\nu_r = 2\nu_z$ are significantly unfavorable. For cyclotrons of relativistic energies, it is also resonances $\nu_z = 2/2$ and $\nu_z = 1$.

2.1.3 Basic beam parameters

The horizontal and vertical distribution of the beam is described by the emittance surfaces A_x and A_y in the phase space [76] with axes x_m, x'_m and z_m, z'_m, where x'_m and z'_m are the divergences of the particle relative to the reference particle in the center of the beam, which we obtain by making a derivative of the equations (2.6) and (2.7) by traverse particle path s

$$x'(t) = \frac{\mathrm{d}x}{\mathrm{d}s} = \frac{\mathrm{d}x}{r\omega_0 \mathrm{d}t} = -\frac{x_m \nu_r}{r}\sin(\nu_r \omega_0 t), \tag{2.17}$$

$$z'(t) = -\frac{z_m \nu_z}{r}\sin(\nu_z \omega_0 t), \tag{2.18}$$

where ω_0 is the angular frequency of the particle in a closed orbit, r is the radius. The amplitudes of oscillations in horizontal and vertical plane are denoted x_m and z_m, respec-

tively. The divergences x'_m and z'_m are measured in mrad. Provided that energy of the beam is not increased by acceleration the emittance areas $A_x = \pi x_m x'_m = \pi x_m^2 \nu_r / r$ and $A_z = \pi z_m z'_m = \pi z_m^2 \nu_z / r$ remain constant.

The transverse dimensions of the beam can also be described using a periodic function $\beta(s)$, representing the dimension of the envelope of the beam at a specific point along the trajectory of the particle. The beta function describes the focusing properties of the field [29]. Amplitude of the oscillations can be expressed as

$$x_m(s) = \sqrt{\varepsilon}\sqrt{\beta(s)}, \tag{2.19}$$

where beam emittance ε equals

$$\varepsilon = \gamma(s)x^2(s) + 2\alpha(s)x(s)x'(s) + \beta(s)x'^2(s). \tag{2.20}$$

Here

$$\alpha(s) = -\frac{1}{2}\beta'(s), \tag{2.21}$$

$$\gamma(s) = \frac{1+\alpha^2(s)}{\beta(s)}. \tag{2.22}$$

The parameters α, β, γ are so-called Twiss parameters and their relation to the dimensions of the phase ellipse is illustrated in Fig. 2.5.

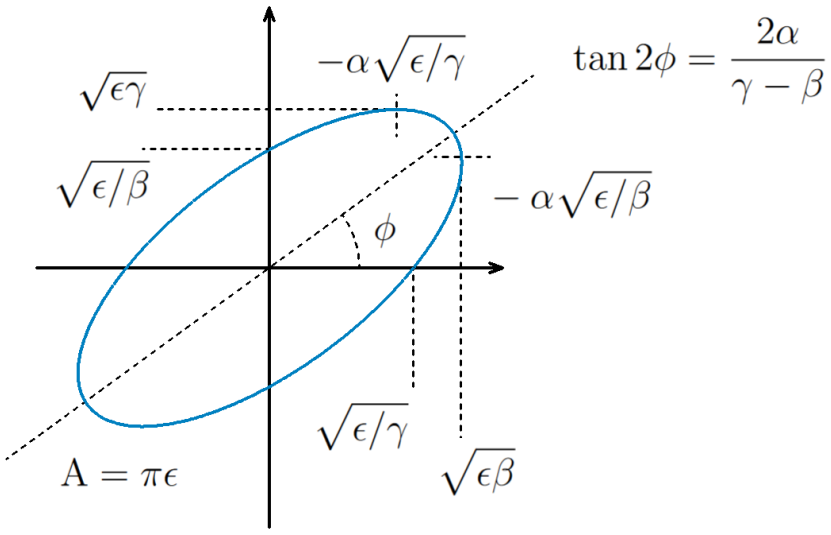

Figure 2.5: Determination of Twiss parameters from the dimensions of an ellipse with area A in the phase plane.

To describe the beam without the effect of acceleration, it is advantageous to introduce normalized emittances

$$\varepsilon_x = \beta\gamma A_x = \pi\frac{\omega}{c}\gamma x_m^2 \nu_r = \text{constant}, \tag{2.23}$$

$$\varepsilon_z = \beta\gamma A_z = \pi\frac{\omega}{c}\gamma z_m^2 \nu_z = \text{constant}, \tag{2.24}$$

where ν_r and ν_z are the frequencies of betatron oscillations, γ is Lorentz factor, $\beta = v/c$ and ω denotes the angular frequency of the particle.

To express the size of the beam, we assume a Gaussian distribution and measure the dimension of two standard deviations 2σ in three-dimensional space as the volume containing 95% of the particles, for further detail see [79, 14].

2.1.4 First harmonic component

For the correct reading of the graphs of the first harmonic component of the magnetic field presented in this work, it is necessary to mention the calculation of the amplitude values of the harmonic components of the magnetic field.

According to Eq. 2.10, the magnetic field can be described using Fourier components

$$B(r,\theta) = \overline{B} + \sum_{n=1}^{\infty} B_n(r)\cos(n\theta - \varphi_n(r)), \tag{2.25}$$

where

$$B_n(r)\cos(n\theta - \varphi_n(r)) \tag{2.26}$$

is n$^{\text{th}}$ harmonic of the magnetic field at certain radius r. B_n is the harmonic's amplitude and φ_n is its phase shift on the radius.

Fig. 2.6 shows the signals of the first and fourth harmonic components and their superposition. The first cosine signal representing the first harmonic component with the amplitude 0.5, the second signal is the fourth harmonic component cosine signal with the amplitude 1. The resulting signal is a superposition of both signals.

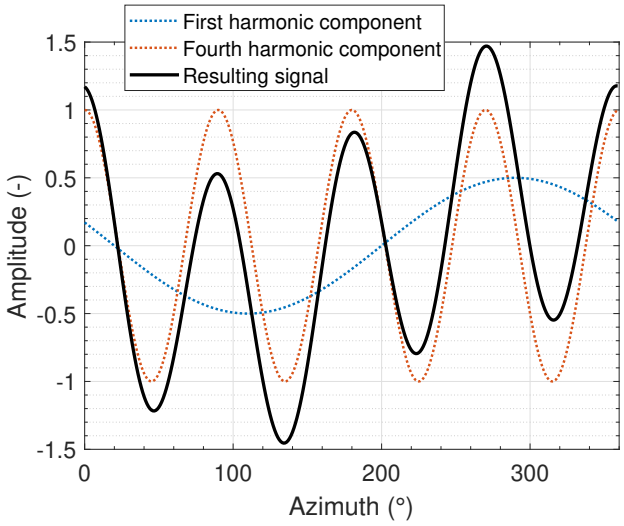

Figure 2.6: Superposition of the first harmonic component and the fourth harmonic component of an arbitrary signal.

In the case of a cyclotron with four-fold rotational symmetry, i.e the magnetic system periodicity, the fourth harmonic component is the main work component with the amplitude of several thousand Gauss (in case of the U-120M cyclotron) and the first harmonic component is introduced as a perturbation. The calculation is performed by decomposing the magnetic field over the entire azimuth at one radius into the Fourier components of

the signal using a fast Fourier transform (FFT) algorithm implemented in Matlab [46]. For each radius, each of the harmonic components has one amplitude. By summing all the harmonic components at one radius, we obtain the resulting azimuthal course of the magnetic field at this radius.

By increasing the amplitude of the first harmonic component the quality of the acceleration process deteriorates. The beam center shift occurs leading to increase of the amplitude of coherent oscillations and related increase of the beam radial size. Ideally, the first harmonic component should be close to zero and well below 1-2 Gauss.

2.2 Beam extraction methods

The theory of ion extraction from the cyclotron acceleration space was investigated in detail in the second half of the last century [1, 44, 54, 34]. It is an important and complex part of the process of obtaining beam of charged particles, the purpose of which is, on the one hand, to transport the beam of given parameters to the area of its intended interaction in the experiment and, on the other hand, to minimize the consequences of unwanted losses in the space of the accelerator.

Losses at the end of the acceleration process, when the energy of the accelerated particles is the highest, are accompanied by the greatest difficulties. As a result of the nuclear interactions of the beam with the impacted material, the accelerator components are radioactively activated, which significantly complicates their handling and maintenance. Due to the high energy density of the beam scattered over a small area, mechanical damage to the accelerator often occurs. For cyclotrons with lower energies, the activation of components can be limited by using suitable materials so that the product of nuclear reactions are short-lived nuclides. However, it is not always possible to use such materials from a technological point of view, and there is usually no such possibility when dealing with high energy beams. Heat removal from a narrowly localized area is also quite problematic. Thus, the optimal solution is to keep the beam losses at the lowest possible level. Both for high-energy cyclotrons and for high-current cyclotrons at lower energies, the efficiency of the beam extraction is therefore one of the key parameters.

2.2.1 Extraction by stripping

The vast majority of newly constructed cyclotrons are commercial devices for the production of radio-pharmaceuticals with energies up to 30 MeV. These cyclotrons accelerate beams of negative hydrogen ions H^- and are intended for the production of radionuclides for diagnostic examinations in radiology and PET tomography. Globally, cyclotrons account for 95 % of the production of radio-pharmaceuticals used in PET [57]. With a great advantage, they use the acceleration of negative ions, which provides the possibility of extraction by the method of charge conversion, the so-called *charge stripping* [36].

When the H^- ion passes through a thin stripping foil, usually pyrolytic carbon with a thickness of approximately 1 μm [77], orbital electrons are lost and the electric charge of the ion is reversed. After the conversion, the positive ion in the magnetic field of the accelerator has the opposite sense of rotation and is taken out of the acceleration space by means of the Lorentz force. The maximum beam energy is determined by the radius of the last orbit in the accelerator and the energy of the accelerated beam can only be changed by a suitable radial position of the conversion foil. The stripping method can be used for beams with current intensities up to about 500 μA. At the same time, it

is also possible to use several foils at different azimuths and to irradiate two or more targets at the same time. This is advantageous for maximum use of the accelerator in the commercial production of radio-pharmaceuticals [78].

The foil method is also very effective for heavier ions extraction. It is no longer a charge conversion, but an increase in the degree of ionization of partially ionized ions. After passing through the foil, they lose the remaining electrons from the shell and thus acquire a higher charge. In a magnetic field, the direction of rotation remains unchanged, but the curvature radius is reduced. After one or more revolutions, the ions leave the accelerator space along a pre-defined path [36].

2.2.2 Positive beams extraction

The situation is somewhat more complicated for ions with a full degree of ionization, for which the radius of gyration can no longer be changed, which is the case of the U-120M isochronous cyclotron. During the extraction process, it is necessary to ensure that the extracted beam is separated from the last acceleration orbit and diverted from the acceleration process with maximum efficiency. At the same time the extraction process should affect the accelerated beam as low as possible. A combination of stationary electric and magnetic fields is used to deflect the extracted beam and resonant and non-resonant concepts are used [36, 28]. An electrostatic extraction electrode – deflector – is used in the vast majority of cases to separate the extracted part of the beam at the beginning of the extraction process. To increase the extraction efficiency, it is advisable to increase the distance between the individual orbits at its entrance through the separation of orbits. An increase in the distance between the orbits can be achieved either by increasing the gain in energy per turn, the so-called *extraction by acceleration*, or by appropriately introduced disturbances in the magnetic field, the so-called *magnetic bumps*, which will excite suitable orbital resonances, or by a combination of both. Both integer and half-integer resonances are used, in which case it is the *resonance extraction* method.

2.2.3 Extraction by acceleration

This is a basic method for the extraction of positive ions, when a suitable separation of orbits is achieved only by an increase in energy during one revolution, or by an increase in energy in combination with a local disturbance of the magnetic field. The radial increment R per revolution n can be expressed as

$$\frac{\mathrm{d}R}{\mathrm{d}n} = \frac{\mathrm{d}R}{\mathrm{d}n}\ (\text{acceleration}) + \frac{\mathrm{d}R}{\mathrm{d}n}\ (\text{disturbance}). \tag{2.27}$$

According to [36, 28], the first term on the right hand side of 2.27 can be expressed as

$$\frac{\mathrm{d}R}{\mathrm{d}n}\ (\text{acceleration}) = R_a \cdot \frac{E_g}{E} \cdot \frac{\gamma}{\gamma+1} \cdot \frac{1}{{\nu_r}^2}, \tag{2.28}$$

where R_a is the average orbital radius, E_g the increment of kinetic energy per revolution n, E the kinetic energy, $\gamma = 1 + E/E_0$ the relativistic factor and ν_r the radial betatron frequency. The equation (2.28) states that in general, extraction efficiency can be increased in three ways

1. construction of a cyclotron with a large radius,

2. by increasing the energy increment by turn,

3. by accelerating into the fringe field region, where ν_r decreases.

By constructing a cyclotron with a large radius and a proportionally lower maximum magnetic field for the same output energy, a greater distance between the orbits can be achieved, but this method is not very economical. Increasing the energy gain per turn E_g is mostly possible only in cyclotrons with separate resonance structures. Most cyclotrons have accelerating electrodes located inside their magnetic structures and they usually operate at the limits of their power capabilities or electrical strength limits. In case of the third option, acceleration into the area of the fringe field results in a considerable shift of the phase of the accelerated beam, which can be limited by increasing the E_g again. In all three cases, there are practical limitations to their application and a choice of compromise is necessary. The only type of cyclotron that allows all three conditions to be realized simultaneously and thus appears to be structurally ideal is the *Ring* type cyclotron designed in 1963 by H.A. Willax [80]. It is a cyclotron with separate sectors and separate resonance systems. One of the cyclotrons of this type is located at the Swiss institute PSI [31] and accelerates protons to an energy of 590 MeV at an extraction efficiency of 99.98% with a maximum mean current of 2.4 mA and a beam power of 1.4 MW.

2.2.4 Resonance methods

Sufficient energy increment per revolution, required for effective extraction, cannot be ensured in most cyclotrons. For this reason, in order to increase the separation of the orbits at the extraction radius, appropriately selected disturbances of the magnetic field stimulating the resonances of betatron oscillations are introduced into the magnetic field of the cyclotron. These are divided into two basic types: integer and half-integer resonances.

Integer resonances $\nu_r = N$

The two basic types of extraction are used for integer resonances, the *Brute force* method, and the *Precession* method [36, 28].

Brute force method:

If we introduce a localized perturbation into the axial component of the magnetic field

$$\Delta B_z(R, \theta) = b_N \cos[N(\theta - \theta_N)], \tag{2.29}$$

where R is the radius, θ is the azimuth and b_N is the amplitude of the N-th harmonic component of the magnetic field, in the region where the betatron frequency ν_r is close to one, the beam shifts off the center. The maximum radial increment due to the disturbance field is

$$\frac{\mathrm{d}R}{\mathrm{d}n} = \pi R \frac{b_N}{N B_0}, \tag{2.30}$$

where B_0 is the mean value of the magnetic field at the radius R. The U–120M cyclotron has a mean field of $B_0 = 1.8\,\mathrm{T}$ at the extraction position of 507 mm and the introduced disturbance amplitude $b_1 = 1\,\mathrm{G}$ (0.1 mT). This yields $\mathrm{d}R/\mathrm{d}n = 0.1\,\mathrm{mm}$. This method is currently the only method used on the U-120M cyclotron and the electromagnetic exciter described in section 5.1.1 is used to produce the magnetic field bump.

Precession method:

For greater separation of orbits by the Brute force method, the amplitude of the introduced disturbance must be proportionally increased. For cyclotrons, where ν_r decreases slowly, there is an elegant method [36]. Oscillations with a coherent amplitude x_c are excited when the beam passes through the resonance region $\nu_r = 1$

$$x_c = \pi\, R\, \frac{1}{B_0}\, n_{\text{eff}}, \qquad \text{where} \qquad n_{\text{eff}} = \frac{1}{\sqrt{\left|\frac{\mathrm{d}\nu_r}{\mathrm{d}n}\right|}}. \tag{2.31}$$

Here the ratio $\mathrm{d}\nu_r/\mathrm{d}n$ expresses the rate of change of ν_r in the resonance passage area and n_{eff} expresses its duration. The value of n_{eff} is usually around ten turns. After passing through the resonance, the beam performs precession oscillations around the equilibrium position with a frequency of $\nu_r - 1$. The maximum radial increment by the precession method is

$$\frac{\mathrm{d}R}{\mathrm{d}n} = \pi\, x_c\, \sin[\pi(1-\nu_r)]. \tag{2.32}$$

Since phase losses of the beam occur due to the loss of isochronism, this method finds its application especially in cyclotrons with a high increase in energy per turn, where it is possible to accelerate the beam up to the region of the fringe field, where ν_r is significantly lower than one.

Half integer resonances $\nu_r = N$

If we supplement the magnetic field disturbance introduced by 2.29 at the radius R_N with a radial gradient g_N

$$\Delta B_z(R,\theta) = g_N\,(R - R_N)\,\cos[N(\theta - \theta_N)], \tag{2.33}$$

this perturbation acquires focusing properties and also changes the frequency of radial betatron oscillations. Vogt-Nilsen [75] derived a relation for the change in radial frequency $\nu_r \rightarrow \tilde{\nu_r}$ and showed that the largest change in the frequency occurs for $\nu_r \sim N/2$. In the narrow range $\nu_r = N/2 + \Delta\nu_r$ there is a forbidden band, the so-called *stop band*, in which the betatron frequency $\tilde{\nu_r}$ acquires complex values and the beam is unstable . This radial instability can be utilized for the extraction. For the half-width of the forbidden region $\Delta\nu_r$, it holds

$$\Delta\nu_r = \frac{R\, g_N}{2N\, B_0}, \tag{2.34}$$

where B_0 is the mean magnetic field at the radius R with the gradient of the Nth harmonic component g_N. Cyclotrons with energies up to about 100 MeV have a value of ν_r close to 1, and the resonance $\nu_r = 2/2$ can be used for the extraction. For high-energy cyclotrons, ν_r does not even come close to one in the extraction area, so the resonance $\nu_r = 3/2$ or $\nu_r = 4/2$ has to be used. The method is called *regenerative*, since a combination of *peeler – regenerator* coils, offset azimuthally by 90°, is used to excite the desired disturbance. It did not find greater application in isochronous cyclotrons working at lower energies, since better results can be achieved using the precession method. However, this method can be used in the installation of relativistic cyclotrons, where it is very effective [36]. This method is also of high importance in synchrocyclotrons, where the radial increments due to acceleration thanks to the low amplitude of the accelerating voltage are much smaller than the amplitudes of betatron oscillations.

3 Cyclotron U-120M

The cyclotron U-120M [37] was built in Joint Institute of Nuclear Research in Dubna in 1976. It is a variable energy multi-particle isochronous cyclotron which design is based on its predecessor – the classical cyclotron U-120. The modernization consisted in the creation of a spatial variation of the magnetic field enabling to exceed the relativistic energy limit of the classical cyclotron. Main parameters of the cyclotron are listed in Tab. 3.1.

The cyclotron magnetic system is designed to create an isochronous magnetic field for particles with mass to charge ratio A/Z equals to 2 or lower. The cyclotron facility enables the acceleration of ions in the range of energies listed in Tab. 3.2, where the values in parentheses indicate the energy achievable in relation to the limitations given by the current extraction system. The maximum proton energy achievable at the cyclotron is 37 MeV. In fact, the designed cyclotron limit is 40 MeV, but due to the impossibility of retuning the RF resonant system to the highest frequency, this value is not currently available.

Table 3.1: U-120M main parameters.

Pole diameter	120 cm
Average magnetic field	0.7 – 1.8 T
Magnetic field periodicity	4
No. of trim coils	18
No. of harmonic coils	8 pairs
Vertical gap dimension in magnetic hill	8.2 cm
Vertical gap dimension in magnetic valley	22 cm
Type of sectors	Spiral
Average sector spirality	4.5 cm
Dee voltage	35 kV
RF system frequency	8.5 – 26 MHz
RF power	250 kW
Number of dees	1
Dee angle	180°
Dee aperture	18 mm
Extraction radius	$\sim$ 50 cm
Total weight	150 t

Table 3.2: Actual ion types and energy ranges for external delivery at U-120M. Values in brackets indicate the maximal energy achievable with the current extraction system. Data taken from [24].

Ion type	Minimal energy (MeV)	Maximal energy (MeV)
Protons / H^-	6	(25) 37 / 37
$^4He^{2+}$	12	(38) 40
$^3He^{2+}$	17	(52) 55
Deuterons / D^-	12 / 11	20

3.1 Cyclotron layout

The geometry of the U-120M cyclotron facility consists of a magnetic system providing a magnetic field in the accelerating region, a RF resonator providing accelerating electric field and a vacuum chamber allowing acceleration in a high vacuum environment. The vacuum chamber itself is placed between the magnet poles and shares the vacuum with the RF resonator. Internal beam intensities are measured by current probes No. 1,2 and 3 placed at azimuth 90°, 210° and 300°. The intensity of the extracted beam in the positive mode is measured by a probe No. 4 placed at 0°. The probes No. 1 to 3 cover a position range from the very center to the chamber boundary, the probe No. 4 has a limited range covering only the extracted beam radius. The situation is schematically shown in Fig. 3.1, where the y axis of the coordinate system is aligned with the dee central line.

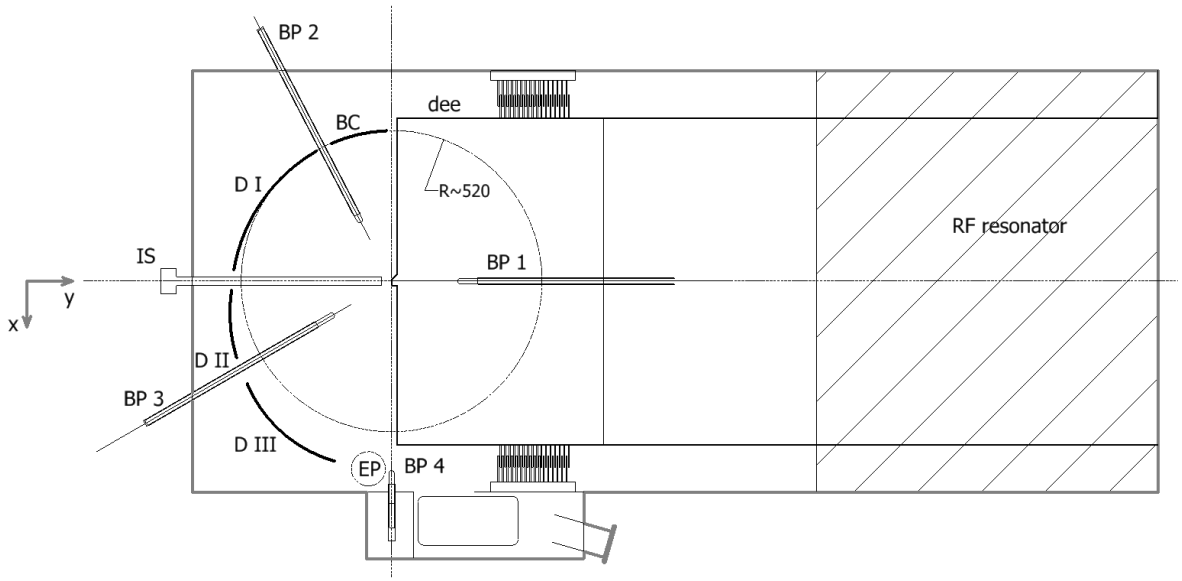

Figure 3.1: Schematic top view drawing of the cyclotron median plane layout. BP 1–4 - beam probes, D I–III - electrostatic deflectors, BC - electromagnetic exciter, IS - ion source, EP - extraction point.

3.1.1 RF system

The RF resonant system of the cyclotron is designed as a quarter-wave resonator tunable in a wide range of working frequencies. Rough tuning of frequencies in the 9–26 MHz range

is achieved by changing the impedance of the input part of the resonator using movable panels. The high-frequency generator is connected to the resonance system using an inductive loop located in the area of the tuning panels. Two sets of capacity trimmers are used for the frequency fine-tuning. Trimmers for coarse tuning are made in pairs and are placed in the space of the acceleration chamber at the dee end of the resonance line. The trimmers for fine frequency change are located in the area of adjustable panels.

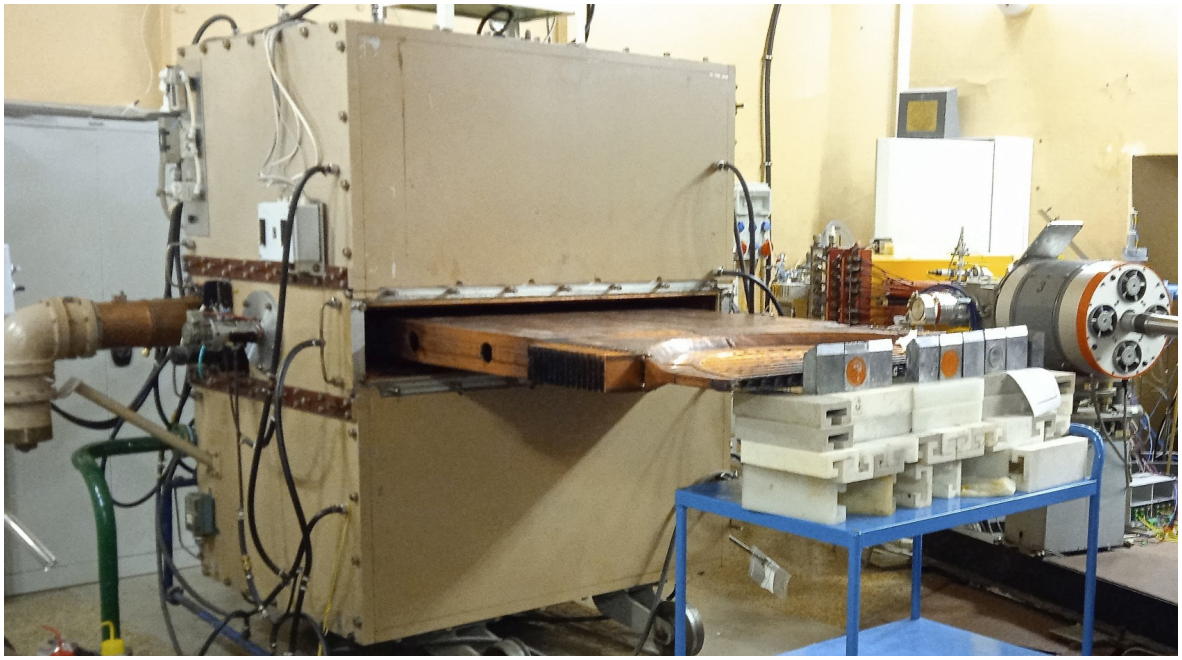

Figure 3.2: RF resonator with the dee taken out from the accelerating chamber.

3.1.2 Ion source

Although the U-120M cyclotron has the option of using an external ion source and vertical beam injection into the central region of the cyclotron, currently only an internal ion source located in the accelerator chamber is used. The internal ion source shown in Fig. 3.3 is a Penning type (PIG) with a cold cathode. During the experiments connected with the radiation hardness tests of the detectors for the ALICE experiment at the LHC, it was possible to significantly extend the working range of the PIG ion source. Currently, in addition to the classic PIG discharge mode, the source can also be used in a glow discharge mode. Thanks to this mode, it was possible to expand the range of output currents of the cyclotron by about eight orders of magnitude. The output current in the regime, which accelerates negative hydrogen ions, can be continuously regulated from a value of approximately 100 protons/s/cm^2 to a value of approximately 10^{16} protons/s/cm^2. The lowest achieved flux from a cyclotron where it is still possible to control its properties is slightly below the level of 1 proton/s/cm^2 [48]. During experiments with very small currents, we discovered an interesting property of the accelerator in our cyclotron laboratory. When the accelerating voltage is applied and the magnetic field is switched on, the accelerator produces a proton flux in the order of thousands of protons per second even when the ion source is completely switched off. This phenomenon is caused by the emission stimulated by the electric field between the body of the PIG ion source and the puller – the dee extraction tip. This feature is probably shared by most similarly constructed cyclotrons,

however, due to the intensity of the flux, this phenomenon is below the detection capability of most common measuring devices. A more detailed description of the properties of the ion source and its operating modes can be found in articles [37] and [47].

Figure 3.3: Internal U-120M PIG ion source.

3.1.3 Vacuum chamber

The vacuum acceleration chamber has a rectangular shape and is made of alumina walls with thickness of 40 mm. The top and the bottom cover of the vacuum chamber is attached from three sides to the side plates. The fourth side of the chamber is missing and serves as a feed-through for the RF line. Due to the one missing side wall, the chamber can be deformed on the open side by a force induced by the pressure gradient. This deformation introduces an uncertainty in magnetic field configuration and complicates operation at the lowest particle energies. This issue is discussed in more detail in a dedicated section 3.3. A cross-section of the vacuum chamber placed between the magnet poles is shown in Fig. 3.4. The transition of the magnet pole to the magnetic structure placed in the vacuum chamber is shown in detail in Fig. 3.5.

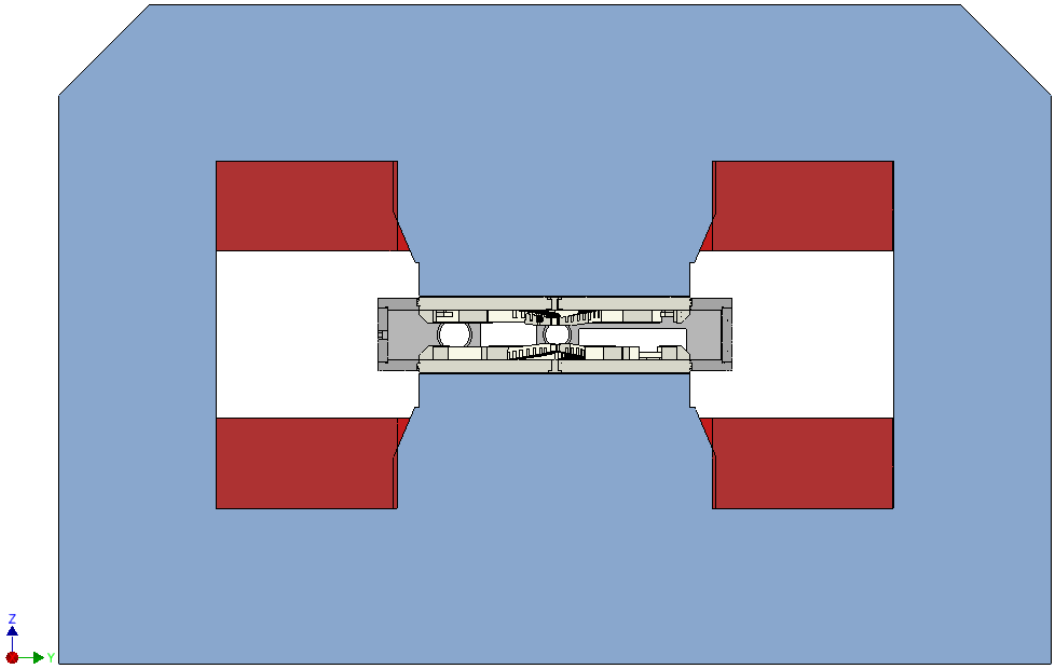

Figure 3.4: A cross-section of the cyclotron magnet (blue), main coils (red) and chamber (gray), iron spirals on the support (light yellow), dee is not shown. See text for further details.

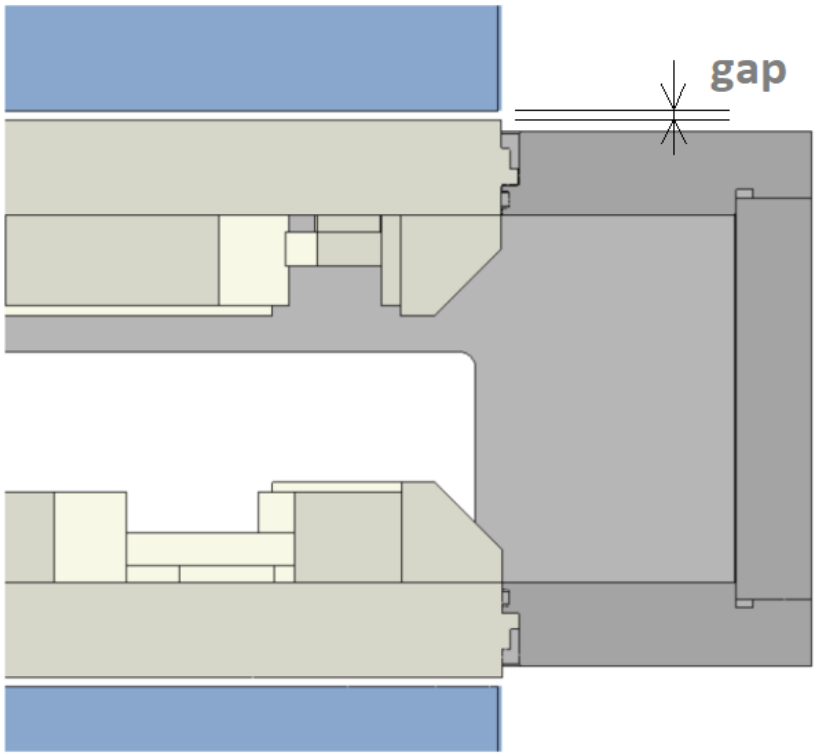

Figure 3.5: Accelerating chamber cross-section detail – magnet pole (blue), sectors and iron sectors support (light yellow), and the chamber (grey). Between the chamber and the sectors support is the high reluctance gap.

3.2 Magnetic system

The resulting magnetic field is formed by the contribution from the main magnet by the magnetization of the iron spiral sectors and the contribution from the correction coils. The spiral sectors form a spatial magnetic field ensuring vertical focusing. The correction coils fine-tune the resulting field to fulfill the isochronism condition. The quality of the beam horizontal centering is ensured by four pairs of internal harmonic coils. Fig. 3.6 shows the amplitudes of radial and vertical betatron oscillation for the particles specified in Table 3.2 at their maximal energies – the so-called tune diagram. Energy values for individual ions are marked at orbits where ν_r=1.

Based on information from [5], the magnetic system was designed to ensure the following cyclotron properties:

- a possibility of axial injection of the beam from an external ion source,
- minimal trim coils current amplitudes for the formation of the isochronous field,
- sufficiently low amplitude of the fourth harmonic component of the magnetic field and low amplitude of vertical betatron oscillations ν_z for low field levels.

3.2.1 Main magnet

The basic magnetic field, i.e. the field formed by iron spiral sectors, is generated using the main coil in the current range of 100 – 650 A corresponding to a mean magnetic field range 0.7 – 1.8 Tesla.

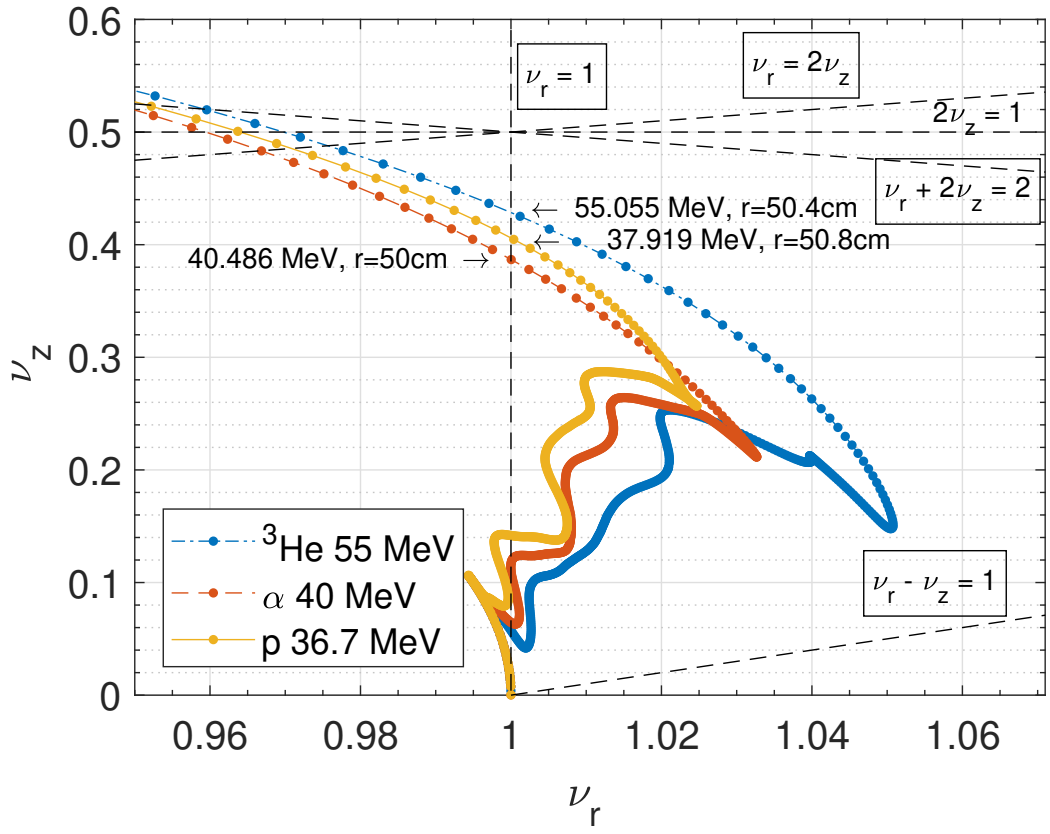

Figure 3.6: U-120M tune diagram for protons, ^{3}He and α ions for their maximal energy mode. Dangerous resonances are highlighted with a dashed line.

The basic magnetic field without the trim coils is designed to be close to isochronous field for $^3He^{2+}$ in case that the main excitation current is 500 A. At this configuration the necessary correction using the trim coils is minimal. The radial profiles of the mean isochronous magnetic fields for the utilized ions and the field without trim coils for the main coil current of about 500 A are shown in Fig. 3.7.

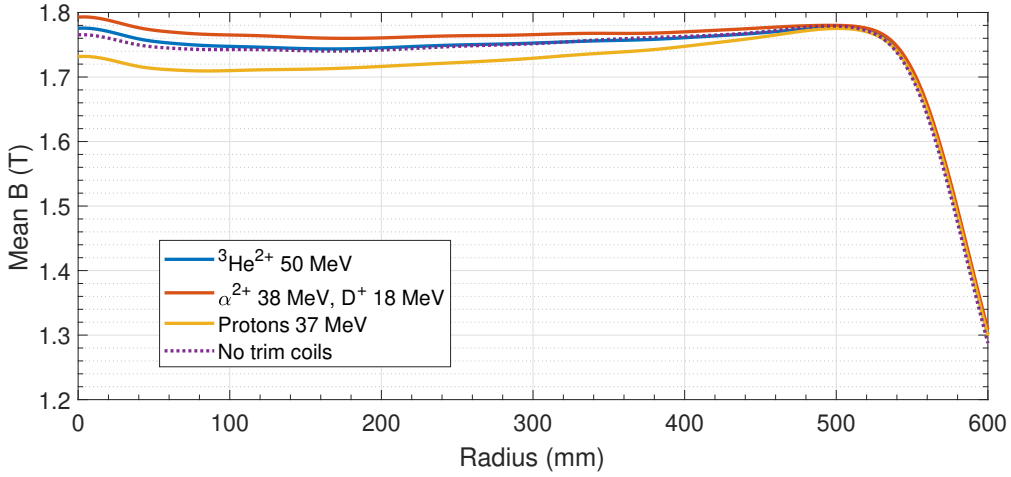

Figure 3.7: Mean isochronous magnetic field along radius for various ions compared with a field without the trim coils for the main coil current of about 500 A.

3.2.2 Spiral sectors

According to Ref. [3] the azimuthal width of the spiral sectors, their distance and height change according to the requirements for the course of spatial variation and the dependence of the mean field on the radius. From the arrangement of the elements of the magnetic system in Fig. 3.8, it can be seen that the spiral sectors are divided into three parts:

- central part – boundaries are formed by spirals close to the Archimedean spiral $r = 18\,\varphi$,
- middle part – boundaries are formed by a section of off-center circles,
- peripheral part – boundaries are formed by a section of off-center circles and straight lines.

In the area of large radii $r = 48 - 56\,\mathrm{cm}$, there are radial sectors which are located in the space between the spiral sectors forming the course of the mean field at the final radius. More detailed information related to the construction of spiral sectors can be found in articles [50] and [5]. Manufacturing tolerances and sector assembly tolerances ensuring preservation of the cyclotron design magnetic field properties are given in Chapter 3.3.

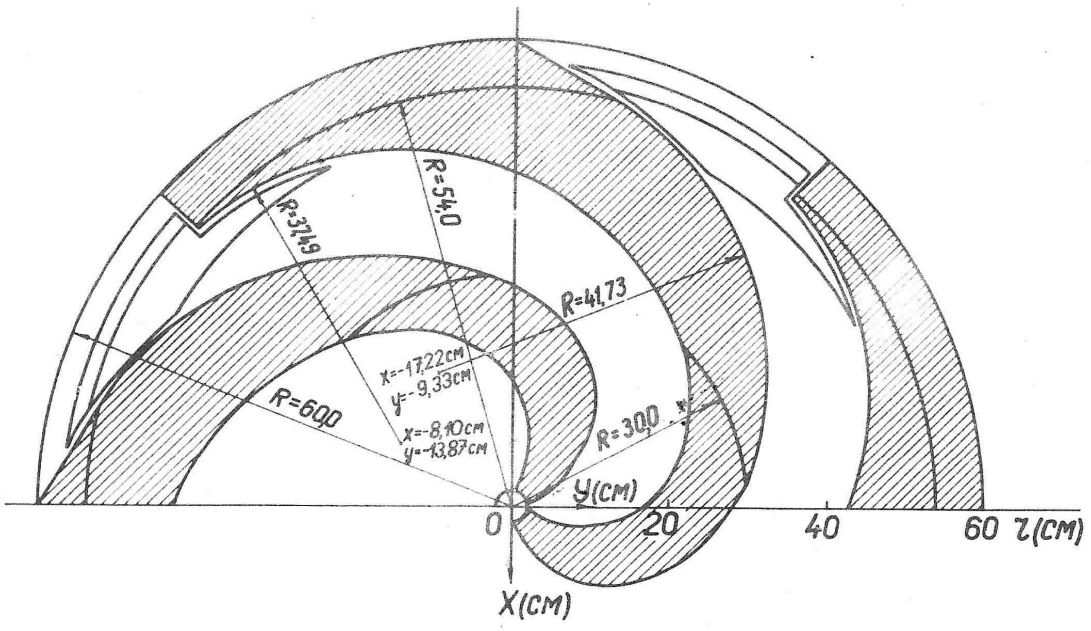

Figure 3.8: Shape of the spiral sectors with marked radii of structural circles. Reproduced from [3].

3.2.3 Trim coils

A set of 18 water cooled concentric trim coils is used for tuning the isochronous magnetic field and for fine tuning of the betatron oscillations ν_r and ν_z. The coils are located

between the radii of 5.5 and 53.3 cm and their coil axis coincides with the cyclotron axis. The maximal current of all the trim coils is in the range of 300 – 600 A. Table 3.3 and 3.4 list the maximal current, radial position, installation height and the number of turns of individual coils. All trim coils are made of high conductivity copper tubes with a diameter of 6 mm and a wall thickness of 1 mm. Each of the coils is constructed in a pair, which are distributed symmetrically with respect to the middle plane of the cyclotron, i.e. the plane with the coordinate z=0. Distribution of the coils is shown in Fig. 3.9.

Both the main coil and the trim coils can be powered either positively or negatively, which enables the acceleration of positive and negative ions. Total power consumption of the magnetic system tuned at the highest ion energy is approx 300 kW.

Table 3.3: Basic parameters of the cyclotron trim coils 1–9.

Coil number	1	2	3	4	5	6	7	8	9
Number of turns	5	5	5	4	3	3	3	3	2
Radius (mm)	55	90	120	145	195	243	277	313	337
Height (mm)	76	76	80	80	87	47.5	47.5	47.5	47.5
Max. current (A)	300	500	600	300	600	500	280	500	300

Table 3.4: Basic parameters of the cyclotron trim coils 10–18.

Coil number	10	11	12	13	14	15	16	17	18
Number of turns	2	2	2	2	3	4	4	4	4
Radius (mm)	357	385	405	425	457	479	497	515	533
Height (mm)	47.5	47.5	47.5	47.5	47.5	47.5	49.5	49.5	49.5
Max. current (A)	500	300	350	350	260	400	400	400	400

The first five trim coils are built inside the central part of magnet sectors, the remaining 13 coils are part of a copper plate covering the spiral sectors - the trim coils' holder. The coils' power leads serve also as cooling water inlets and are located in the magnetic valley between the sectors. Access to the vacuum chamber is ensured by a vacuum and electrical feed-through at the side of the vacuum chamber as it is shown in Fig. 3.9.

An electrical insulation of individual coil turns is ensured by a glass strip stabilized by an epoxy casting. The breakdown of the insulation of the supply wires of coil No. 6 in Fig. 5.22 was caused by a high ripple of the supply current and required repair and a three-quarter year shutdown of the cyclotron in 2022. A detail of the breakdown spot is shown in Fig. 3.11.

3.2.4 Harmonic coils

Initially the cyclotron was equipped with only one set of harmonic coils (HC) located in the central region at a radius of 14 cm. These HC coils ensure centering of the beam and determine the beam quality during the entire acceleration process. Harmonic coils at medium radius 42 cm were added later, but these did not prove to be useful and were not used.

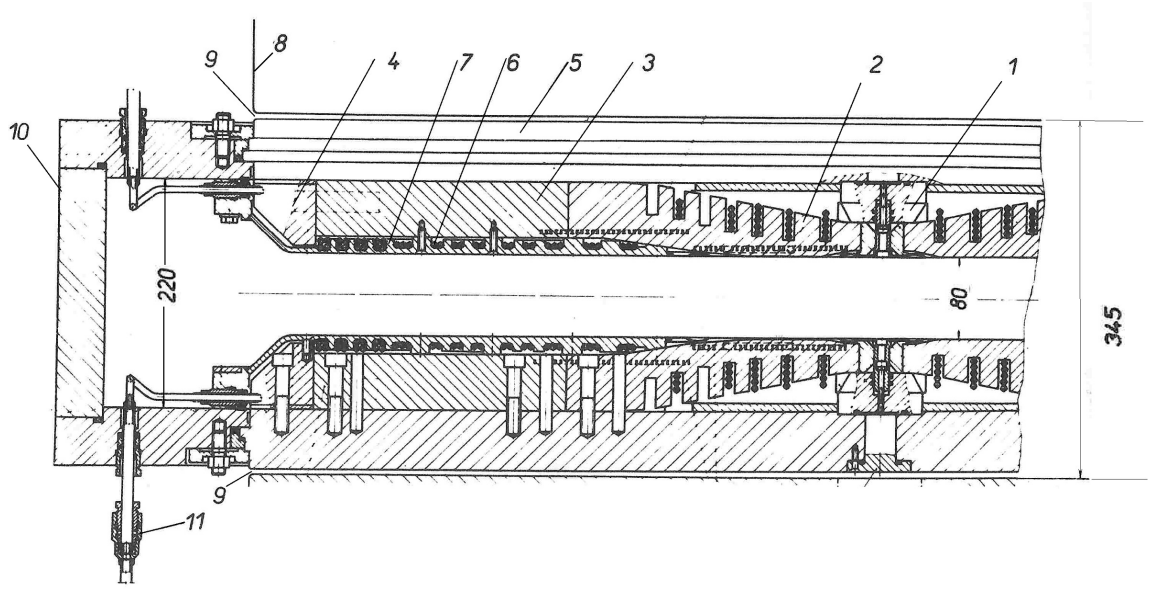

Figure 3.9: Accelerating chamber and magnetic sectors structure cross-section. Central plug – 1, magnetic sectors (central part – 2, middle part – 3, peripheral part – 4), iron sectors support – 5, trim coil no.13 – 6, trim coils holder – 7, magnet pole – 8, high reluctance gap – 9, chamber wall – 10, trim coils water inlet vacuum feed-through – 11. Reproduced from [3].

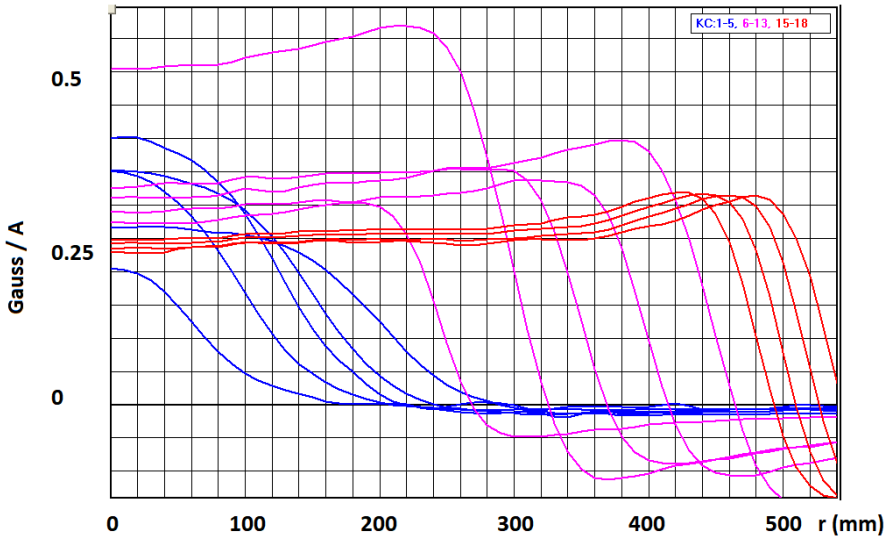

Figure 3.10: Contribution of individual trim coils to the basic magnetic field. trim coil 1 – 5 (blue), trim coil 6 – 13 (magenta), trim coil 15 – 18 (red). Credit [19].

Figure 3.11: Detail of the trim coil No. 6 power leads breakdown.

During the shutdown period in 2022 a new set of HC at radius 51 cm was installed in the cyclotron magnetic structure replacing the old medium radius HC. Since the new set of HC is intended to improve the beam extraction process, its design is a significant part of this dissertation thesis. The design and installation of the new harmonic coils is described in detail in the dedicated section 5.3.2. At present, the cyclotron is equipped with two sets of harmonic coils at radii 14 cm and 51 cm. Their field map and contribution to the cyclotron first harmonic magnetic field component is shown in Figures 3.12 and 3.13.

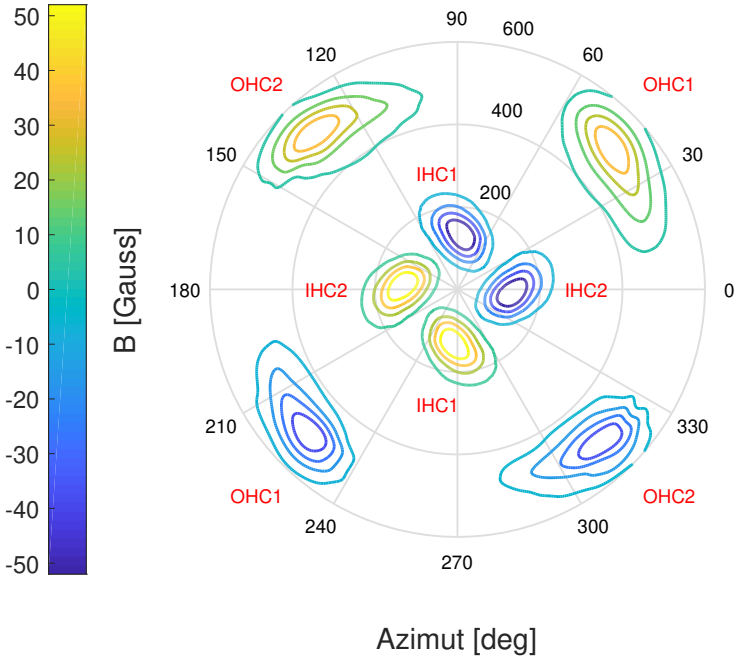

Figure 3.12: Magnetic field maps of inner (IHC) and outer (OHC) harmonic coils.

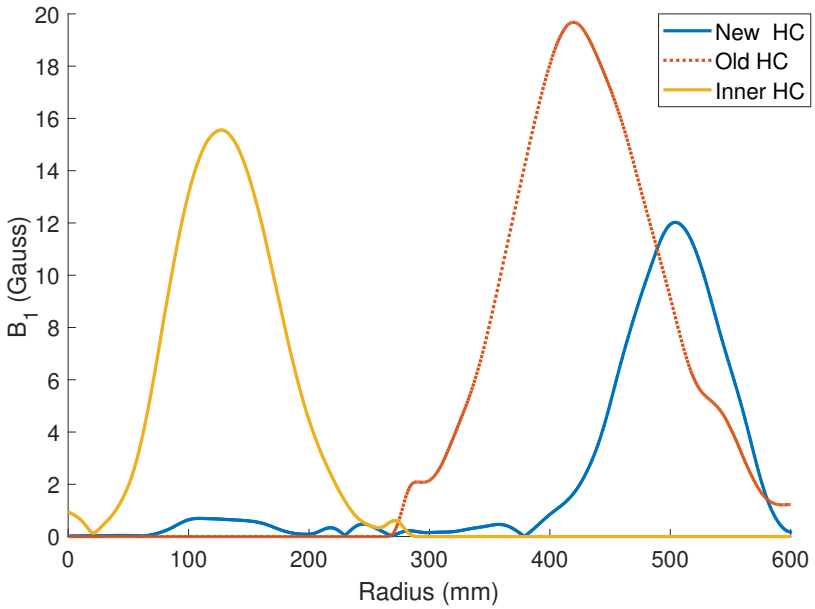

Figure 3.13: The harmonic coils' first harmonic contribution to the magnetic field for the inner and the old HC current 100 A and the new HC current 200 A.

3.2.5 Magnetic field measurement

The magnetic field of the U-120M cyclotron was measured several times in the past. The first detailed measurement was carried out during the commissioning of the cyclotron at the JINR Dubna in 1976. The magnetic field was mapped for three excitation levels of the main magnet coil – 175 A, 350 A and 610 A. For each of these levels a contribution of each cyclotron trim coil was investigated. After the cyclotron transfer to the Nuclear Physics Institute in Řež a control measurement was done confirming the cyclotron main parameters did not change during the machine transport and the final assembly. In a high detail the magnetic field was mapped again during the measurement periods in 1984 and 1988 [17].

The measurement carried out in 1984 was dedicated for optimization of the quality of the magnetic field. A considerable effort has been devoted to reducing presence of the fairly large first harmonic component of the magnetic field. The correction was made using ferromagnetic inserts between the poles and the sectors. From the protocols recorded during this measurement, we were able to reconstruct the progress of the work. The principle of the magnetic field perturbation correction using these inserts is described in chapter 3.3.

A detailed profile of the hysteresis curve of the magnet was investigated during the measurement in 1988. It was conducted for the magnetic field configurations close to the isochronous fields for protons, deuterons and ^{3}He ions. The range of the main coil excitation was 100 – 650 A with a step of 50 A. The entire magnetic field measurement took three months and was worked continuously during day and night shifts. The resulting magnetic field maps then served as a basis to a numerical model of the cyclotron. This model is described in more detail in section 4.1.1.

The magnetic field mapper design

The magnetic field measuring device – the magnetic field mapper – was developed at JINR Dubna in 1976 specially for mapping the U-120M cyclotron magnetic field in polar coordinates. During the subsequent field measurement campaigns at the NPI Řež the mapper underwent several improvements such as re-design of the azimuthal motor and a new design of the radial motor.

The active element of the magnetometer is a semiconductor Hall magnetic field sensor. It moves with a predefined step in the median plane of the magnetic field. The azimuthal range 0° – 360° is mapped in 43 steps. Based on information from eyewitnesses, the value of 43 steps was chosen deliberately as it is not divisible by four, which allows refine the measurement of the second and higher even harmonic components of the four fold symmetry magnetic field. The radial range 0 – 60 cm can be mapped with a minimal step of 2.5 mm. The vast majority of maps are taken with eight radial step i.e. with a field radial resolution of 2 cm.

Figure 3.14: The magnetic field mapper placed in the vacuum chamber.

The mapper itself consists of a rotating circular holder which is equipped with a mechanism for radial movement of the measuring probe as it is shown in Fig. 3.14. Rotation of the holder in the azimuth direction is performed by a transmission mechanism driven by a series DC electric motor. The gearbox is designed in such a way that there is not necessary to switch off the azimuthal motor while changing position between the 43 individual steps in one full revolution of the field mapper. This is achieved by an internal arrangement of the gearbox such that, within one measuring step, the azimuth drive wheel is rotating half of the time (the Hall sensor changes its azimuthal position) and stands still the other half (data is collected from the sensor), although the azimuthal motor is running continuously. Such a solution makes it possible to avoid unwanted electromagnetic noises arising during the switching on and off the azimuthal motor, which would occur during the measurement of one complete revolution. After completing the revolution, the azimuthal motor is turned off and the radial motor moves the measuring probe to the next radius and the process repeats.

The radial movement of the Hall sensor is provided by a special iron-free motor developed in-house which makes it possible to measure the magnetic field without being affected by inserted ferromagnetic material. The radial motor is constructed similarly to permanent magnet DC motors, with the only difference being that instead of a permanent magnet, the motor is excited by the magnetic field of the cyclotron. The radial motor is powered via a sliding contact, which means that the motor is only powered in the default azimuth position of the mapping wheel. The motor is active only when the mapper

changes the radial position of the Hall sensor so that its current does not influence the measured magnetic field.

Refurbishing of the magnetic field mapper

Before the magnetic measurement conducted in 2022, the field mapper was stored in the basement of the accelerator department for 34 years. Moreover the device was flooded in 2002 when the whole NPI accelerator department basement was under water. Although it was possible to develop a completely new magnetic measurement mechanism, usage of the old field mapper spared great amount of development effort. We decided to renovate the old mapper and utilize the saved time to develop the driving software. The mapper was disassembled to the last screw, cleaned, lubricated and reassembled. Only the gear housing of the azimuthal drive had to be fabricated completely.

Hall sensor

The condition of the field mapper mechanical part was satisfactory in the moment we have found it. Nevertheless the electrical part of the mapper was completely missing and the magnetic sensor was rather obsolete. The author of this thesis therefore had to design and construct the power system of the motor drives and their control and replace the old magnetic field sensor by a new one. For the field measurement I have chosen LakeShore Cryotronic [30] monocrystalic transverse magnetic field sensor HGT3030. This room temperature InAs low doped bulk sensor exhibits low output resistance leading to low thermal noise, low zero field offset and temperature drift. Parameters of the HGT3030 sensor are listed in Tab. 3.5. The corresponding data linearity error plot is shown in Fig. 3.15a.

Table 3.5: Hall sensor HGT3030 parameters [30].

Active area	0.76 mm diameter
Input resistance	2 Ω
Output resistance	2 Ω
Nominal control current I_c	100 mA
Magnetic sensitivity at I_c	8 mV/kG
Maximum linearity error	±1.25 % of reading
Zero field offset voltage at I_c	max 75 μV
Temperature coefficient of magnetic sensitivity	max. -0.04 %/°C
Temperature coefficient of offset at I_c	max. ±0.03 μV/°C
Calibration range	±30 kG at room temperature

The best magnetic field measurement practice is to place the Hall sensor to a temperature stabilized environment to ensure a constant value of the sensor zero field offset and magnetic sensitivity. The lack of time to develop the temperature stabilized Hall sensor enclosure forced us to only measure the temperature during the ongoing measurement. I designed the controller software to record the temperature during the magnetic measurement process, which allows temperature correction of the output value. A typical temperature drift during one measurement cycle stayed in the range ± 0.1 °C as it is shown

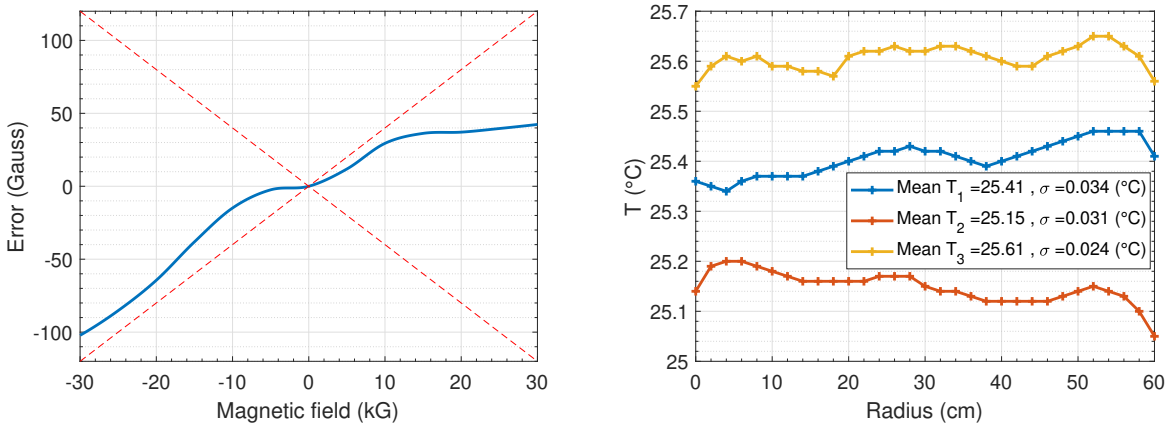

(a) HGT3030 Hall sensor linearity error data plot.

(b) Temperature drift for three typical magnetic field measurements.

Figure 3.15: Hall sensor linearity [30] and typical temperature drift during magnetic field measurements. The field was measured in levels -5 – -20 kG.

in Fig. 3.15b for three typical measurement runs. The measured data were subsequently calibrated according to the supplied calibration curve and the recorded temperature.

Hall sensor readout unit

Gaussmeters for precise magnetic field measurement are commercially available for example from companies Lake Shore Cryotronics, Inc [30] , Senis AG [2] and Group3 Technology Ltd [41]. Unfortunately their price usually starts at several thousand US dollars. As the price tag of a professional commercial solution was restrictive for us, I decided to build the gaussmeter from individual components and develop the operating software myself. This allowed us to build the magnetic field monitor for approximately one tenth of the commercial price.

The data acquisition unit necessary to readout a magnetic field value from the Hall sensor is commercially available from a Czech company JanasCard [35]. This small electronics R&D company has a long history in development of magnetic measurement readout components. Their top level high performance product AD24USB exhibits parameters fully comparable with the commercial gaussmeters from the above mentioned companies with a price tag of 500 USD. The JanasCard company provides for the AD24USB DDL libraries for for Delphi, VisualBasic, C++, Matlab and LabView.

The multi-function USB module AD24USB is a programmable DC current source with a precise differential analog inputs. The module is equipped with a single-chip microcomputer controlling an isolated high resolution integrating AD 8-channel converter and a programmable DC current source. The module is equipped with an additional unique features of AC modulation of input or output. The AC modulation of the unit input reduces the input offset and the input low frequency noise. The modulation of the unit output current eliminates parasitic thermoelectric voltages in input wires from the sensors. More details related to the modulation techniques used in the readout unit can be found in [35]. Basic parameters of the AD24USB readout unit are listed in Tab. 3.6

Table 3.6: AD24USB Hall sensor readout unit parameters [35].

Voltage reading resolution	22 – 26 bits
Sampling rate	80 – 3 samples/s
Analog inputs	8 differential or 16 single ended
Input range	$\pm 5\,\mathrm{V}$
Input noise w/o AC modulation	$210\,\mathrm{nV_{pp}}$
Input noise with AC modulation	$33\,\mathrm{nV_{pp}}$
Output current	100 mA
Output current resolution	16 bits

Mapper software

The magnetic measurement control program is created in the LabView development environment [32]. It combines the control of the mapper's positioning and the readout of the measured magnetic field values. The software allows for choosing one of the measurement modes, either measuring the complete magnetic map or measuring over one revolution. The latter mode carries out mapping of the magnetic field at certain radius over the full azimuth. This is particularly advantageous in tuning of the optimal position of the acceleration chamber, as will be described in Sec. 3.3. An integral part of the control program is a harmonic analysis of the measured field, the temperature monitoring of the Hall sensor, a calibration of the measured values and the creation of magnetic field maps.

The software also provides full control over the Hall sensor acquisition unit. It enables selection of the resolution of the readout value, control of the readout frequency and the amplitude of the control current. The AC modulation is optional. It is possible to apply it at the input or output of the AD24USB unit.

Description of the measurement process

The mapper finds initial azimuthal position and drives the radial Hall probe carriage to the zero radius. After the measurement is started, the azimuthal range is covered with 43 steps. In each step, depending on the readout frequency, approximately 20 values of the magnetic field and Hall sensor temperature are measured. In each step, a mean value and a standard deviation of the measured values is calculated and stored. After one full turn the mean values for each step, the mean value of the standard deviations of all steps and the mean temperature for the turn are stored in a log file. The carriage then makes one radial step and the whole process repeats itself. After reaching selected radius – for the full map after 31 radial steps – values from the log are converted to a magnetic field map and stored on a hard drive.

Measurement error

The measurement error estimation is based on the shift of the cyclotron frequency 2.2 between the measured map and the map used in actual accelerator. The magnetic field appears to be measured slightly higher than the actual field with an error of about 1.2 %.

Measurement progress

At the beginning of the U-120M cyclotron shutdown period in 2022, dedicated to the repair of the insulation fault in the trim coil system, several of the most commonly used isochronous fields were measured along with the basic field without the trim coils, in the range of the main coil current 100 to 600 A with a step of 100 A. The main purpose of the magnetic field measurement was to record the current configuration of the magnetic field so that after the repair it was possible to verify the correct assembly of the magnetic circuit while preserving the original operating parameters. The investigated isochronous magnetic fields correspond to the modes for negative hydrogen ions 19.3 MeV, 29 MeV and 36.4 MeV.

At the end of the repair, when the correction coils were repaired and the new harmonic coils were installed, the acceleration chamber was seated between the pole pieces of the magnet. During the subsequent magnetic measurements, the horizontal position of the chamber was fine-tuned with respect to the magnitude of the disturbance given by the first harmonic component of the magnetic field. Thanks to the horizontal offset of the chamber, it was possible to minimize this deviation to approximately one tenth of the value which was measured before the shutdown. After fixing the acceleration chamber in the position set in this way, the measurements were carried out in the same configuration as before the start of the repair. Details of the horizontal alignment of the chamber and the corresponding response in the first harmonic component of the magnetic field are presented in the next section.

3.3 Magnetic field systematic deviation

A systematic deviation of the magnetic field from the ideal fourfold rotationally symmetric field is manifested by an increase in components of the Fourier transform 2.26 that are not a multiple of four, the so-called disturbance harmonic components of the magnetic field. By investigating the first few disturbance harmonic components, one can effectively infer the quality of this field. In the following text, we will focus on the first perturbation component, i.e. the first harmonic component of the investigated magnetic field, which will be referred to in the text as the first harmonic perturbation component.

One of the main objectives of the magnetic measurement carried out in 2022 was to confirm the presence and evaluate the level of the first harmonic perturbation component in the U-120M cyclotron magnetic field. Imperfections in the ferromagnetic structure forming a spatially shaped magnetic field are most often caused by deviations in the dimensions of individual parts of the system, or by imperfect assembly of these elements. Manufacturing and assembly tolerances are specified at the design stage of the cyclotron and their adherence should be the main criterion when judging the quality of the final product. In addition, some flaws in the design of the machine may not be known during the facility design process and will become apparent only after the machine is completed and put into operation. The magnetic field perturbation resulting from such a procedure can then be considered systematic. In such a case, follow-up measures are taken, which will either completely or to some extent eliminate this disorder. The design flaw most likely occurred in the case of the U-120M cyclotron during the design of the vacuum acceleration chamber and its connection to the RF system. This connection became another source of systematic deviations in the magnetic field due to the deformation of the vacuum vessel caused by the pressure gradient.

In the following paragraphs, prescribed tolerances of the U-120M cyclotron and the observations found by measurements of the dimensions and deviations of selected parts of the magnetic system will be presented. The measurements were conducted during the cyclotron shutdown period in 2022. The systematic magnetic field deviation caused by the flaw of the vacuum acceleration chamber structure stiffness will also be discussed and one of the possible solutions leading to its mitigation will be proposed.

3.3.1 The magnetic system manufacturing and assembly tolerances

Any inaccuracy in the manufacturing of the magnetic structure affects the resulting magnetic field and generates a deviation from the ideal field. Since the impact of this deviation on the acceleration process changes depending on the location of the inaccuracy, manufacturing inaccuracy tolerances are prescribed for the critical components of the magnetic system. During the design of the cyclotron, the performed sensitivity analyzes resulted in limits in which the dimensions of the individual parts and the precision of the assembly have to be maintained. The tolerances of the magnetic system manufacturing and the assembly tolerances listed in Tab. 3.7 are taken from Ref. [5]. It is very interesting that the article doesn't mention a tolerance for the magnet poles parallelism which affects also the spiral sectors parallelism. It is possible to assume that the indicated quantity is common to both of these parameters.

One of the main criteria for the quality of the magnetic field is the minimum amplitude of the first harmonic component of the magnetic field. Any inaccuracy in the symmetry of the magnetic system construction will be manifested by an increase in this first harmonic component. The amplitudes of the first harmonic perturbation component of the magnetic field measured before the U-120M cyclotron transport from the JINR Dubna to the NPI Řež, i.e. the commissioning values [50], are shown in Fig. 3.16. The wave-forms shown in the figure correspond to the magnetic field at three excitation levels of the main coil 175 A, 350 A and 610 A.

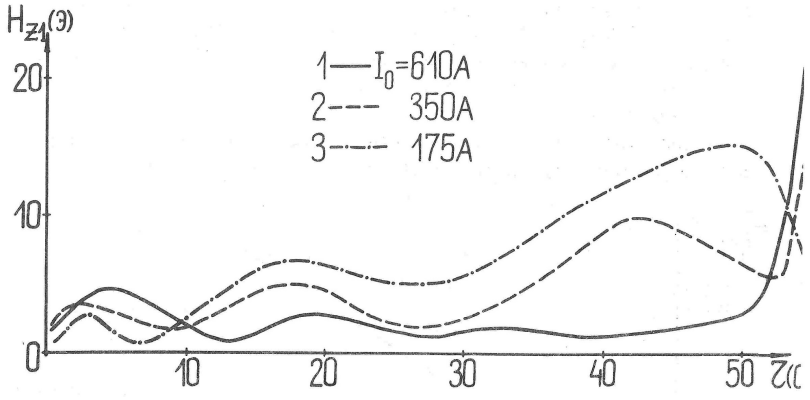

Figure 3.16: First harmonic component of the magnetic field for three levels of main coil excitation measured during commissioning of the U-120M cyclotron at JINR Dubna in 1976. The horizontal axis represents radius in centimeters, the vertical axis corresponds to the amplitude of the first harmonic component in units of Gauss. Reproduced from [50].

Table 3.7: Tolerances prescribed for the U-120M cyclotron. Taken from [50].

Deviation in spiral sectors profile	$< 0.1\,\mathrm{mm}$
Height difference of individual sectors	$< 0.05\,\mathrm{mm}$
Width difference of individual sectors	$< 0.05°$
Relative precision of the assembly of the spiral sectors	$\pm 0.05\,\mathrm{mm}$
Eccentricity error of top and bottom sector support disc	$< 0.2\,\mathrm{mm}$
Spiral sectors parallelism error	$< 0.1\,\mathrm{mm}$
Vacuum chamber placement precision between the magnet poles	$\pm 0.2\,\mathrm{mm}$

3.3.2 The Vacuum chamber deformation

The U-120M cyclotron was one of the first isochronous cyclotrons built in the Eastern Bloc in 1970's [13, 4]. With its predecessor, the classical U-120 cyclotron, this model shares the construction of the main magnet and the principle of guiding the dee from one side of the acceleration chamber. As the development of these types of accelerators continued over the following decades, the horizontal quarter wave resonance RF lines were gradually replaced by half wave vertical lines [61]. When placing the dee from the side of the acceleration chamber, the acceleration electrode must pass through one side of the chamber and its mechanical strength on this side is reduced. Under the influence of the forces given by the pressure difference on the walls of the acceleration chamber, deformations can occur in the case of insufficient mechanical stability of such a structure. This effect is very noticeable in quarter-wave resonant structures, where the accelerating electrode passes through only one wall of the chamber. In more modern cyclotrons with vertical guidance of the RF resonance system, this shortcoming is completely eliminated [82, 63], since the return path of the magnetic circuit is closed all the way around and deformations of the acceleration chamber due to the action of the pressure gradient cannot occur.

A brief overview of the design of the U-120M vacuum chamber was given in the paragraph describing the arrangement of the cyclotron 3.1. Figure 3.4 shows that the body of the magnet accommodates the return yoke and the magnet poles and that these parts form one inseparable unit. The vacuum acceleration chamber is placed between the magnet poles and includes an iron disc serving as an extension of the magnet poles and a support for the magnetic spiral sectors. Between the magnet poles and the support iron disk there is an air gap occupied by a loose alumina plate. Due to large reluctance of the gap we refer to this specific gap as a high reluctance gap [53]. The magnet poles and the magnetic sectors attached to the iron support disk are not firmly mechanically connected. A photograph of the magnetic circuit taken just after the acceleration chamber was taken from the space between the pole extensions is shown in Fig. 3.17.

The vacuum chamber has only three solid side walls ensuring the rigidity of the chamber see Fig. 3.18. The fourth side, through which the accelerating electrode passes, is opened towards the resonator and its mechanical stability is strengthened only by supports made of long screws. These screws were installed in later years after the cyclotron was commissioned. However, during magnetic measurements we found out that these screws do not grant firm mechanical support and moreover since they are made of iron with high permeability, they affect the internal magnetic field of the accelerator as it is discussed in section 3.3.5. Fig. 3.19 was taken before the start of disassembling the cyclotron and

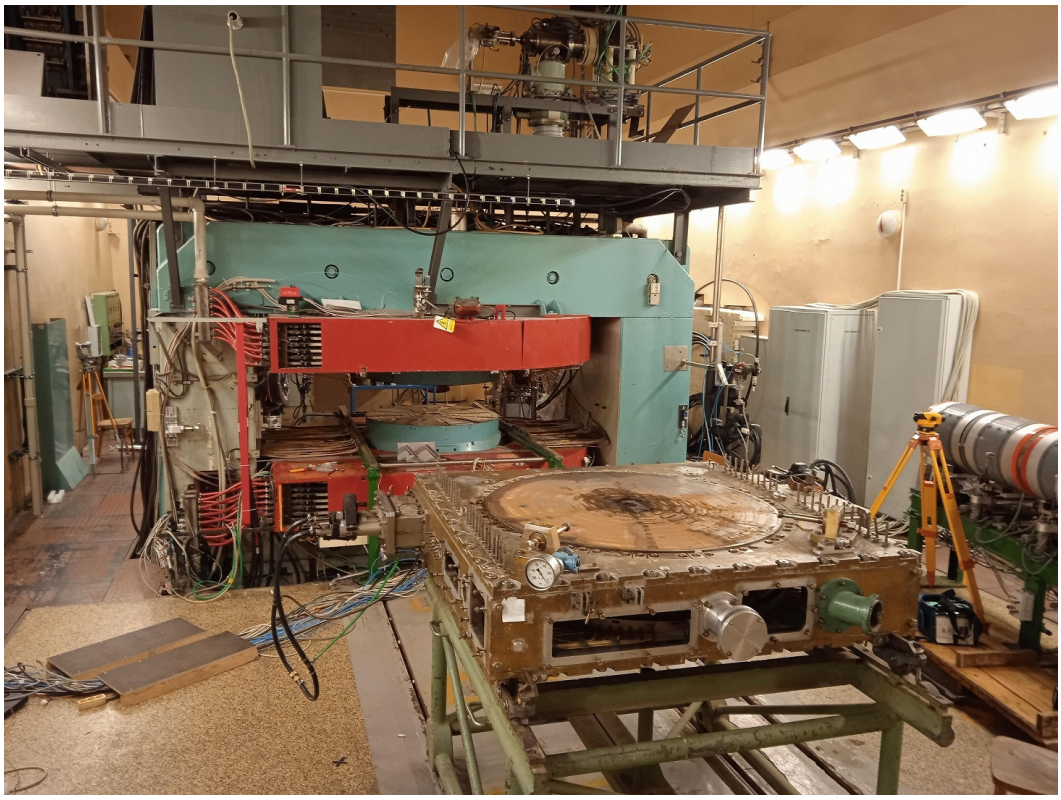

Figure 3.17: Vacuum chamber pulled out from the cyclotron magnet.

shows these supports in their working position.

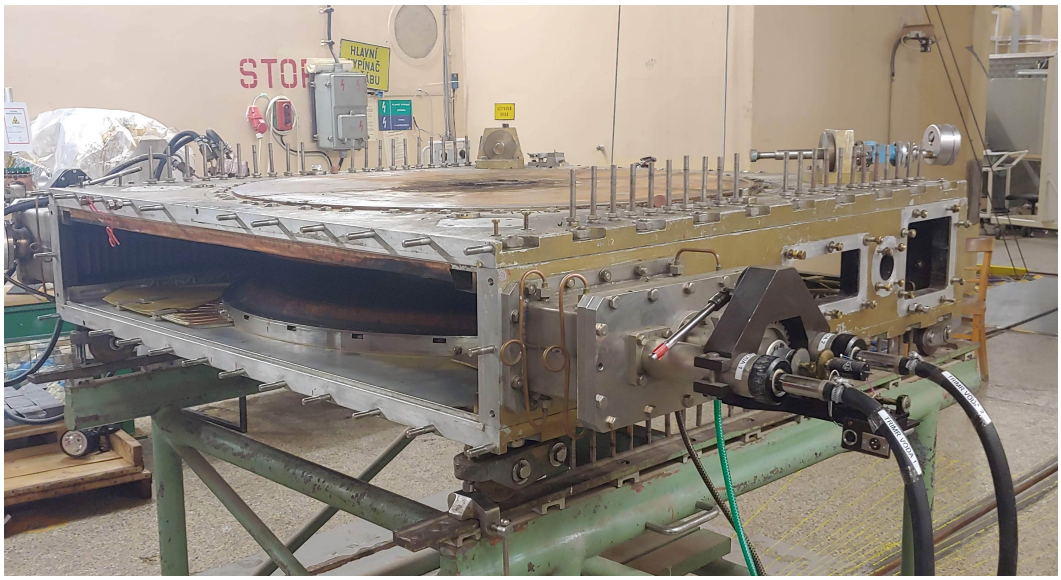

Figure 3.18: Open side of the vacuum chamber.

Without the magnetic field, the force due to the pressure gradient acting on the vacuum chamber top and bottom sides is approximately 2.3×10^5 N. As the magnetic field increases, the force acting on the iron plates at the top and the bottom of the chamber starts to compensate the atmospheric pressure. At a certain level of the magnetic field the two forces compensate each other. With increasing the magnetic field, the magnetic force increases to its maximum approximately 2.6×10^6 N for the fully excited magnet.

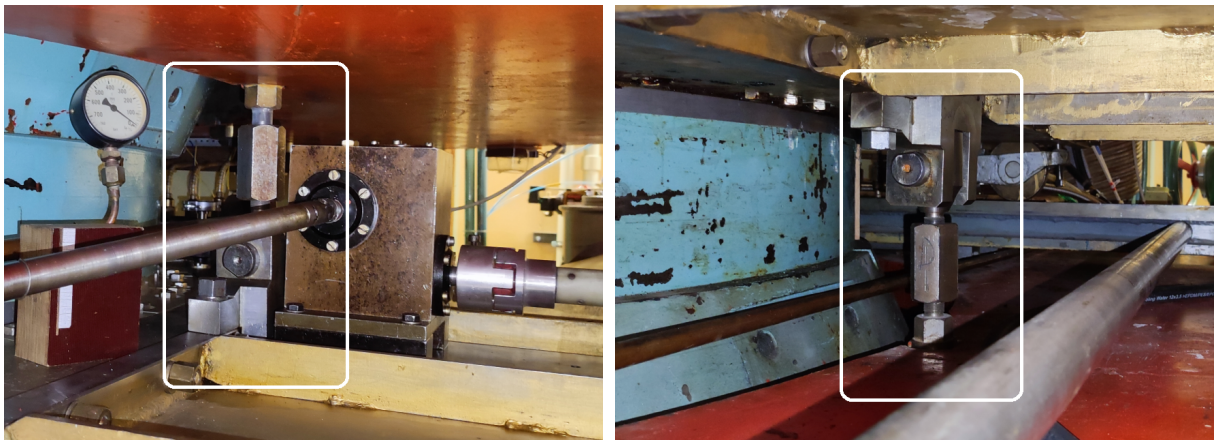

(a) Top side support. (b) Bottom side support.

Figure 3.19: Ferromagnetic screws supporting the open side of the vacuum chamber. The supports are inside the white squares. See text for further details.

The deformation of the upper and lower walls on the open side of the vacuum chamber results in the tilting of the spiral sectors fixed on the iron disc. Since the sectors and the disc are rigidly connected, changes in the gap distance between the sectors can be estimated indirectly by measuring the increase in the hight of the high reluctance gap between the iron support disc and the pole of the magnet. The gap has a size defined by a 5.8 mm thick non-magnetic flake-shaped insert. The exact shape and function of this insert will be described in more detail in section 3.3.4. Obviously, ideally the gap size should remain constant for all magnet excitation levels.

For the fully evacuated chamber with inside pressure 10^{-4} Pa and zero magnetic field the height of the gap at the open side is approximately 2 mm greater than the reference value, the corresponding tilt angle of the iron disc is 0.1°. The tilt caused by the pressure gradient is completely eliminated when the magnet current reaches 250 – 300 A. The residual tilt is approximately 0.3 mm even for the highest magnetic field.

A measure has been taken in the past to deal with this undesirable feature. Since the iron support disk of the sectors and the pole piece of the magnet limit a certain volume, this volume was sealed and evacuated. By reducing pressure on the upper and lower sides of the chamber in the volume of the magnetic high reluctance gap, the influence of the deformation of the acceleration chamber due to the pressure gradient was decreased. However, the vacuum sector tilt phenomenon is not fully eliminated and still produces difficulties with extraction of the positive particle beams at the lowest energies. Without the above mentioned measure it would be impossible to accelerate particles in the very low range of the cyclotron energy.

Reduction of the vacuum tilt magnetic field deviation

During the investigation of the vacuum influence on the sector tilt, numerical simulations of the vacuum chamber mechanical deformation were made using a 3D CAD model of the chamber. The simulations were performed by Ing. Radek Behal and showed results that are comparable with the values measured directly for the vacuum chamber. Figure 3.20 shows the simulated tilt of the vacuum chamber walls. For better visibility, the bending display is enlarged by a factor of 10.

Elimination of the tilt caused by the pressure gradient would require installation of a

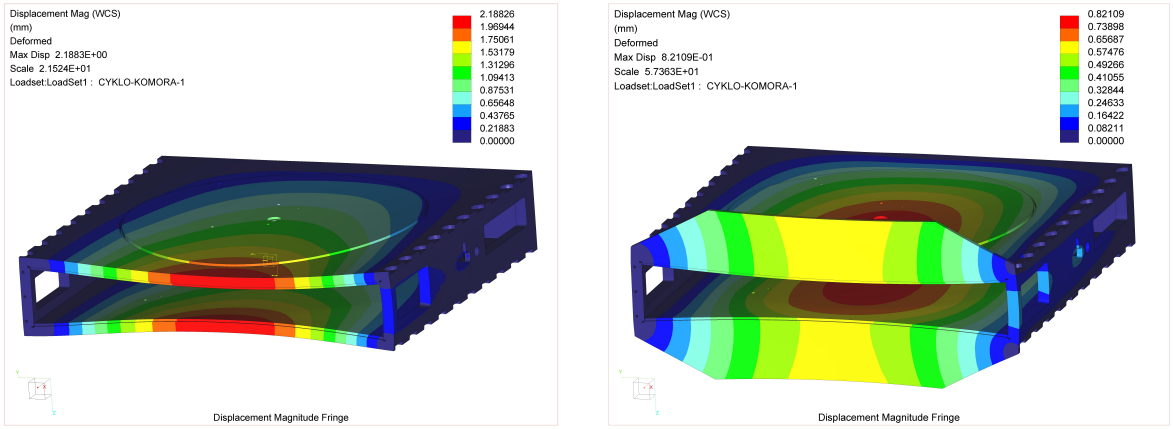

(a) Vacuum chamber deformation without the support.

(b) Vacuum chamber deformation with the support.

Figure 3.20: Simulation of the pressure gradient influence on the vacuum chamber deformation.

vertical support on the upper and lower sides of the acceleration chamber. A drawing of such a solution can be seen in Fig. 3.20. The numerical simulations have shown significant improvement of the vacuum chamber rigidity for support thickness of 20 – 40 mm. The chamber bent decreased almost five times, from 2.2 mm to 0.5 mm.

The practical implementation of such a solution will require a more detailed study. In particular, it would require a detailed design of the attachment of the support to the vacuum chamber such that, while maintaining the mechanically stabilizing properties of the support, it would be possible to disassemble the chamber and put it back together again without major restrictions. It is therefore likely to be a demanding design task, but according to preliminary analyzes and discussions with experienced mechanical engineers, it should be feasible [10].

3.3.3 Reduction of the magnet assembly systematic deviation

The magnetic field first harmonic perturbation were present in all magnetic maps measured over the course of the U-120M cyclotron's history and tended to increase with time. The size of the first harmonic perturbation measured before the accelerator was dismantled in 2022 is very considerable, see Fig. 3.21. The first harmonic perturbation caused by the deformation of the acceleration chamber due the pressure gradient was described in the previous section. This perturbation disappears at a magnet excitation level of approximately 300 A and even earlier when the high reluctance gap is evacuated.

The magnetic field systematic deviation caused by the chamber deformation cannot be measured directly using the magnetic field mapper. Since the acceleration chamber has to be open to atmospheric pressure during the magnetic field measurement, the vacuum deformation effect is not present as the pressures on all the walls of the chamber are the same. Therefore, although the influence of this effect strongly affects the accelerated beam, it does not appear in the measured magnetic field maps.

During the 1984 and 1988 shutdowns, considerable effort was devoted to minimizing the first harmonic perturbation. By inserting small pieces of magnetically soft iron, i.e. ferromagnetic inserts, into the high reluctance gap space, the first harmonic perturbation compensation was carried out for multiple magnetic field levels. By measuring the radial

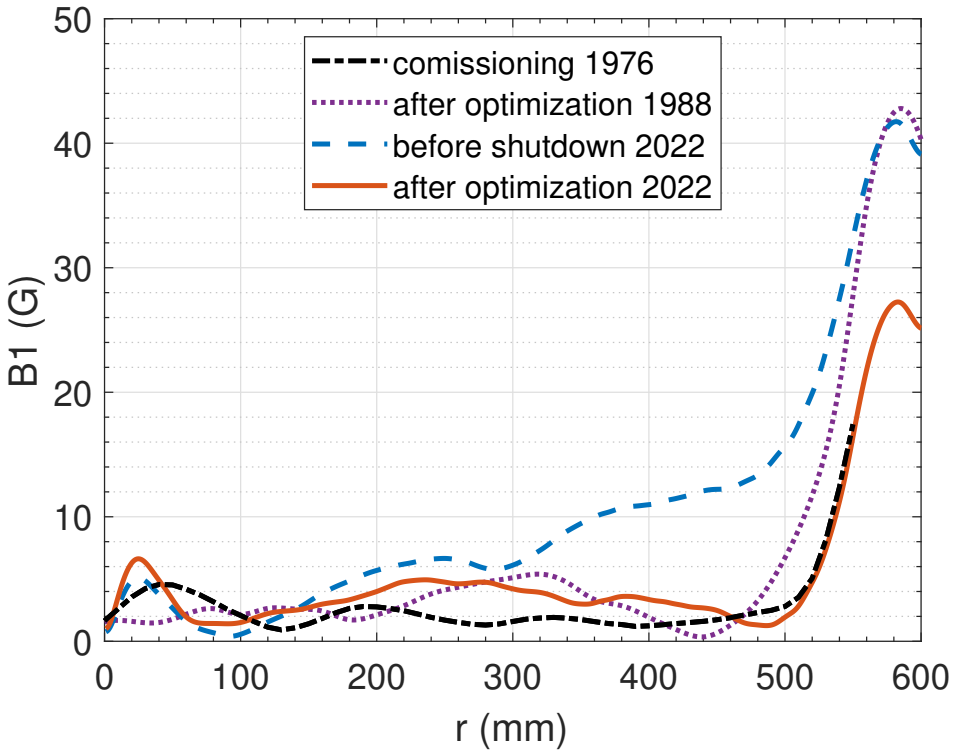

Figure 3.21: Comparison of individual measurements of the first harmonic component of the magnetic field.

course of the amplitude of the first harmonic component of the field and a phase of its maximum, suitable azimuths and radii for placing the inserts were determined. The effect of these ferromagnetic inserts on the cyclotron magnetic field is discussed in paragraph 3.3.4.

During the cyclotron shutdown period in 2022, we tried to find out the cause of the significant disturbance in the first harmonic component. We focused on three main hypotheses for a possible explanation of the source of the field error:

- significant deviations from manufacturing or assembly tolerances,
- presence of areas with different permeability in the magnet poles,
- magnet sectors tilt depending on the level of the magnetic field – parallelism error.

Unfortunately, the other two possible causes of the field error did not occur to us until the final stage of the reconstruction, when the accelerator chamber was placed in its working position. These are the following hypotheses:

- imperfect horizontal coverage of the magnet poles by the sectors – the eccentricity error of the sectors,
- imperfect horizontal coverage of the magnet poles itself - the eccentricity error of the poles.

It has to be said that during the search for deviations from the prescribed tolerances, we've focused on the search for one main defect in the magnetic system, but we did not

find any such deviation. Instead, we were able to identify a number of small variations spread throughout the magnetic system. Some of them are minor and their importance can probably be neglected, such as the differences in the heights of the tops of the sector fixing screws over the sectors, which differ by a few tenths of a millimeter.

Probably the most significant finding of the entire effort to improve the quality of the magnetic field was that the critical assembly parameter is the very fine adjustment of the horizontal position of the acceleration chamber in the space between the magnet poles. At the end of the reconstruction, we tuned this parameter to minimize the first harmonic perturbation to a level close to the value measured when the cyclotron was commissioned in 1976 as it is shown in Fig. 3.21.

In the following paragraphs, the individual findings will be described and compared with the prescribed tolerances.

Height difference of individual sectors

The height measurement of the individual sectors was made when the chamber was disassembled and its upper and lower walls, on which the sectors are located, were accesible. We measured the heights of the middle and the final part of the spiral sector at the positions where the top surface is flat and the measured value does not depend on precise radial position of the measurement probe. Since the beginning part of the sectors has shaped vertical profile, see Figure 3.9, the sectors' height was not measured in the central region. The prescribed manufacturing and assembly tolerance is required to be equal to or less than 0.05 mm. We estimate an error in measuring the individual heights to be ± 0.1 mm and all the measured values which are in this range are taken to be zero. The measured values greater then the tolerance are corrected by 0.1 mm towards zero. Even after this correction and after repeated measurements some of the measured values exceed the prescribed tolerance several times over. These deviations are subsequently reflected in the first harmonic perturbation curve as the sum of all individual perturbations at different radii.

Figure 3.22 shows the measured height differences at the positions where these were measured. Let us nevertheless point out that some of these distortions were rectified once the chamber was reassembled. It is possible that the direct measurement of the gap between the sectors was performed with lower accuracy, or individual deviations compensate for each other.

Homogeneity of the magnet poles iron

One of the possible causes of the magnetic field distortions could be the presence of regions with different permeability in the volume of magnet poles. When the chamber was removed from the cyclotron, we measured the magnetic field level directly on the surface of the magnetic poles and ruled out this possibility with a high degree of probability. The field difference along azimuth at radius 55 cm was of the order of $10 - 20$ Gauss only for the highest magnet saturation level. The searched disturbance should manifest itself with an amplitude of at least 50 Gauss.

Parallelism error of the sectors

The inclination of the magnetic sectors was investigated with great care. Thanks to the measurements of the high reluctance gap height made before the cyclotron shutdown, it

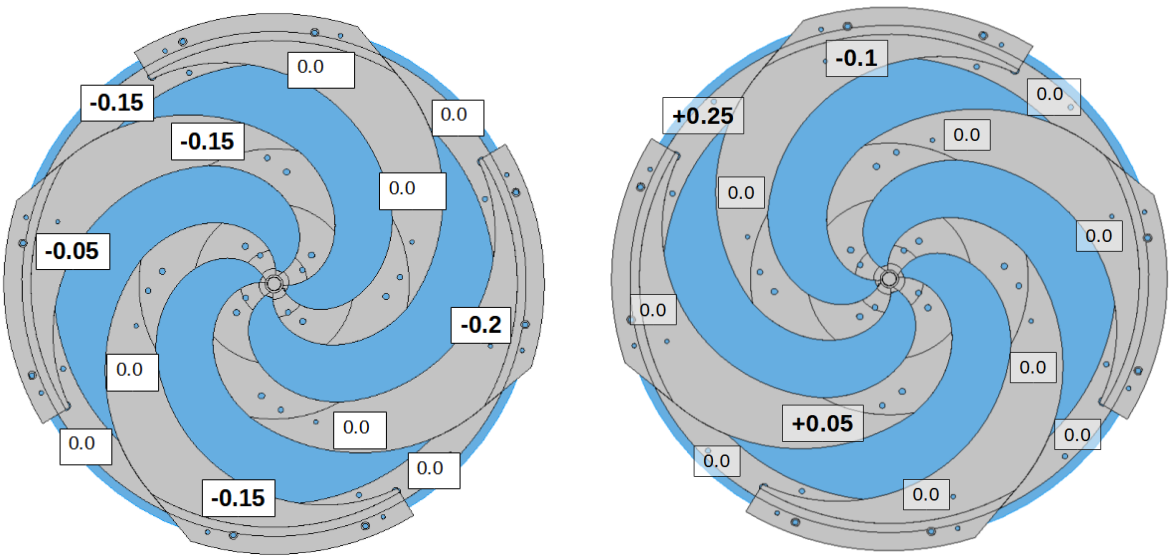

(a) Bottom sectors.

(b) Top sectors.

Figure 3.22: Individual height deviations at the measured positions.

was known that there is a systematic distortion in parallelism by about 0.2 – 0.3 mm. The value of 0.3 mm was subsequently confirmed by a direct measurement of the gap between the sectors. Without the magnetic field, the parallelism error of the sectors was less than 0.1 mm, or it was within the gap height measurement error range. After turning the magnetic field on, the gap between the sectors was manifestly reduced for the 600 A current of the main magnet. Moreover, the slope of the sectors accidentally corresponded to the azimuth of the maximum of the first harmonic perturbation component observed during the previous magnetic measurements.

Since the distortion in parallelism does not appear without a magnetic field and since the effect of the presence of a magnetic field should be just the opposite, i.e. the field should attract the iron discs and the sectors placed on it towards the poles of the magnet and thereby rather increase the gap between the sectors, the tilting of the sectors due to the action of the field was a mystery for a while. However, a precise measurement of the gap between the poles of the magnets with and without the presence of a magnetic field, partly shed light on the whole matter. We found that when the magnet is turned on, the pole pieces of the magnet are attracted to each other and the gap between them is reduced by approximately 0.14 mm. In addition, one side of the pole tilts more then the other. Initial distortion of parallelism of the magnet poles without the magnetic field is approximately 0.08 mm . After the magnet is switched on, the gap height lowers and the gap height distortion increases to approx. 0.16 mm. Fig. 3.23a shows height of the poles gap without the magnetic field, Fig. 3.23b shows the same gap height for 600 A in the main coil. In these two figures, the measured values represent the vertical dimension of the gap reduced by 345 mm, which is the base height of the gap, i.e. the actual measured height of the gap is H=345+h, where h is in hundredths of a millimeter. Specifically, for a value of h=52 in Fig. 3.23a at the position $[x/y] = [300, 400]$ mm, the actual gap height is H=345.52 mm. Fig. 3.23c shows the difference between the two plots and expresses how the gap between the poles has changed after turning the magnetic field on. The same plot in 3D is shown in Fig. 3.24, where the vertical axis is the gap size change. Local peaks in the difference figures are due to a measurement error.

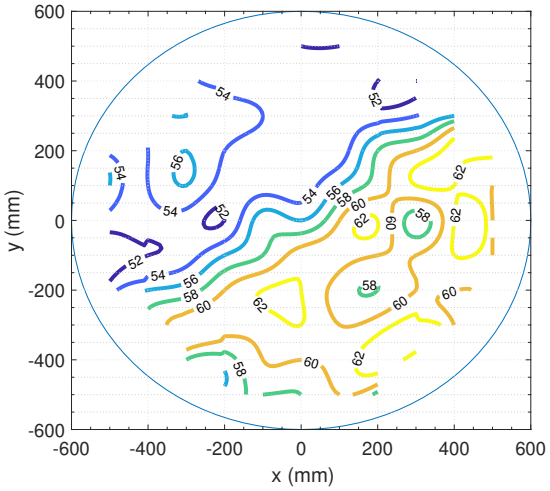

(a) Gap height for the main magnet at 0 A.

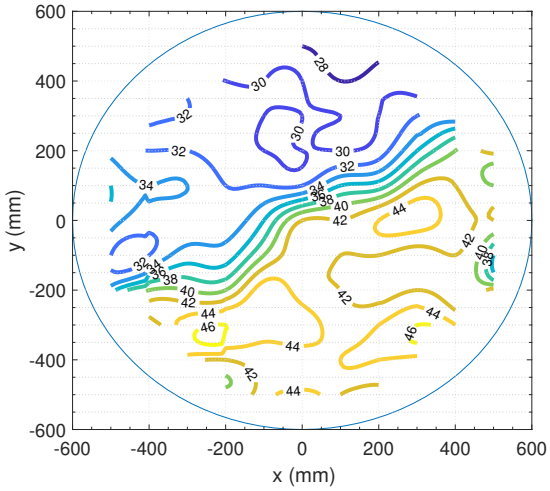

(b) Gap height for the main magnet at 600 A.

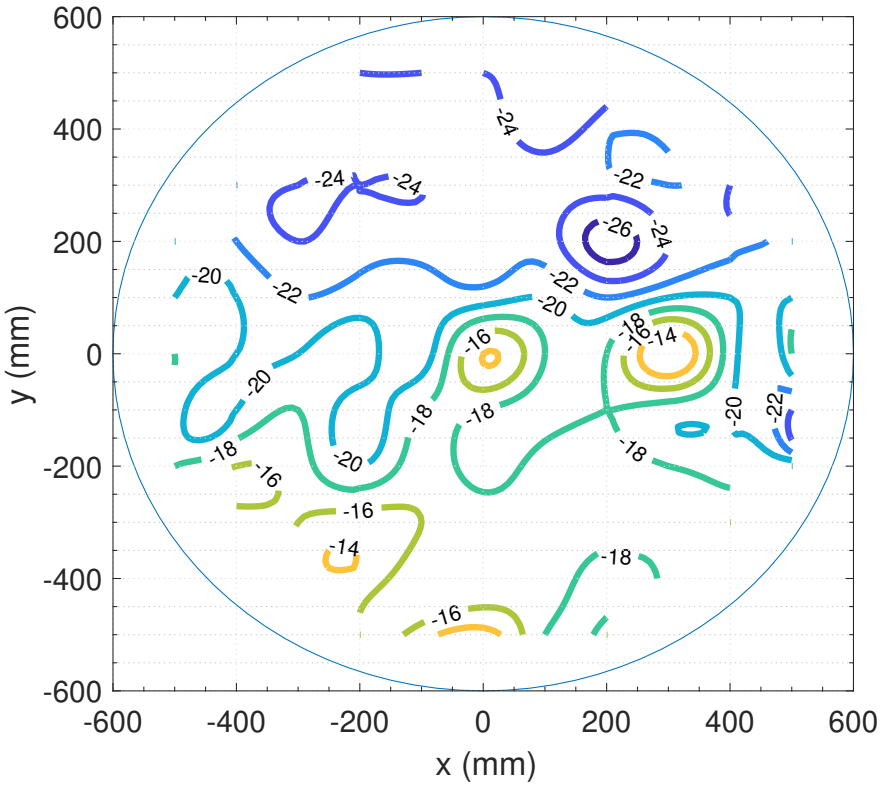

(c) Gap height difference.

Figure 3.23: Heights of the magnet poles gap with and without the magnetic field. Actual height is 345 + measured value/100 (mm). Details given in the text.

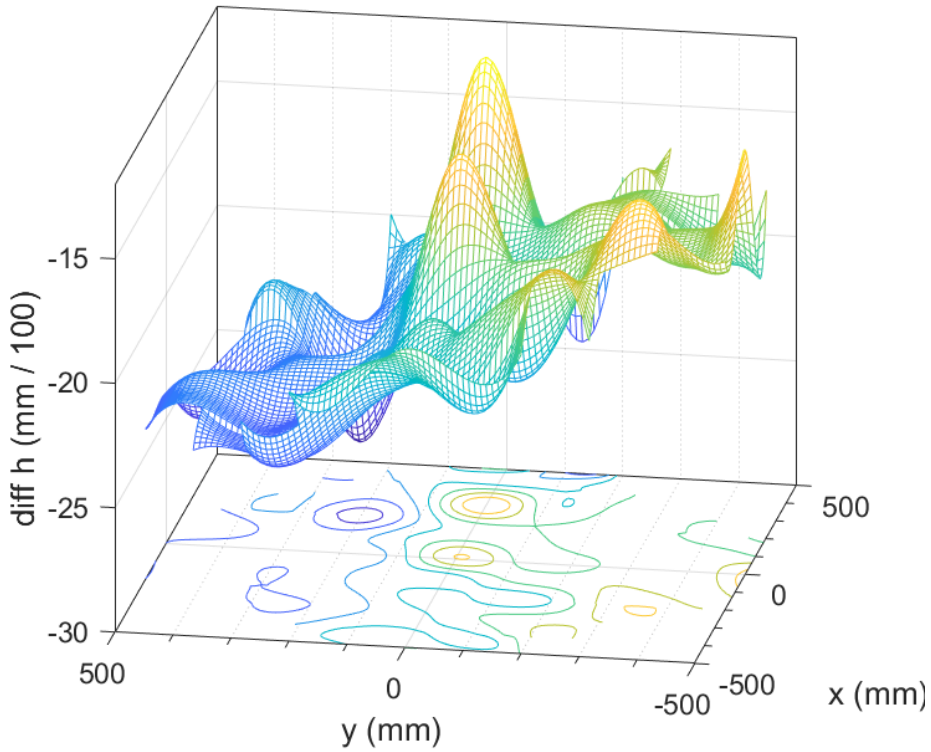

Figure 3.24: Relative change of the pole gap height after switching the magnetic field on. See text for further details.

It follows that the poles of the magnet are not perfectly attached to the magnet yoke and when the magnet is excited, they come closer to each other and tilt slightly. Subsequently, the acceleration chamber is also asymmetrically deformed, which causes an error in the magnetic field.

Numerical simulation of the sectors tilt effect

The measured value of the sector parallelism error of 0.3 mm is three times greater than the value of 0.1 mm allowed by the designers of the magnetic system. Numerical simulations in Opera [66] of a tilt 0.05° corresponding to the parallelism error 1 mm indicate that the parallelism error is probably responsible for only a part of the field distortion, see Figure 3.25. Numerical simulations of the tilt 0.014° corresponding to the actual parallelism error 0.3 mm suffered from problems with computational grid formation and have not been successfully performed so far.

Accelerating chamber horizontal alignment

At the end of the cyclotron shutdown period in autumn 2022 we made fine adjustment of the vacuum chamber horizontal position with respect to the magnet poles. Based on an idea described in an article related to the Polish cyclotron AIC 144 [15], we were able to minimize the first harmonic perturbation in the magnetic field to a satisfactory level. We monitored the amplitude of the first harmonic perturbation at a radius of 50 cm using the magnetic field mapper and changed the horizontal position of the acceleration chamber in various directions with 0.1 mm long steps. Initially we shifted the chamber

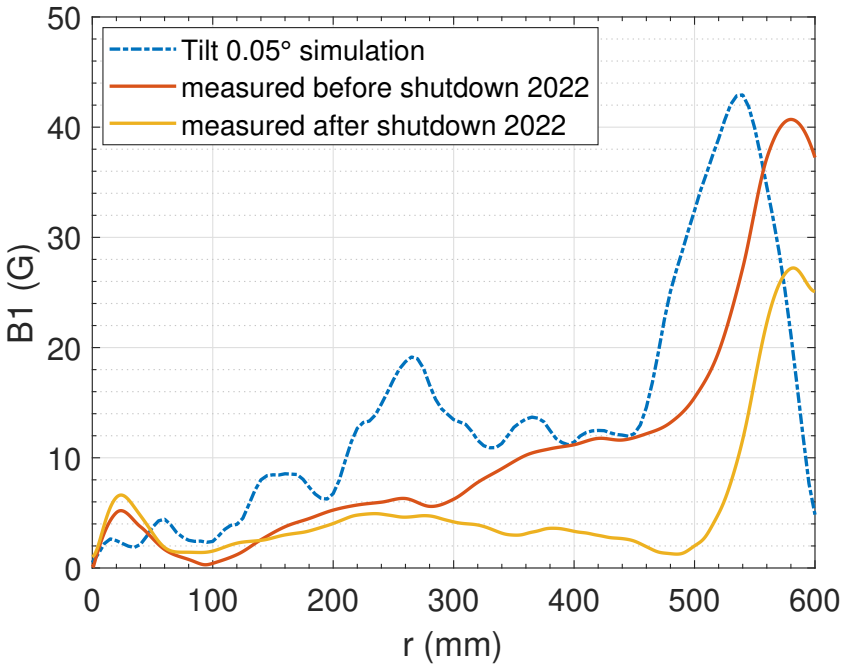

Figure 3.25: First harmonic component as measured before and after the 2022 shutdown. Data are compared with a simulation of the cyclotron field by the Opera software, where the geometry accounts for a 0.05° tilt of sectors.

towards the azimuth of 150° where the first harmonic perturbation was maximal. With this movement, we were able to reduce the amplitude of the first harmonic perturbation. When moving along this direction we found a pronounced minimum in magnetic field deviation. Starting from this position we proceeded in the perpendicular direction to find the global minimum of the distortion. In this way, we were able to reduce the size of the first harmonic perturbation at the extraction radius 50 cm from a value of 15 Gauss measured at the beginning of the shutdown period to a value of about 2 Gauss. This newly found minimum value of the first harmonic perturbation amplitude could probably be considered the smallest achievable on the U-120M cyclotron. I am led to this conclusion by considering the values measured during the commissioning of the accelerator in 1976 see Fig. 3.21, which are very close to the values we managed to achieve. The radial profile of the perturbation between 10 and 50 cm emerges due to accumulation of large amount of small deviations from the prescribed tolerances. The "bump" below 10 cm is most probably a result of a damage of the central region plug as it will be discussed in the next paragraph.

Central region defect

It is worth noting that a substantial magnetic field error in the central region appears in all the measured magnetic field maps. This fault is not present in the 1988 maps as shown in Fig. 3.26, and its cause is the long-term operation of the accelerator without limiting the current of the RF generator during discharges. The consequence of such operation is considerable damage of the central plug and the erosion of a considerable amount of iron. The consequences, we discovered after opening the acceleration chamber, can be seen in Fig. 3.27.

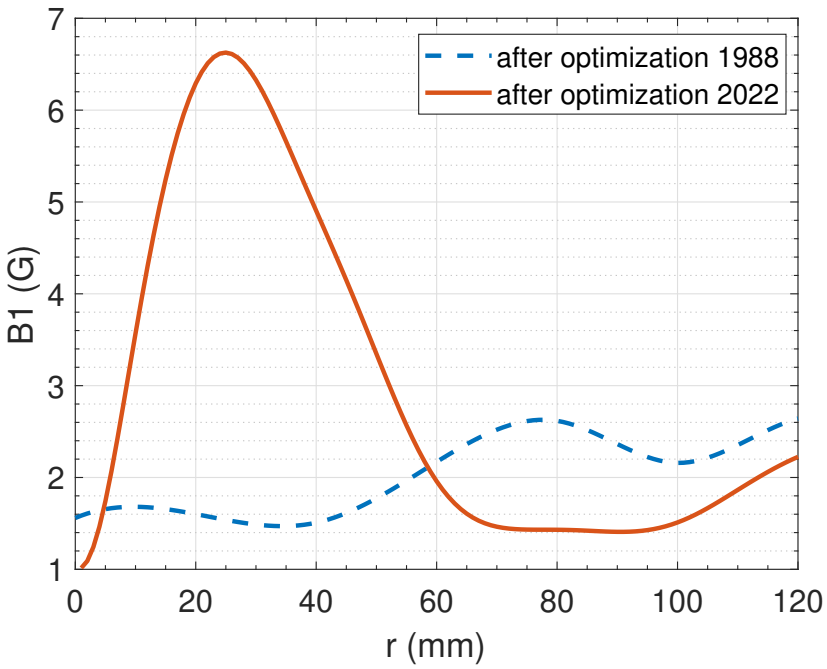

Figure 3.26: Central region magnetic field defect.

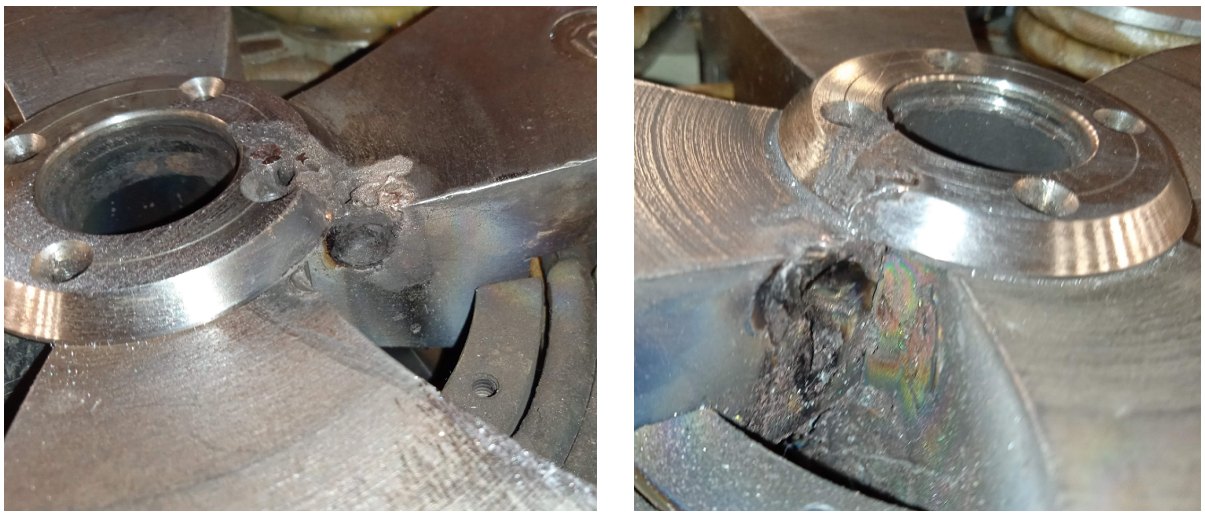

(a) Top sector.

(b) Bottom sector.

Figure 3.27: Holes in the sectors responsible for the magnetic field defect in the central region.

Although it is not visible from the pictures, these holes have a depth of several mm. I estimated that at least 1 cm^3 of material is missing from the bottom plug, which of course has a significant effect on the resulting homogeneity of the magnetic field. According to the performed simulations of the ion beam dynamics, the defect should probably not have significant consequences on the accelerated beam. This defect was left uncorrected as there were concerns that the repair by welding would cause damage to an even greater extent than the original defect.

3.3.4 Magnetic inserts

The method of the horizontal shift of the acceleration chamber with respect to the magnet poles has not been utilized to improve the magnetic field properties back in 1988. Instead of it, the alumina flake shaped disk with cutted periodic openings holes, see Fig. 3.28, was placed between the magnet poles and the vacuum chamber iron disk. Ferromagnetic inserts were subsequently inserted into the disc cutouts to modify the resulting shape of the magnetic field. For homogeneity of the resulting field, the inserts are placed in a pair, one insert at the top of the chamber and the second one at the bottom.

Figure 3.28: Alumina flake disk with cutouts for the ferromagnetic inserts.

By combining ferromagnetic inserts located at different azimuths and at different radii, it was possible to minimize the first harmonic perturbation for some magnetic field levels. At other levels, the situation either did not change or got worse. As a result, when the cyclotron was disassembled in 2022, only a single pair of the inserts located at the azimuth 300° compensating the largest field error magnitude was present. Most probably it was the best compromise between the inserts effect for the high and the low magnetic fields chosen in 1988.

Radial profiles of the first harmonic component and phase of its maximum for fields with and without the inserts placed at 240° is shown in Fig. 3.29. In Figures 3.29a and 3.29b the blue lines show the improvement of the first harmonic perturbation when the insert is present. The influence of the insert on the magnetic field for 500 A in the main coil is shown in Fig. 3.29c. The figure presents the result of subtraction of a map measured with the inserts and a map measured under the same conditions but without them.

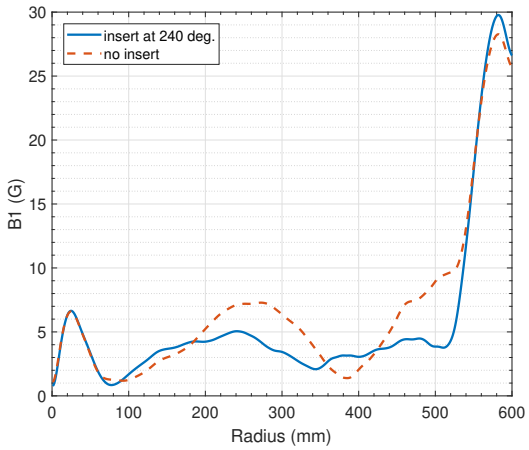

(a) Effect on the first harmonic perturbation amplitude.

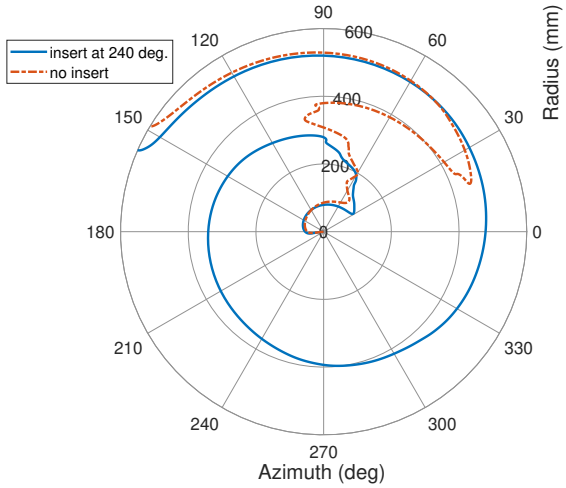

(b) Effect on the first harmonic perturbation phase.

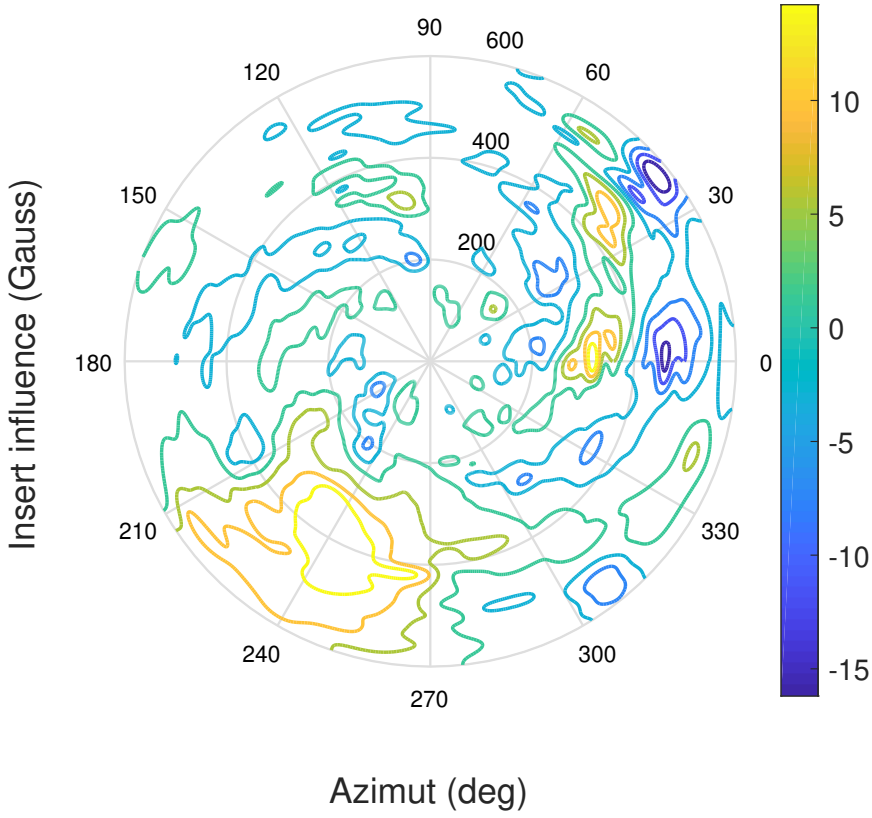

(c) Effect on the magnetic field.

Figure 3.29: Effect of the ferromagnetic insert placed at azimuth 240°.

3.3.5 Influence of the chamber holder supports

The upper one of the two chamber holders which should prevent the inward deformation of the acceleration chamber is shown in Fig. 3.19. As already mentioned, ferromagnetic nature of these elements causes undesirable changes in the magnetic field. In the same way as in the case of inserts, their influence on the magnetic field of the cyclotron can be displayed. The holders are placed at azimuth 90° and radius approx. 70 cm i.e. 10 cm from the outer boundary of the magnet poles. The chamber horizontal alignment was optimized taking into account the presence of the holders during the normal operation before the influence of the holder was investigated. For that reason, the radial profile of the first harmonic perturbation has worsened after their removal as it is shown in Figures 3.30a and 3.30b. The difference magnetic field map is shown in Fig. 3.30c.

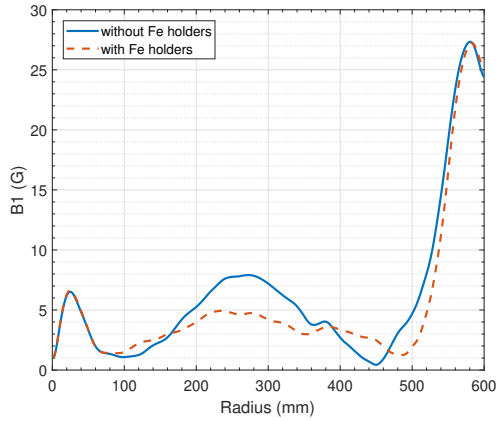

(a) Effect on the first harmonic perturbation amplitude.

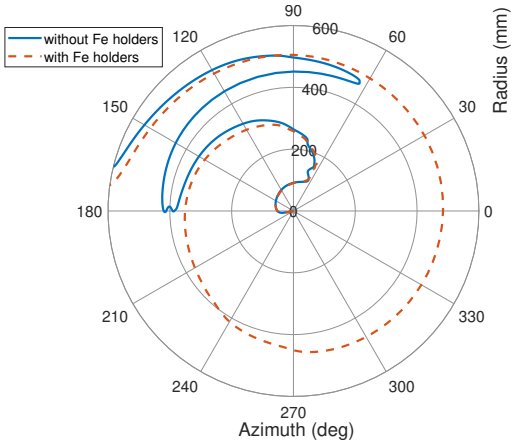

(b) Effect on the first harmonic perturbation phase.

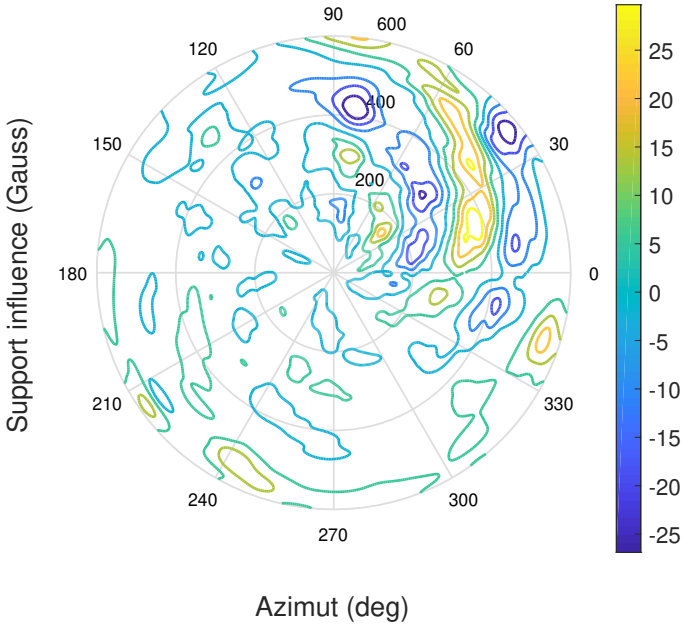

(c) Effect on the magnetic field.

Figure 3.30: Effect of the ferromagnetic chamber support holder placed at azimuth 90°.

The difference in amplitude and phase of the first harmonic component in the compar-

ative figures for chamber holders and ferromagnetic inserts is due to the different time when the effects were measured. While the influence of the inserts was investigated before the optimization of the horizontal position of the chamber, the influence of the holders was determined only after it.

3.3.6 The pole assembly error

We observed the asymmetry of the covering of the upper and lower iron support sectors with the pole of the magnet only in the last days of the cyclotron repair. This was in the course of settling the chamber into its final horizontal position and the cyclotron had to be prepared for recommissioning. Due to time constraints, it was no longer possible to proceed with further removal of the acceleration chamber from the magnet space and verification of the correctness of the hypothesis.

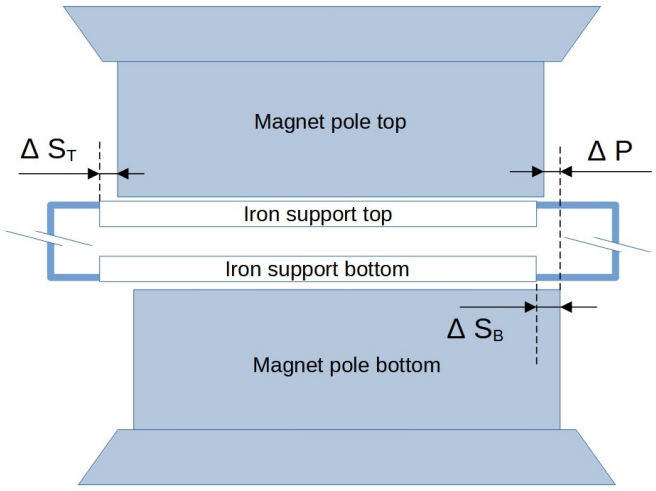

Figure 3.31: Schematic sketch of the magnet poles assembly. Dimensions are not to actual scale. See text for further details.

We measured a very strange asymmetry, which manifested itself as a discrepancy in the subtle horizontal position of the upper and lower walls of the acceleration chamber, respectively, of the sector support iron disks. This deviation can basically have two causes. The first possibility is that the chamber is slightly inclined, i.e. that its side walls are not perfectly perpendicular to the bottom and top. The second cause could be an imperfect covering of the magnet's poles, i.e. an error in the eccentricity of the magnet's poles.

The situation is shown schematically in Fig. 3.31. The measured value of the overlap of the upper sector over the pole extension S_T is 0.5 mm. The embedment value of the lower sector S_B is 0.1 mm. The azimuth on which the values were measured is 150°. It is worth noting that the azimuth at which this deviation is detected corresponds very well to the azimuth of the maximum of the first harmonic perturbation component of the magnetic field. Whether it is an error of the eccentricity of the pole extensions, i.e. whether the ΔP deviation value marked in the picture is non-zero, it cannot be determined due to the size of the deviation – approximately 0.4 mm – if the acceleration chamber is located in the space between the magnet poles. The verification of this hypothesis will probably only be possible during the next shutdown, when the acceleration chamber will be again driven outside the area of the magnet poles.

4 Cyclotron U-120M model

4.1 Software resources

Software resources and related numerical model of the cyclotron U-120M played a key role in the facility evolution. Sophisticated support programs utilizing real-time data obtained from beam phase measurement were used for isochronization of the cyclotron regimes from the first moments of the cyclotron operation [6, 23]. Over the time a system for semi-automated machine tuning and measurement of basic accelerator properties with only of minimal input from the side of cyclotron operators evolved. Since the development of computer hardware was very fast, and the constant need for higher computing power required a change of mainframe from time to time, it was not easy to transfer the complete software equipment to new hardware systems. As a result, over time, the automated functionality implemented on very old computer systems such as the M6000 with only a few KB of memory and punched paper cards instead of a hard disk became less and less usable. Thus, the control of the cyclotron gradually changed from computer-controlled and operator-supervised to an operator-controlled system with a computer support.

Thoughtful magnetic measurements enabled the creation of a precise mathematical model for off-line simulation of the acceleration processes and calculations of the required characteristics of the acceleration modes including the beam phase with good accuracy. Currently, most of the basic isochronous regimes of the cyclotron are tuned and stored in the database. These regimes serve as the basis for the day-to-day operation of the accelerator and at the same time as input data for programs for simulating the dynamics of the accelerated beam and extraction processes.

Further in this chapter the cyclotron mathematical model and the software for numerical simulation of the beam dynamics will be described in more detail.

4.1.1 The cyclotron mathematical model WModel

The mathematical model of the cyclotron (WModel) is designed to calculate the average values of the magnetic induction over the entire range of radii for arbitrarily chosen currents in the main coil and the cyclotron trim coils. The trim coils 7–8, 9–10, 11–12 and 13–14 are connected in series which has reduced the number of calculated trim coils to 14. Calculation of the isochronous fields is based on three sets of magnetic field used for protons, deuterons and $^3He^2$ ions each measured at 12 levels and the trim coils contribution measured at 4 levels of the magnetic field [17].

The resulting isochronous field is formed by parabolic interpolation of three closest measured basic field levels and calculated contribution of the trim coils. The Bc matrix 4.1 describing the magnetic field has size $[61 \times 17]$ and consist of 14 columns for the trim coil coefficient contribution and 3 columns for the main coil. The matrix element for k-th trim coil and j-th radius are

$$Bc[j,k] = \Delta Bs[j]/\Delta I[k]. \tag{4.1}$$

The main coil linear Bc [j,15], quadratic Bc[j,16] and absolute Bc [j,17] coefficient are calculated [18]. The average field values Bs on j-th radius are then calculated as

$$Bs[j] = Bc[j,17] + Bc[j,16] \times \Delta I[15] + \sum_{k=1}^{15} Bc[j,k] \times \Delta I[k], \tag{4.2}$$

where $\Delta I[k]$ are deviations of the actual currents from the values of their basic level. The accelerating regime is optimized using modified least square method [19], where the functional

$$F = \sum_{j=1}^{61} \omega_j (\sum_{k=1}^{15} Bc_{j,k} \times \Delta I_k - \Delta Bs_j)^2 + \sum_{k=1}^{15} \alpha_k^2 (I_k - Iz_k)^2 \tag{4.3}$$

is minimized. The coefficient ω_j reflects the efficiency of optimization at the j-th radius while the α_k reflects the k-th trim coil participation in it. Resulting currents I_k for non-zero α_k will converge to Iz_k values. The final solution for $Iz_k = 0$ aims at the minimum energy consumption at the trim coils. Coefficient α_{15} for the main coil is always zero.

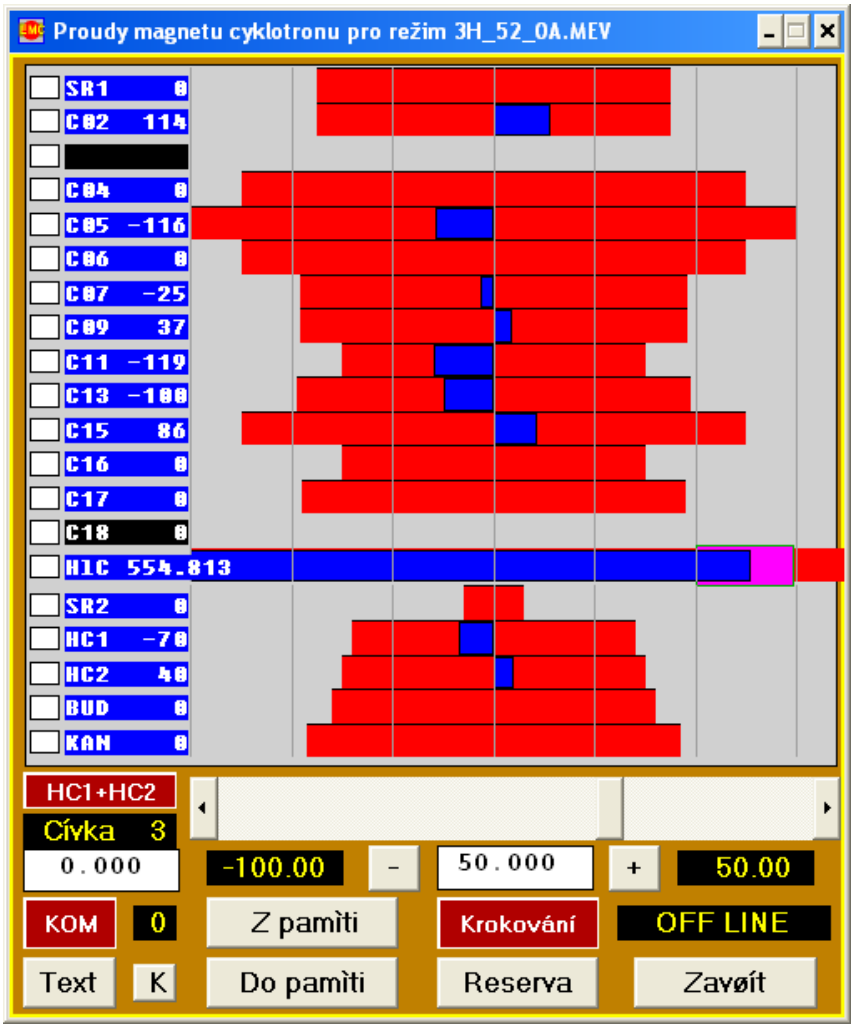

Figure 4.1: Operator interface to the mathematical model WModel. Credit [19].

The radial dependence of the mean magnetic induction and the beam transit phase are calculated. The field index $n(r)$, frequencies of the betatron oscillations ν_r and ν_z and the beam energy are calculated for each radius using formulas [19]. The result of

the optimization can be stored in the mode database for further use by the accelerator operator or for further processing in programs dedicated for the study of beam dynamics. An example of the WModel optimizer user interface is shown in Fig. 4.1 where individual currents for all coils may be set. Basic parameters of the tuned isochronous regime for $^3He^2$ ions at 52 MeV are shown in Fig. 4.2. Using the main window, the operator is able to optimize the beam phase and horizontal and vertical betatron oscillations ν_r and ν_z displayed interactively in monitor windows shown in Fig. 4.3 where are denoted as Q_r and Q_z, respectively.

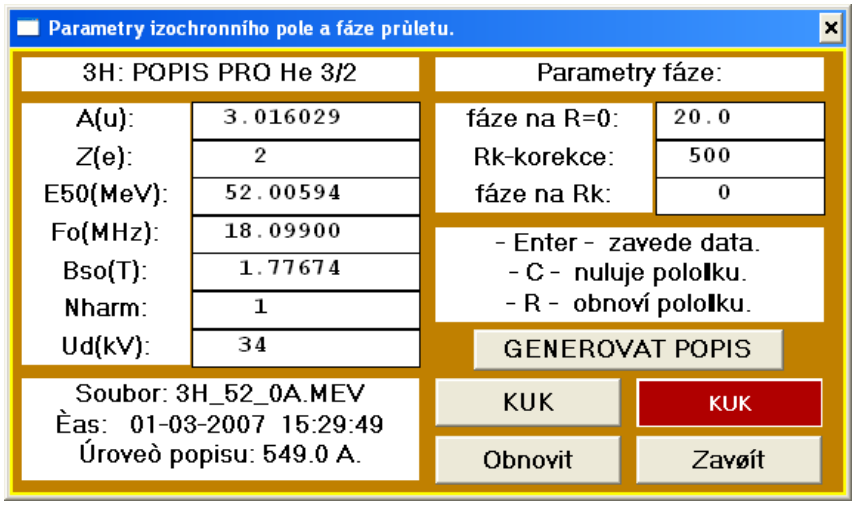

Figure 4.2: WModel particular description window of the optimized isochronous field properties. Credit [19].

4.1.2 Durycnm

Since the WModel mathematical matrix model of the U-120M calculates only average values of the cyclotron parameters a software module for calculation of detailed beam properties has been developed. Beam dynamics simulation code Durycnm incorporates 2D magnetic field maps expanded from the WModel optimizer output, a detailed 3D electric field of the dee and a contribution from the harmonic coils. The purpose of the code is to optimize the acceleration process and to analyze the beam properties during its acceleration and extraction.

The Durycnm program calculates 3D trajectories of ions accelerated in an arbitrarily chosen accelerating regime with a large variety of initial conditions. The relativistic equations of motion in the orthogonal coordinates are solved in 3 dimensional phase space (x, x', y, y', z, z') with the time as an independent variable by the four order Runge-Kutta method [52]. The integration step is the time that corresponds to the RF phase step 0.1° in the injection region and 0.5° in the further course. Actual values of magnetic field components B_x, B_y, B_z and electric field components E_x, E_y, E_z are calculated at each step [21]. The program continuously calculates the position and velocity components, RF ion phases at the moment of the ion pass through the acceleration gap, centres of the orbits of particular ions or of the whole beam, their energies and, if required, also their radial and axial emittance, beam profiles, energy dissipation, space distribution and radial density of the ions in the beam at a given radius [20]. Configuration of the electric

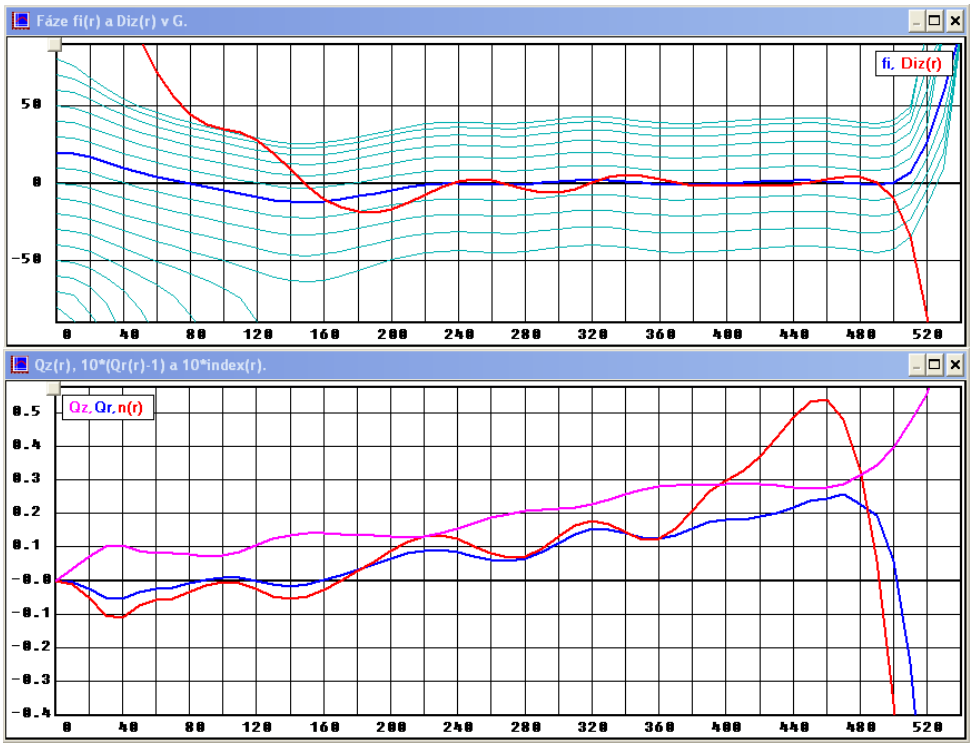

Figure 4.3: Top window: Phase evolution (blue), Bottom window: betatron oscillations (red, blue) and field index (magenta). Details are given in the text. The x-axis is radius in mm. Credit [19].

field distribution in the central region and the ion trajectory after leaving the ion source slit is shown in Fig. 4.4.

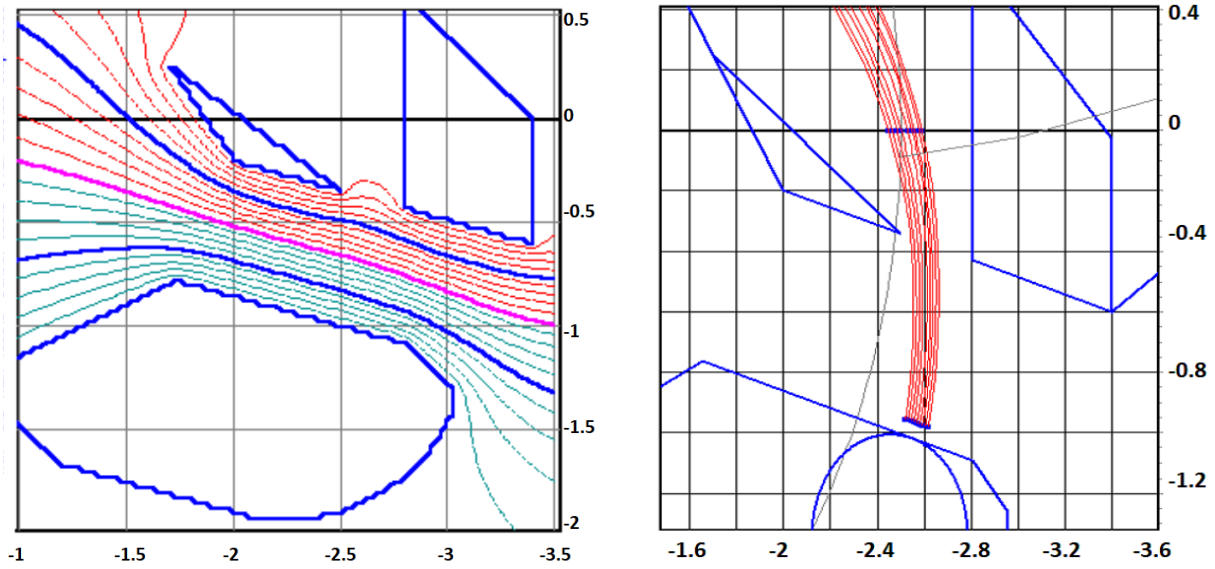

(a) Electric potential

(b) Beam tracks

Figure 4.4: Electric potential at the ion source slit (a) and beam tracks before entering the puller (b) used in calculation in Durycnm. See text for further details.

Durycnm extraction simulation

For the negative particle beams, the program shows excellent agreement with the measured data verified by measurements of parallel reactions $^{nat}Cu(p,X)^{62}Zn$, ^{63}Zn, ^{65}Zn on thin copper foils [20] with very good correlation (R>0.999) and statistical average energy deviation only 175 keV. The extraction process is simulated by means of semi-automated algorithm which finds optimal stripping foil position and a correction magnet current to pass the beam to a beamline quadruple triplet entry. The reliability of the algorithm has been verified by many years of practice and requires only a slight manual correction by the cyclotron operator. Example of the algorithm output is in Fig. 5.32.

Although the capabilities of the Durycnm program to simulate the extraction of negative ions are very good, similar quantitative agreement is lacking for positive ions. The process of extraction through an electrostatic deflector is solved only approximately by introducing an analytical electric field acting on beam of particles in a certain azimuthal range at a selected radius. Since the program processes information about the properties of the magnetic field only up to a radius of 60 cm, its possibilities to simulate the extraction process of the positive beams are rather limited.

4.1.3 SNOP

The beam dynamics simulator SNOP is well established code used for supporting design of small cyclotrons and for analysis of the beam properties of the existing cyclotron facilities by a number of laboratories. Its functionality has been verified on several real accelerators [51, 71] and during the construction of the ultra-compact cyclotron ION-12SC [74]. The program uses 3D electric and magnetic field maps, calculates beam space charge effects and analyses beam losses on structural elements of the accelerator. The SNOP calculates trajectories of particles in the electromagnetic fields by solving a complete system of the equations of motion without any simplification. It uses the classical fourth order Runge-Kutta method to solve the system of the equations [72]. Fig. 4.5 shows an internal structure of the program. The acceleration process is divided into four steps covering the injection line for external ion source, the inflector region, the cyclotron region and the extraction region. For all regions it is possible to import 3D geometry for calculation of the losses and field maps of the individual accelerator components. All the simulations performed in this thesis start in the cyclotron region and the initial beam parameters are defined on the ion source slit for beam currents up to 50 μA, where the space charge effect is negligible. The geometry defined in the cyclotron region consists of the central region 3D model of the ion source and puller, the geometry in the extraction region consists of 3D models of the electrostatic deflectors and magnetic channels. Electric and magnetic field maps used in SNOP simulations are discussed in the next sections.

4.2 Magnetic fringe field

The cyclotron magnetic field is well known up to a radius of 600 mm from the previously performed magnetic field measurements and the mathematical model WModel. The radius covered by the measurement is sufficient to investigate the behavior of the beam during acceleration and in the initial part of the beam extraction. Since the extraction process involves the study of the behavior of the beam up to a radius of 800 mm, where the beam leaves the accelerator chamber and enters the beamline, a fringe field in the

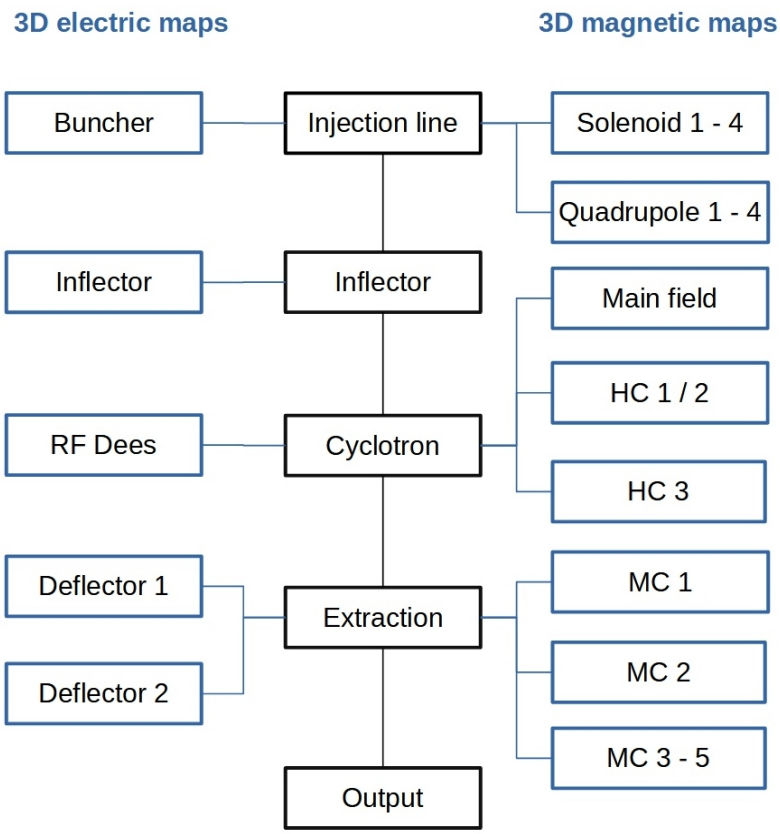

Figure 4.5: Internal structure of the SNOP simulator.

region of 600 – 800 mm has to be created. For this purpose, I created a 3D CAD model of the magnetic circuit, which is based on the drawings supplied with the U-120M cyclotron.

4.2.1 Cyclotron magnet model

The CAD model consists of a model of the steel AISI 1010 [45] body magnet yoke excited by a pair of the main magnet coils and of a CAD model of the spiral sectors of the cyclotron placed on the support disc.

Calculation of the magnetic field in the model median plane is carried out in the numerical simulator Opera [66] for four levels of the main coils excitation covering the mean magnetic field range 1.1 – 1.8 T . The magnetic fields produced by the simulator are evaluated in a radial range of 450 – 800 mm. By interpolation of the two neighbouring field levels a map of the fringe field is obtained for any level in the simulation range. Resulting simulated radial fringe field profile slightly differs from a fringe field profile measured along the H- beam line at azimuth 270°. This is the only azimuth where the field is known in detail by previous measurement in radii 0 – 1000 mm.

The difference between the two fields, see Fig. 4.9a, probably originates from the fact that the numerical model of the magnetic system consists only of the magnet itself and does not include surrounding parts of the cyclotron infrastructure. Various supporting elements of the cyclotron such as probe holders, beam line supports, cable platforms and an axial injection test stand are made of high permeability steel. Magnetic properties of these surrounding objects may influence the final shape of the fringe field and lead to the observed inconsistency between the simulations and the measurement.

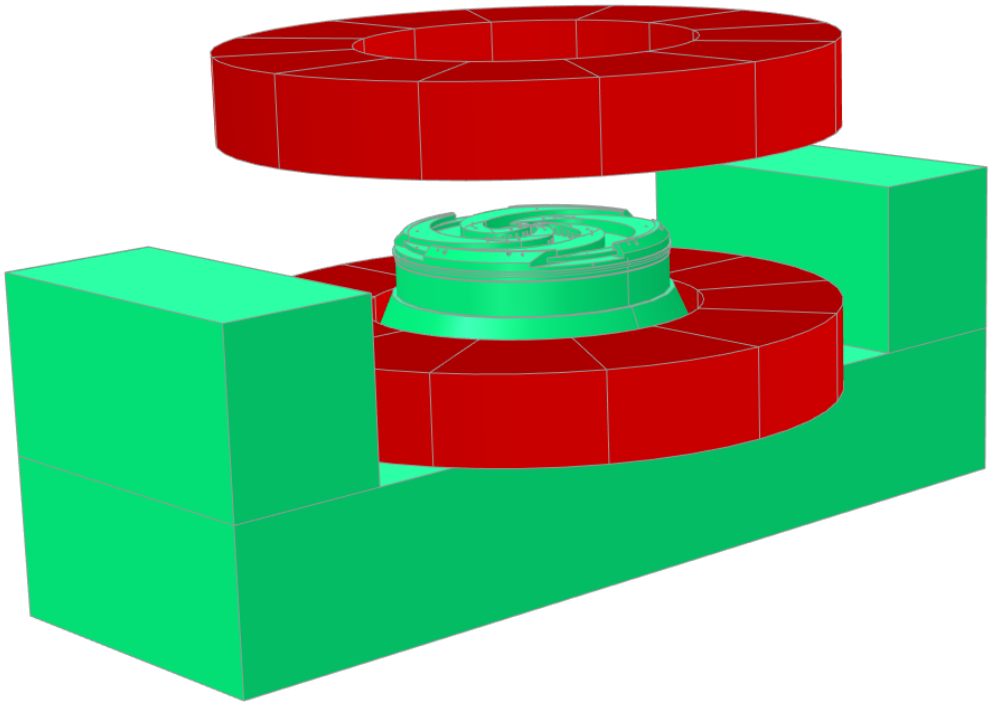

Figure 4.6: The lower part of the U-120M magnet Opera model. The main coil has red color.

4.2.2 Resulting field map

To obtain final isochronous field map RM in a default resolution [721×801] covering the full investigated radii range $r = 0 - 800$ mm for a specific particle and its energy, the simulated fringe field map SF ($r = 600 - 800$ mm) needs to be fitted for a specific isochronous magnetic field map of interest MM, i.e. a basic map. The basic map MM [121×121] is produced by the mathematical model Durycnm with resolution 3° azimuthally and 5 mm radially and is interpolated by cubic interpolation to a default resolution with step 0.5° in azimuth and 1 mm in radius.

The resulting field map RM is created by combining the original map MM and a modified fringe field map MF

$$RM(az, r) = MM(az, r_1) + MF(az, r_2), \tag{4.4}$$

where azimuth index az covers full angle $0 - 360°$, radius index r means full radius 0 – 800 mm, index $r_1 = 0 - 600$ mm covers the radial range of the basic map and index r_2 is the fringe field region 600 – 800 mm. The simulated SF map is scaled to the same value of mean induction as the basic MM map at radius $r = 600$ mm with a scaling factor

$$sc = \overline{MM}(r)/\overline{SF}(r). \tag{4.5}$$

Then the scaled SF map is modified by a function F reflecting the measured radial profile of the fringe field

$$MF(az, r_2) = F(r_2) \cdot sc \cdot SF(az, r_2), \tag{4.6}$$

where the modification function F is obtained in radial range $r_2 = 600 - 800$ mm as a

ratio of the measured radial profile EF related to the basic map MM and the scaled fringe field profile at azimuth 270°

$$F(r_2) = EF(270°, r_2)/(sc \cdot SF(270°, r_2)). \tag{4.7}$$

The final isochronous map RM then combines the original cyclotron field map MM which stayed untouched and the fringe field resulted from the Opera simulations with the radial profile corresponding to the profile obtained by the measurements. The maps created in this way for individual acceleration regimes are imported into the SNOP code and are used in the extraction simulations.

An example of final field map for $^3He^2$ ion and final energy 52 MeV is shown in Fig. 4.7. Azimuthal field profile for several radii is shown in Fig. 4.8.

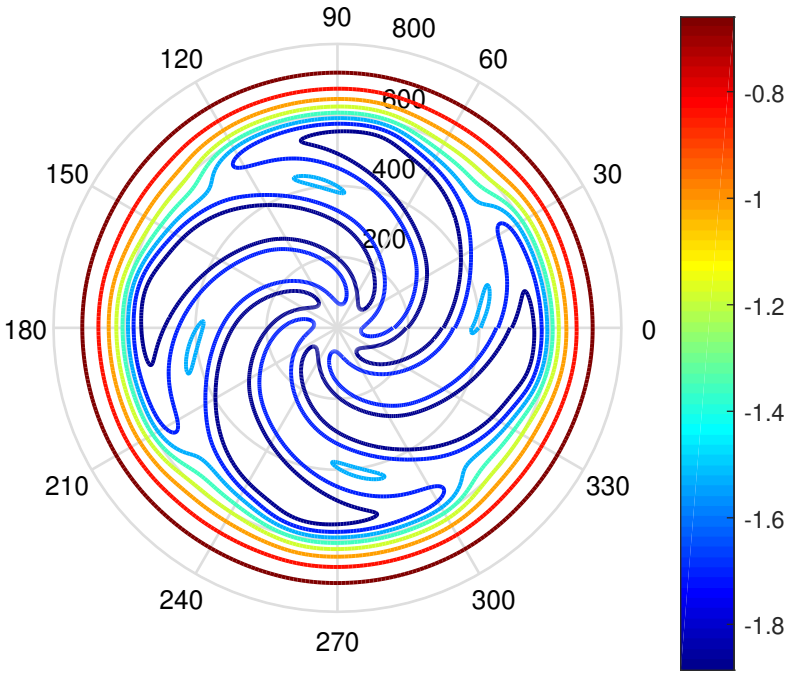

Figure 4.7: Magnetic field map for $^3He^2$ at 52 MeV including the fringe field. The color scale is in Tesla.

Figure 4.9a shows the mean magnetic induction radial profile for the field with and without the modification by the function F. The difference at the outer radius reaches 8.7 % and the beam dynamics simulations show a minimal effect on the extracted beam. The modification function F for this particular case is shown in Fig. 4.9b.

4.3 Electric fields calculation

As for the magnetic field, the 3D simulation software Opera [66] was used to calculate the electric field for the acceleration region and for the electrostatic deflectors. The source models are created in Autocad Inventor [7] and imported into the simulator. The 3D CAD models of the currently used deflectors are based on drawings of the original extraction system. Models of the new deflectors are created and modified according to the needs based on the performed simulations. The current configuration of the accelerating

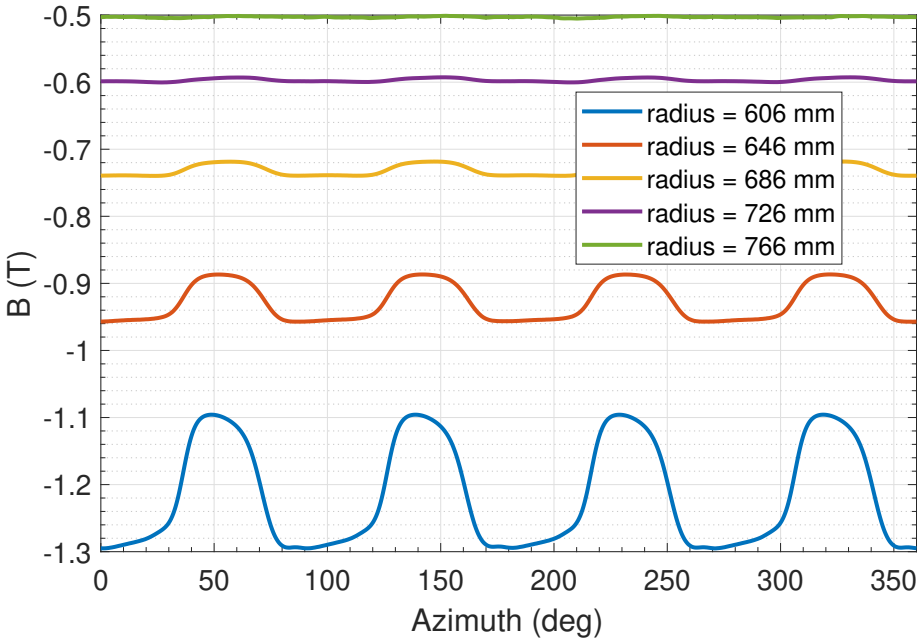

Figure 4.8: Fringe field profile along azimuth at several radii.

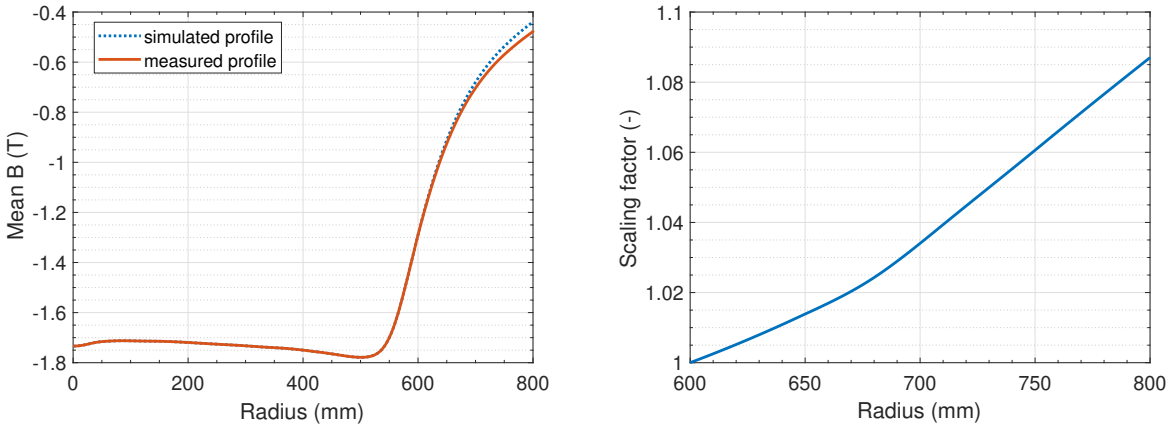

(a) Mean magnetic induction.

(b) Fringe field coefficient function.

Figure 4.9: Mean induction radial profile and the fringe field coefficient function used for field correction. See text for further details.

Table 4.1: Mesh sizes for electric field calculations.

Region	Mesh size (mm)
IS slit	0.2
Puller	0.5
Central region r $<$ 40 mm	1
Acceleration region r $>$ 40 mm	1.6

electrode and especially the puller underwent many changes during the operation of the cyclotron. The 3D CAD model used in the simulations reflects these changes and is based on the most recent drawings and measurements made on the physical element.

The geometry of the central region of the cyclotron determines the centering of the beam in the first few revolutions and thus influences the behavior of the beam during the entire acceleration process. During the design of the geometry of the central region, special consideration must be given to the position and shape of the accelerating electrodes with regard to minimize the amplitudes of free oscillations of the particles and to preserve the focusing properties of the electric field in the vertical plane [62]. The situation with the modeling of the central region on the U-120M cyclotron is simplified in the sense the accelerating electrode and the central region related to it are already constructed and in the long-term operation. However, although the geometry of the puller and the ion source that form the central region is well known, their relative position changes during cyclotron operation. Since the relative ion source position with respect to the puller is one of the main parameters of the cyclotron optimization during its operation, the configuration of the central region for the needs of simulations of the accelerating process is only estimated. The estimation is based on indirect measurements of the distance of the ion source from the puller during short-term shutdowns of the cyclotron.

A great emphasis was put on the area of the ion source slit and the area of the first turns of the ions. Overview of the mesh sizes used for the central region and for region with greater radii are presented in Table 4.1. The configuration of the electric field distribution near the ion source slit deserves special care and the next subsection is devoted to it.

Fig. 4.10 shows the configuration in the central region. Details for the ion source slit region are shown in Fig. 4.11a and Fig. 4.11c shows a cross section of this region in the vertical plane.

4.3.1 Beam initial conditions

During the first half-turn, the energy of the ions extracted from the ion source is low and their path is strongly influenced by the shape of the electric field in the close vicinity of the ion source slit and in the space between the ion source and the extraction slit of the puller. The phenomenon of the realistic electric field shape at the cold-cathode Penning Ion Gauge (PIG) [22] ion source slit was studied thoroughly during the design of the 250 MeV medical cyclotron for cancer therapy at MSU university [60, 26, 27], and confirmed experimentally during the cyclotron commissioning [9].

The emission of positive ions from a plasma surface can be simulated using the plasma sheath emission model. The plasma consists of positive ions and electrons closed inside a cavity in the ion source. Due considerably smaller mass and high temperature the

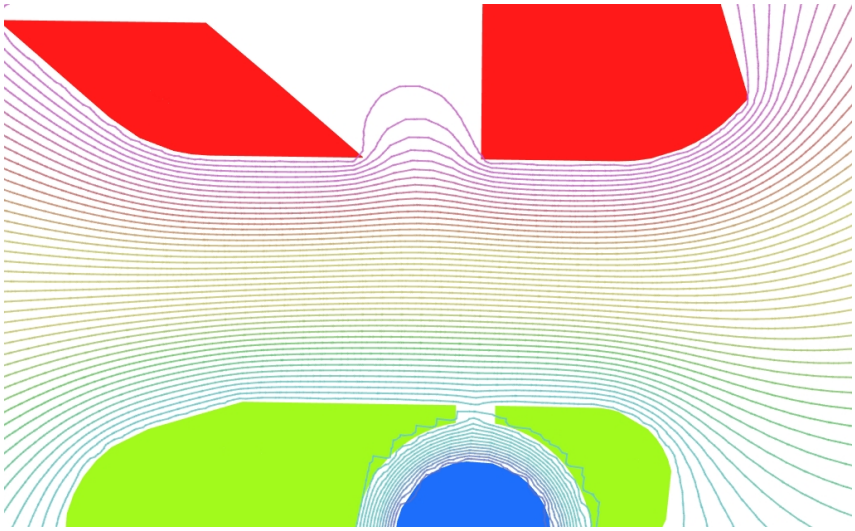

Figure 4.10: Electric field used in beam dynamics simulations. Distribution in the central region.

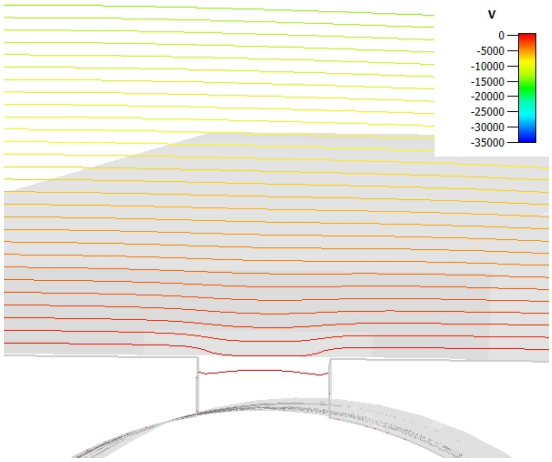

(a) Potential in horizontal plane

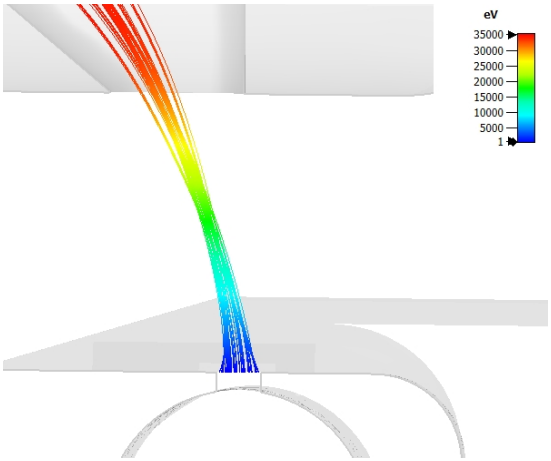

(b) Track in horizontal plane

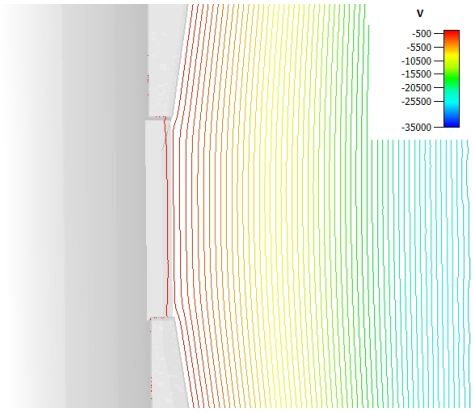

(c) Potential in vertical plane

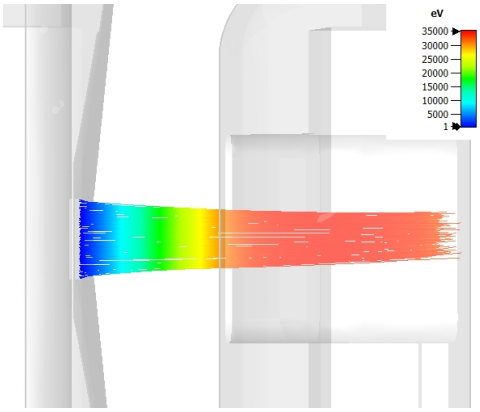

(d) Track in vertical plane

Figure 4.11: Electric potential at ion source slit (a)(c) and beam tracks before entering the puller (b)(d) for realistic slight concave plasma meniscus ($w = 0.36$). The ion source is at the bottom in the horizontal plane figures and on the left in the vertical plane figures. See text for further details.

electrons in the plasma tend to build up a negative charge at the walls and an associated plasma potential gradient from the wall to the plasma core. This potential gradient results in electric potential drop inside the so-called plasma sheath region [55].

For the PIG ion source, the chimney volume contains the electrically neutral plasma and the positive ions are extracted from the chimney opening towards the puller – the ion source *slit*. The plasma surface from which the ions are extracted is an near-zero equipotential surface, the so-called plasma boundary. Ions inside the boundary are assumed to be shielded by the plasma charge from the electric field produced by the puller [60]. The conditions under which the PIG source is operated determine the shape of the plasma boundary. Depending on the intensity of the extracted current and the plasma potential, the plasma boundary can have a concave, a convex or a flat shape. The shape of the plasma boundary defines the potential lines of the electric field in the vicinity of the ion source slit and thus directly determines the path of the extracted ions. In the horizontal plane, with a concave shape of the boundary, the ions are focused very soon after extraction see Fig. 4.12a and 4.13a, with a convex shape of the boundary, they are defocused see Fig. 4.12e and 4.13e, and for a flat shape, their trajectories are parallel, see Fig. 4.12c and 4.13c. In the vertical plane, the effect is similar, only less pronounced.

4.3.2 Plasma boundary estimation

For the U-120M cold cathode PIG ion source the three possible shapes of the plasma boundary are simulated using CST Particle Studio [67]. The electrostatic model includes the plasma indirectly by introducing so-called image electrode. This electrode is introduced as a cylinder created along the ion source chimney vertical axis with potential $V_I = wV_0$, where V_0 is the dee potential and w weight factor $0 < w < 1$. It is worth to mention that the image electrode does not represent any physical object, it is just a virtual electrode used in the simulation providing a continuous electric field derivative at the plasma boundary. The Fig. 4.10 shows horizontal cross section of the U-120M central region and the electric potential distribution. In this figure, the image electrode is the round electrode (blue) in the PIG ion source (green) chimney. The puller (red) is the top structure. Resulting beam behavior for weight factors $w = 0.1, 0.55$ and 0.86 is shown in Fig. 4.12 in the horizontal plane and in Fig. 4.13 in the vertical plane.

According to [9] the most probable shape of the plasma boundary is the slight concave profile with the beam focusing between the puller and the ion source slit. For the U-120M PIG ion source this situation corresponds to the weight factor approximately $w = 0.36$. The potential distribution and the beam behavior for this weight is shown in Fig. 4.11. Identical configuration is used for the Opera calculator [66] to calculate the electric field used in beam dynamics simulation in SNOP [72]. A comparison with Fig. 4.4 shows that the use of a flat plasma boundary in the electric field of the central region in the Durycnm simulator (section 4.1.2) is rather optimistic with regard to the behavior of the beam after extraction from the ion source.

It would be appropriate to study the central region of the U-120M cyclotron in more detail, as it can be assumed that the current geometry could be further optimized as shown in section 5.5. It follows from Ref. [81] that slight changes in the configuration of the central region, especially the dimensions and shape of the output slit of the ion source in the order of tenths of a millimeter, have a fundamental effect on the quality of the beam and the intensity of the extracted current.

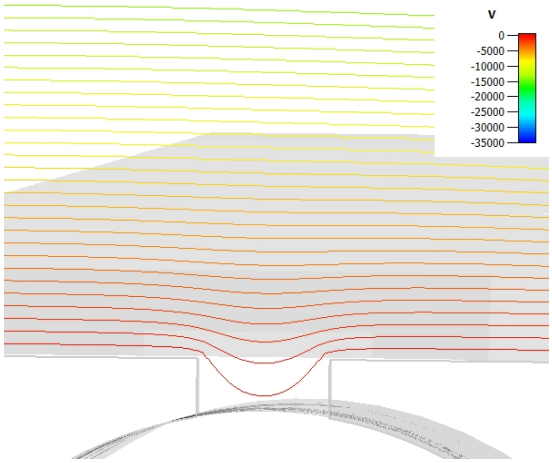

(a) $w = 0.1$

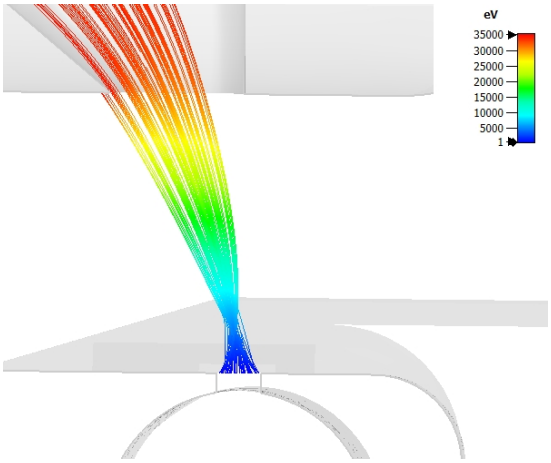

(b) $w = 0.1$

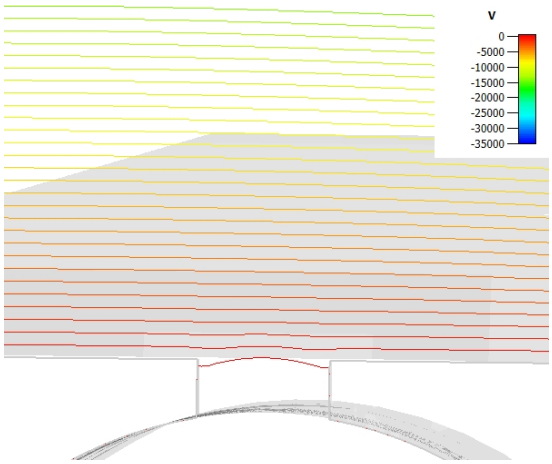

(c) $w = 0.55$

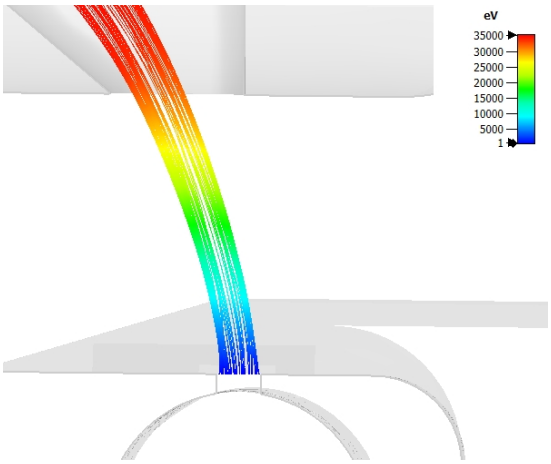

(d) $w = 0.55$

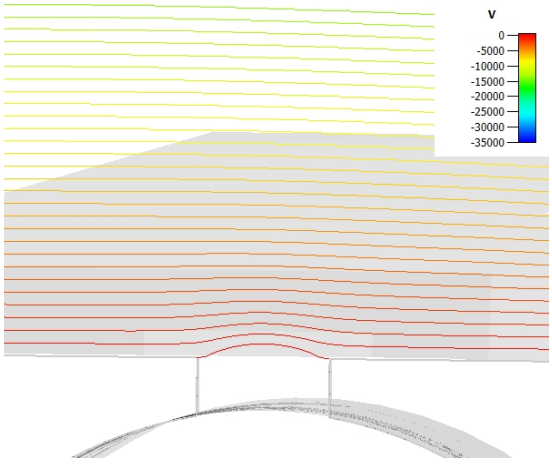

(e) $w = 0.86$

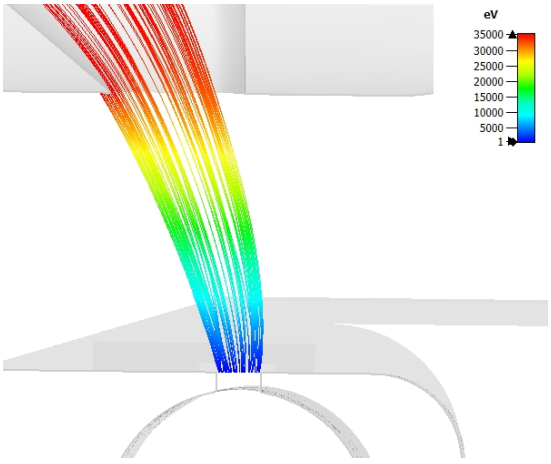

(f) $w = 0.86$

Figure 4.12: Electric potential at the ion source slit and beam tracks before entering the puller for concave $w = 0.1$ (a)(b), flat $w = 0.55$ (c)(d) and convex $w = 0.86$ (e)(f) plasma meniscus in the horizontal plane. The puller is the upper structure, the ion source is below. See text for further details.

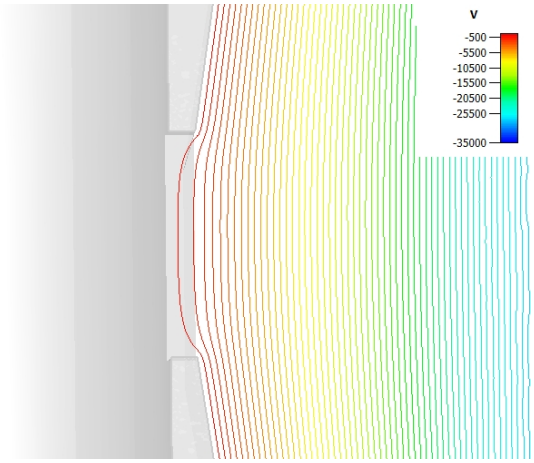

(a) $w = 0.1$

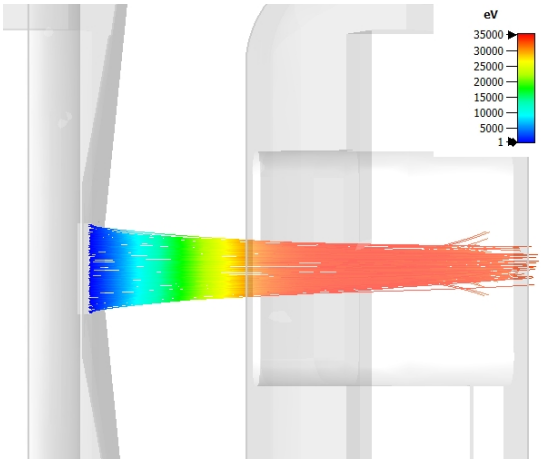

(b) $w = 0.1$

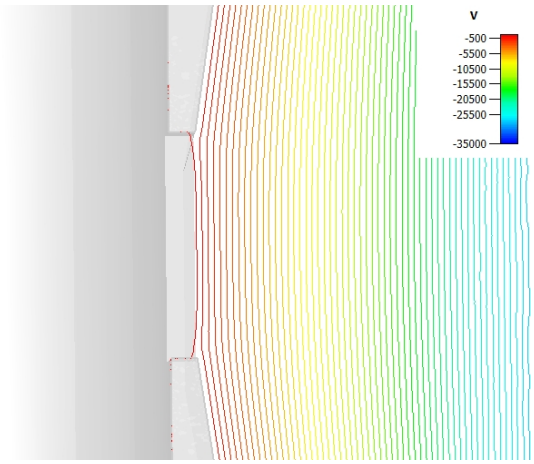

(c) $w = 0.55$

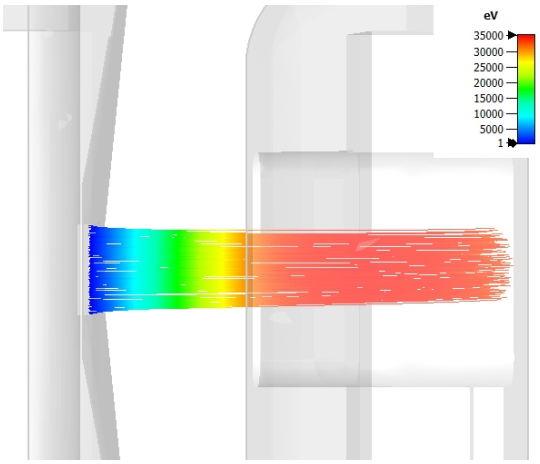

(d) $w = 0.55$

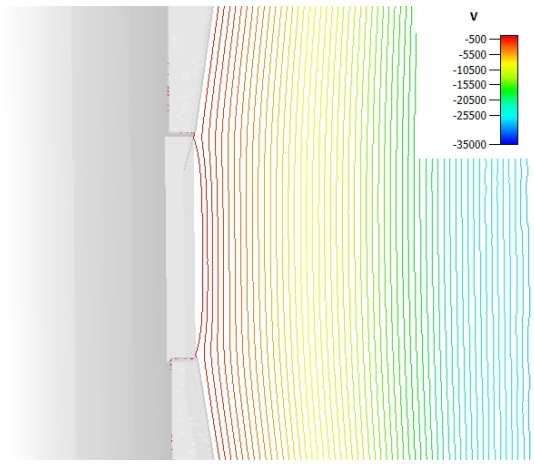

(e) $w = 0.86$

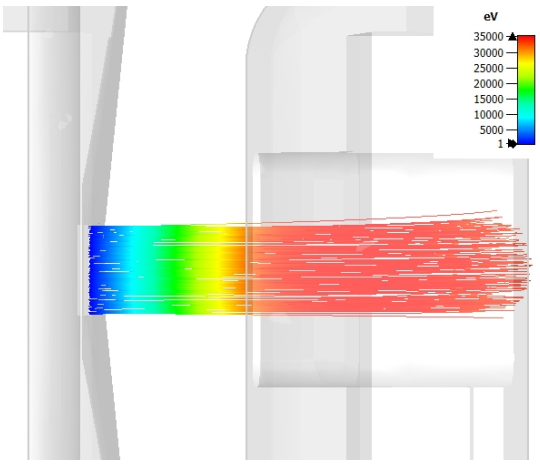

(f) $w = 0.86$

Figure 4.13: Electric potential at the ion source slit and beam tracks before entering the puller for concave $w = 0.1$ (a)(b), flat $w = 0.55$ (c)(d) and convex $w = 0.86$ (e)(f) plasma meniscus in vertical plane. The ion source is on the left, the puller is on the right. See text for further details.

5 U-120M Extraction system for positive ions

Originally, the extraction system of the U-120M cyclotron was designed by Z. Trejbal as a purely electrostatic regenerative system consisting of three electrostatic deflectors, an electrostatic exciter and an electrostatic compensator [70]. The efficiency of this system was very good and, according to the available information [38], reached up to 60% in most modes. However, the operation of the electrostatic exciter, which required high electric field strengths for satisfactory operation, encountered serious problems. During the extraction of particles of the highest energies, when the electric potential required to deflect the beam is the greatest, electrical breakdowns occurred between the exciter electrodes. Subsequently, the electrodes of the electrostatic compensator melted due to the high intensity of the incident beam, and the regenerative system of the electrostatic exciter and compensator were replaced by a single electromagnetic exciter. Since then, the extraction of positive ions has been struggling with very low extraction efficiencies in the range of $5-15\,\%$, depending on the type and energy of the extracted particles.

It is clear that the high amplitude of the first harmonic perturbation component of the magnetic field measured in the spring of 2022 was one of the causes of the very low extraction efficiency. The main goal of this dissertation is the design of such an extraction system that will enable an efficient extraction of positive ions. Thanks to the optimization of the horizontal position of the acceleration chamber and the associated reduction of the first harmonic disturbance discussed in section 3.3, and thanks to the design of new harmonic coils, it was possible to propose a system with an extraction efficiency close to $80\,\%$. In the following paragraphs, the current extraction system will be described and the procedure for designing a new system will be given.

5.1 Current extraction system

The current positive ion extraction system is composed of three electrostatic deflectors and an electromagnetic exciter as it is shown in Fig. 5.1. The entire extraction system is located in the azimuthal range of $182\,^\circ - 355\,^\circ$, i.e. in the space between the sectors of the cyclotron which is not occupied by the dee.

The structural arrangement of the elements for the operation of the cyclotron, i.e. the supply rods of the ion source and the beam current probes, define the areas for the placement of the individual extraction system elements. Azimuthal positions and radii of influence of individual parts of the extraction system are listed in Table 5.1. Electromagnetic fields and mechanical properties of the individual elements are described in the next paragraphs.

Table 5.1: Positions of individual parts of the extraction system.

Extraction element	Start azimuth	Azimuthal length	Radius of action
EM exciter	182°	23°	∼ 500 mm
Deflector I	210°	58°	∼ 500 – 540 mm
Deflector II	272°	23°	560 – 580 mm
Deflector III	305°	50°	580 – 700 mm

Figure 5.1: Configuration of the actual extraction system. EB – electromagnetic exciter, I. – III. Electrostatic deflectors. The beam orbits from right to left.

5.1.1 Electromagnetic exciter

The electromagnetic exciter – a bump coil – is a dipole electromagnetic coil designed to excite coherent oscillations in the accelerated beam and create separation between turns at the extraction radius. Ideally, the exciter coil would be mirrored on the opposite azimuth and connected in reverse polarity such that its contribution to the mean magnetic field along the azimuth is zero. Since the exciter used in the U-120M extraction system consists of only one coil, its contribution to the mean magnetic field is not compensated. This causes a deviation from the isochronism of the magnetic field and a slight phase shift of the accelerated particles. According to the available literature, this phase deviation is of little importance for a very well-centered beam, but with imperfect centering, it can increase the energy spread of the extracted beam and its transversal profile, which is usually undesirable [71].

Contribution of the exciter to the cyclotron magnetic field is shown in Fig. 5.2. The first harmonic component amplitude and phase of the exciter magnetic field contribution is shown in Fig. 5.3.

5.1.2 Electrostatic deflectors

The electrostatic deflectors used in the U-120M cyclotron are one of its most problematic components. In addition to the fact that their efficiency is very low, their operation and maintenance are associated with several very serious shortcomings. Probably the most serious complication is the practically limited possibility of maintenance, which is due to

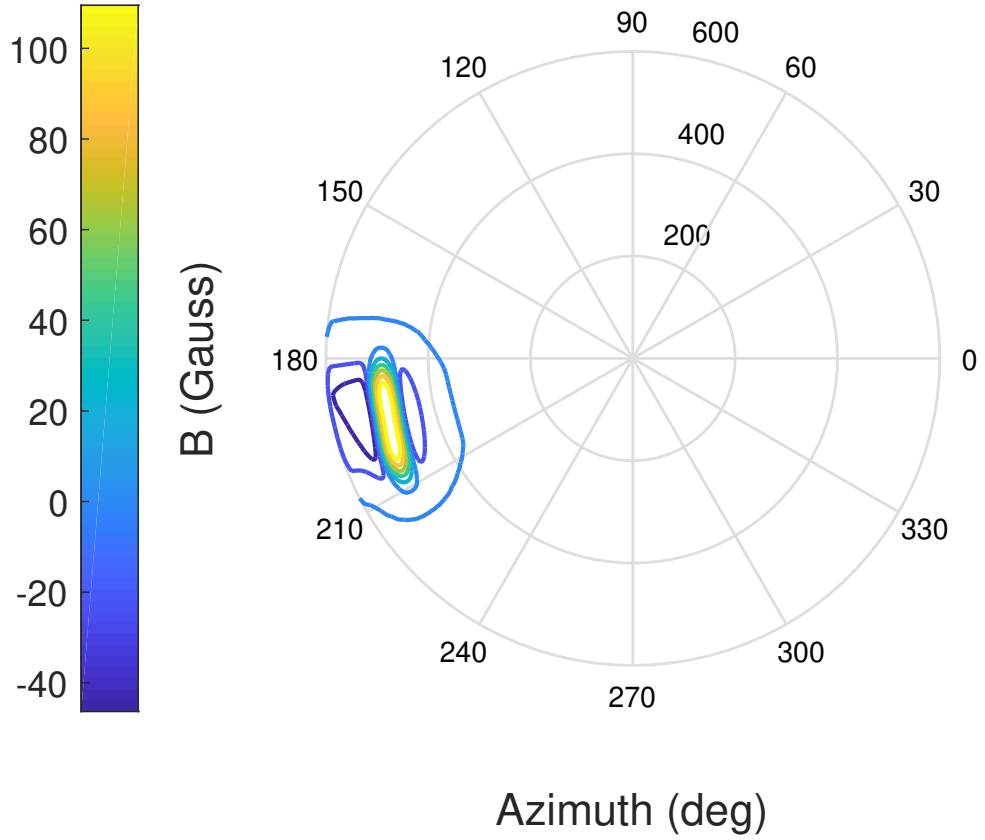

Figure 5.2: Electromagnetic exciter magnetic field contribution to the main cyclotron field.

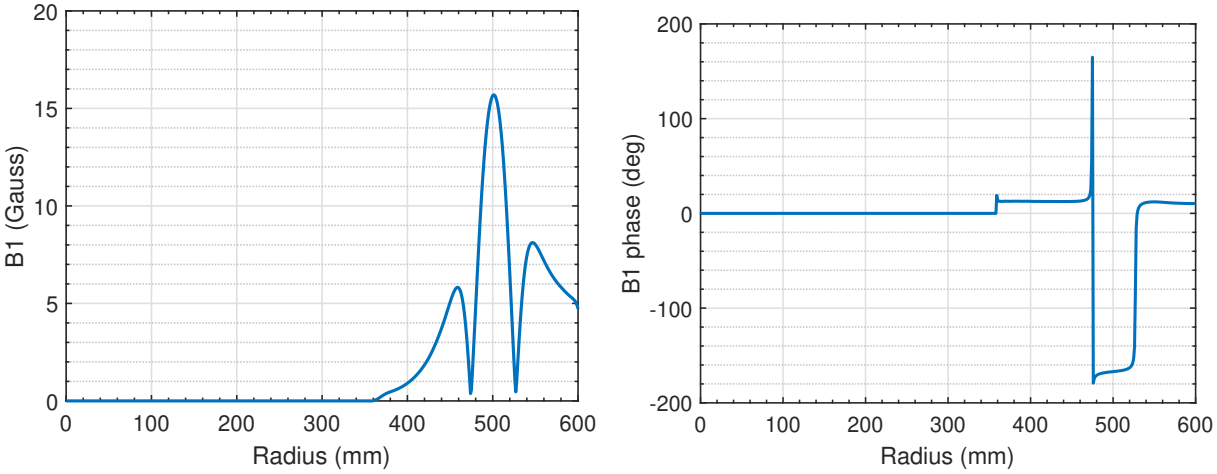

(a) (b)

Figure 5.3: Amplitude (a) and phase (b) of the first harmonic component of the electromagnetic exciter magnetic field contribution.

their considerable radioactive activation. The first deflector, whose task is to separate the extracted part of the beam from the beam orbiting in the acceleration space, is naturally activated the most. When removed from the accelerator chamber immediately after the positive ion experiment, it is common for the septum of the first deflector to have a dose rate of 150 – 200 mSv/h at the surface and the activity does not drop below 10 mSv/h for several weeks. Any maintenance on the just removed first deflector is practically impossible for a few days.

Another complication during operation is that especially the first and third deflectors are very susceptible to plating of high voltage insulators, which limits their service life. In experiments with the highest extracted ion energies, the first deflector has problems maintaining the necessary voltage, leading to frequent discharges and the release of metal vapors into the vacuum chamber. These vapors settle on the high voltage insulators and reduce their insulating properties. A longer training period and a slow build-up of the high voltage on the electrodes allow operation in the range of three to five days. After this time, the leakage current of the insulators is so large that the high voltage source is unable to maintain the necessary voltage on the high voltage (HV) electrode, and the insulator must be cleaned or replaced.

For the needs of numerical simulations of beam dynamics during the extraction process, I created 3D CAD models of electrostatic deflectors based on the available plans supplied with the cyclotron. However, during almost half a century of operation, the design of all three deflectors underwent a number of minor changes. For the most part, these changes related to the supporting mechanical parts, i.e. the routing of high voltage leads and insulators, the attachment of electrodes and the system of changing the position. By measuring the dimensions of the electrodes, I verified that their shapes have been preserved and are consistent with the original designs. In the 3D CAD model the bending radii of the HV electrodes are based on the drawings of the deflectors, the cross-sections of the electrodes and their azimuthal lengths and relative positions are based on measurements of the actual condition.

The 3D CAD models of the deflectors are created in Autodesk Inventor [7] and include only the high voltage electrodes and septa. The drive support mechanisms and electrode holders are not included in the models, as they do not affect the resulting electric field. The electrostatic solver in Opera [66] is used to calculate the electric fields of the deflectors and create their maps in a format suitable for the SNOP simulator [72]. For the correct function of the maps imported into the SNOP, all electric fields are calculated for a positive potential of +1 V on the HV electrode of the deflectors. The maps created in this way are subsequently multiplied in SNOP to achieve the desired deflectors voltage. Potential of the septa is 0 V in all cases reflecting the septa are grounded electrodes.

Deflector I

The first electrostatic deflector, i.e. Deflector I, is the only one from the set of three deflectors that inevitably comes into contact with the beam. Due to the insufficient separation of the orbits at the extraction radius, a certain part of the beam falls on the leading edge of the septum. To limit the power lost at this point, the leading septum edge is modified by a small V-shaped cut. This modification spreads the power loss from the incident beam over a larger area and to a considerable extent protects the beginning of the septum from melting. The Deflector I is show in Fig. 5.4 and the V–shaped septum is shown in Fig. 5.5.

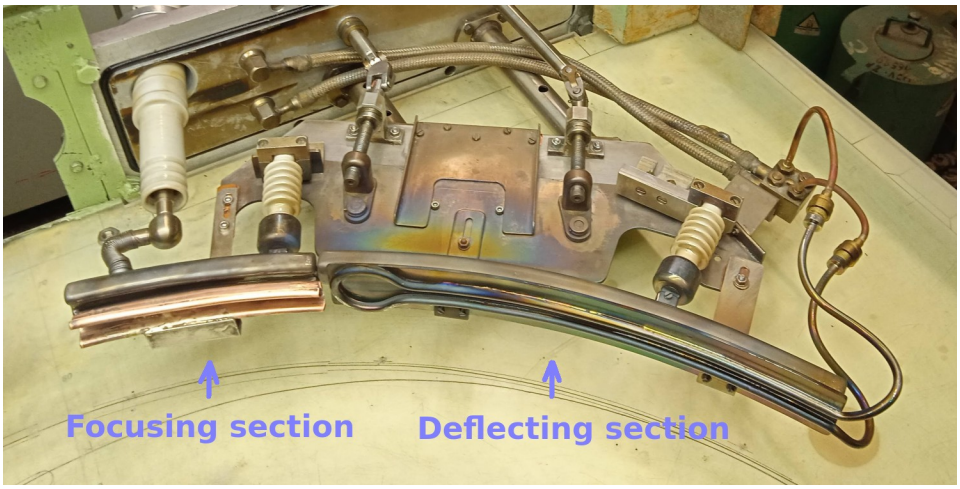

Figure 5.4: First electrostatic deflector.

Figure 5.5: V-shaped beginning of the first deflector electrostatic septum.

The deflector is divided into two consecutive parts. The first non-focusing part has the azimuthal length of 40°, and the high voltage electrode and the septum electrode have a simple shape in the space through which the beam passes. In this part which is designed as purely deflecting, a homogeneous electric field is generated by the plate shape of both electrodes. The homogeneity of the electric field is disturbed only at the beginning of the deflector where the septum is modified by the V–shaped cut. Through this septum opening the electric field emerges to the lower radii and affects the beam at lower orbits. The effect is small but not insignificant. Figure 5.6 shows the top view of the Deflector I beginning together with the electric field leaking to the lower radii. The second part of the Deflector I has an azimuthal length of 18°. Electrodes in this part provide electric field which focuses the beam in the radial direction.

The potential distribution at the beginning of the deflector and in its focusing part is shown in Fig. 5.7. The course of the electric field and its gradient shown in Fig. 5.8 is investigated in the middle plane along the line dividing the focusing part of the deflector into two halves, i.e. 9° from the end of Deflector I for the potential on HV electrode $-75\,\mathrm{kV}$, which corresponds to the maximum voltage the deflector is usually able to sustain. The distance coordinate on the x axis is calculated from the septum electrode to the HV electrode. The azimuthal lengths, gap sizes and a mean gradient of the electric field of the

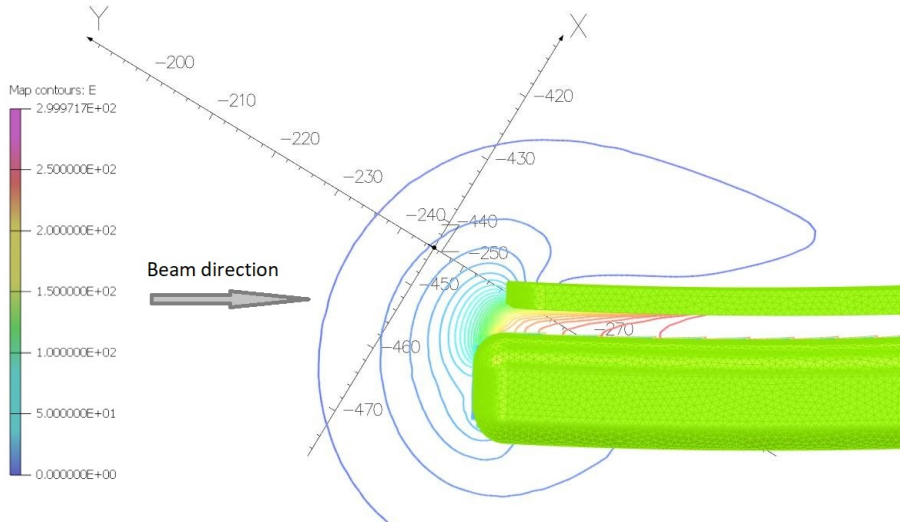

Figure 5.6: The electric field E(V/m) distribution at the beginning of the Deflector I for HV electrode potential +1 V. The direction of the incident beam is indicated by an arrow.

Deflector I individual sections are listed in Table 5.2. It is worth noting that before each experiment with the deflectors, the gaps are adjusted individually as needed. The gap values given in the table are therefore approximate and may vary by tens of percent for individual experiments. The CAD model of the Deflector I has the gap in the deflection section 4 mm and in the focusing section 7.1 mm.

Table 5.2: Properties of individual sections of Deflector I.

	Deflecting section	Focusing section
Azimuthal length	40°	18°
Gap size	∼ 4 mm	∼ 8 mm
Septum bending radius	627 mm	538 mm
Septum height	44 mm	31 mm
Septum thickness	0.3 mm	1 mm
Electrode bending radius	633 mm	549 mm
Electrode height	32.8 mm	32.8 mm
Maximum operating voltage	∼ −75 kV	
Mean electric field gradient	–	84 kV/cm^2

Deflector II

The second electrostatic deflector, i.e. Deflector II, has an electrode profile different from the two remaining deflectors. The radial gap is not limited by the distance between the septum and the HV electrode, since the HV electrode is made up of two parts with a vertical gap of 9.6 mm, see Fig. 5.9. Fig. 5.10 shows the potential distribution between the electrodes for +1 V on the HV electrode. Such an arrangement of electrodes generates

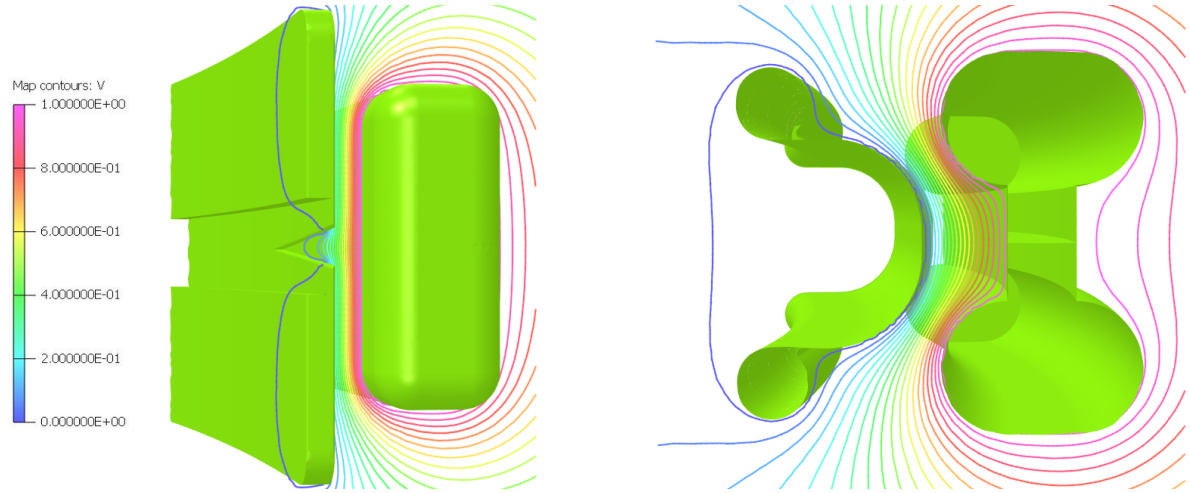

(a) V–shape region (b) Focusing region

Figure 5.7: Electric potential distribution inside Deflector I at azimuths of the beginning of the deflector and of the focusing part for HV electrode potential +1 V. The color scale is in Volts and is common for both figures.

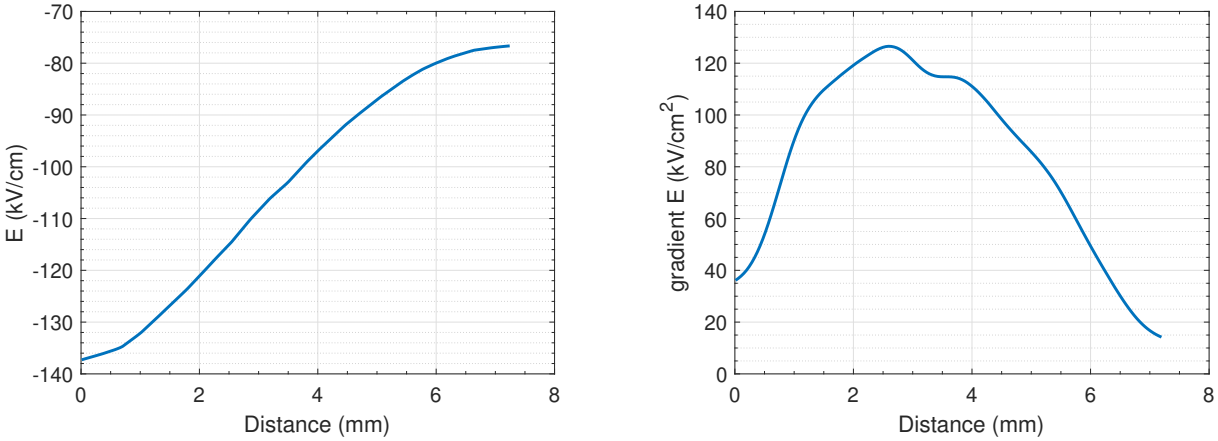

(a) Electric field (b) Electric field gradient

Figure 5.8: Distribution of electric field and its gradient between electrodes in the focusing region of the Deflector I for −75 kV at the HV electrode. Details in text.

an almost constant gradient near the septum, which is very convenient for adjusting the effect of the deflector on the beam. By gently changing the radial position of Deflector II, the degree of focusing of the beam entering the next deflector can be regulated. The courses of the electric field and its gradient in the center of Deflector II are shown in Fig. 5.11. The basic design and operational parameters are listed in Table 2.

The operation of this deflector is more or less problem-free. The design of the Deflector II allows for long-term operation without discharges, and the insulators also do not tend to quickly metallize. A small drawback is the absence of water cooling of the septum, which creates the possibility of melting in case of incorrect tuning of the beam extraction, as has already happened several times in the past.

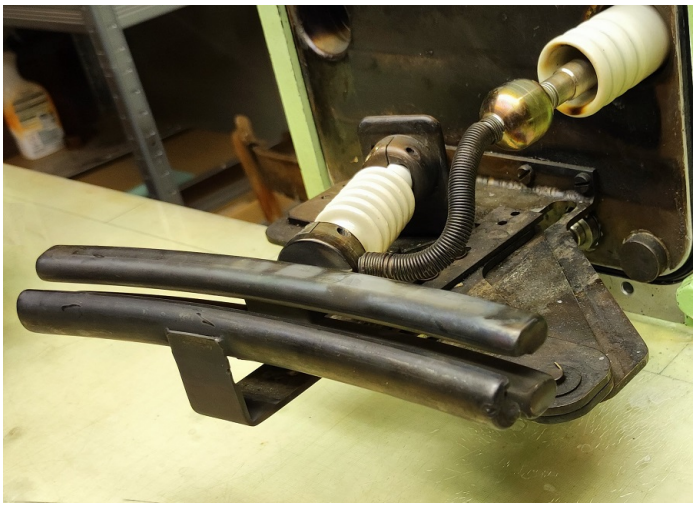

Figure 5.9: Second electrostatic deflector.

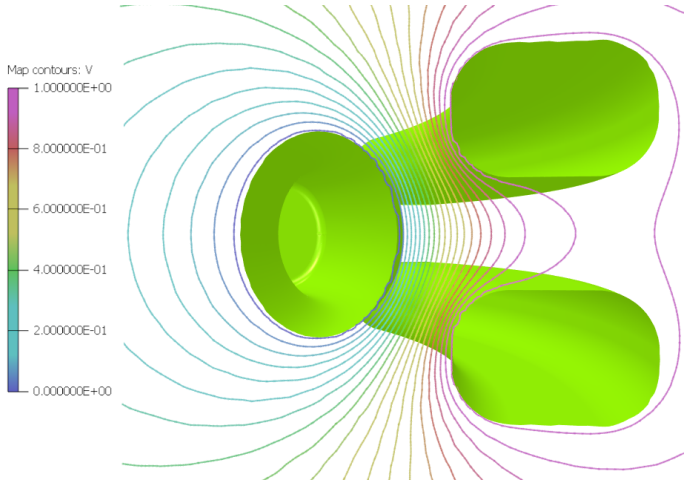

Figure 5.10: Electric potential distribution in the middle of the Deflector II for HV electrode potential +1 V. The color scale is in Volts.

Table 5.3: Basic properties of Deflector II.

Azimuthal length	23°
Gap size	~ 15 mm
Septum bending radius	572 mm
Septum height	18 mm
Septum widht	14 mm
HV electrodes bending radius	577 mm
HV electrodes height	11.4 mm
Vertical gap between HV electrodes	9.6 mm
Maximum operating voltage	~ -50 kV
Electric field gradient	42 kV/cm^2

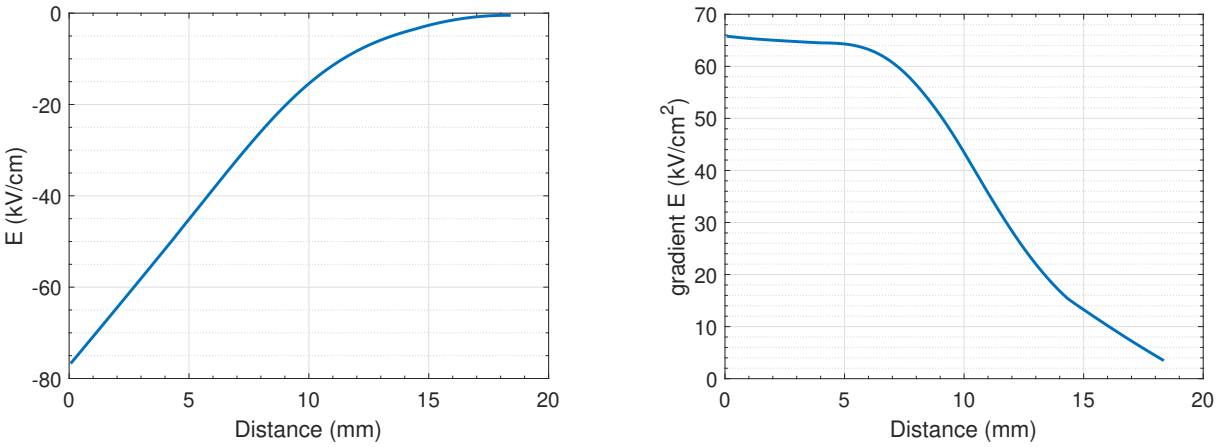

(a) Electric field (b) Electric field gradient

Figure 5.11: Distribution of electric field and its gradient between electrodes in the focusing region of the Deflector II for −50 kV at the HV electrode.

Deflector III

The third deflector, i.e. Deflector III, has a single section formed by profiled electrodes generating a focusing gradient of the electric field, see Fig. 5.12. Its bending radius is almost double that of the previous two deflectors, and the radial gap between the electrodes is approximately 12 mm, see Tab. 5.4. The distribution of the potential in the center of the deflector for +1 V on the HV electrode is shown in Fig. 5.13. The courses of the electric field and its gradient for a voltage of −50 kV on the HV electrode are shown in figure 5.14.

Neither the Deflector III has water-cooled electrodes or the septum. For that reason, an 8×8 mm cross-section collimator is placed at its entrance, which prevents the beam from hitting the deflector electrodes in the event of an incorrect operating procedure.

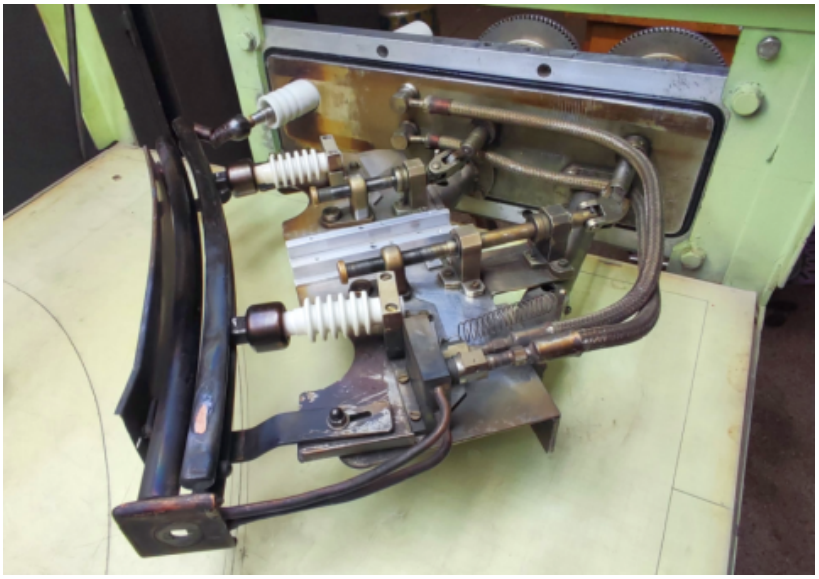

Figure 5.12: Third electrostatic deflector.

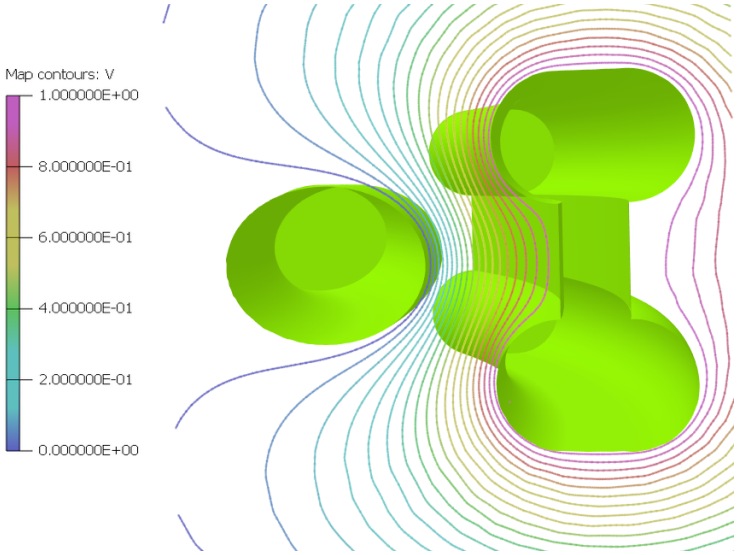

Figure 5.13: Electric potential distribution in the middle of the Deflector III for HV electrode potential +1 V. The color scale is in Volts.

Table 5.4: Basic properties of Deflector III.

Azimuthal length	50°
Gap size	∼12 mm
Septum bending radius	1026 mm
Septum height	14 mm
Septum widht	18 mm
HV electrodes bending radius	1037 mm
HV electrodes height	32.8 mm
Maximum operating voltage	∼ −50 kV
Mean electric field gradient	49 kV/cm^2

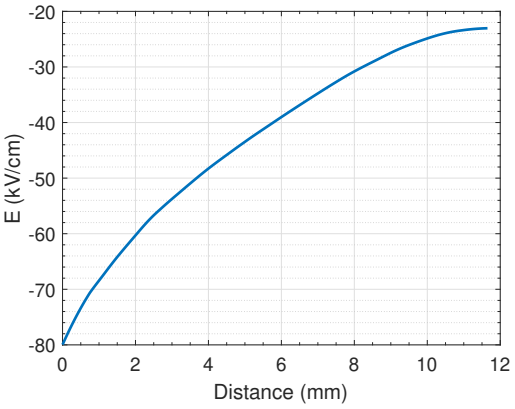

(a) Electric field

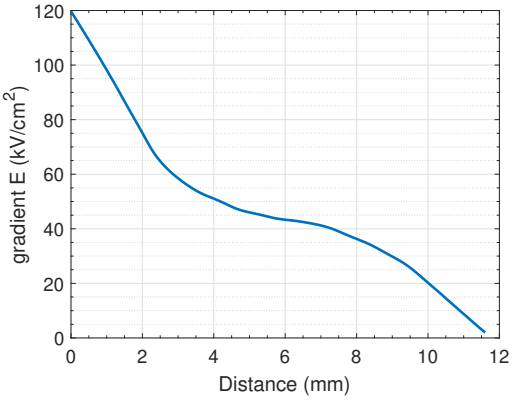

(b) Electric field gradient

Figure 5.14: Distribution of electric field and its gradient between electrodes in the focusing region of the Deflector III for −50 kV at the HV electrode.

5.2 Preliminary simulation of the extraction system

As mentioned in the previous text, the maximal efficiency of the positive ion extraction system is approximately 15%. The efficiency value is the ratio of the beam intensity measured before entering the deflection system and the beam intensity measured on the last current probe, i.e. the probe No. 4, before leaving the cyclotron chamber. Directly behind the probe No. 4 there is a horizontal magnetic dipole - a correction magnet (MK), with a vertical width of 18 mm, which adjusts the angle of beam entry into the subsequent beamline. As the beam progresses through the beamline, the extraction efficiency further decreases, as some parts of the beam hit the beamline walls or are absorbed by collimators. In the following text, I will therefore limit myself to the investigation of the transmission of the beam from the last orbit of the cyclotron to the current probe No. 4. A beam with a vertical dimension of less than 18 mm will pass through the MK dipole without loss and can be further processed during its passage through the beamline. The analysis of the beam behavior during the passage through the beamline is not a part of this dissertation.

By transferring the beam to the probe No. 4, I will define the overall extraction efficiency. Partial extraction efficiencies express the transmission properties of individual elements of the extraction system, and are given as a transparency of the individual elements. The transparency expresses the ratio of the intensity of the beam passing through the deflector to the intensity of the beam entering the deflector.

5.2.1 Calculations comparison

For a beam that will be accelerated to the extraction radius, but that will not pass into the deflectors, a basic comparison can be made between the two available beam dynamics calculators. For this comparison, the proton regime for 36.7 MeV with the main coil current of 502 A is selected. It is the maximum proton energy that is currently achievable on the cyclotron due to the frequency limit of the resonant system.

Since the Durycnm program does not allow the user to change the initial parameters of the accelerated beam freely enough, I define an particle with RF phase 0 ° and an initial position corresponding to the predefined parameters given by this program. I will subsequently introduce the initial particle defined in this way into the SNOP program and compare the outputs of both programs. Parameters of the initial ion are listed in Table 5.5. Position of the ion is listed in cylindrical coordinates related to the cyclotron center. The z coordinate refers to vertical coordinate above the cyclotron median plane and it is chosen to be 1.5 mm, i.e. at the top boundary of the ion source slit.

Table 5.5: Initial ion parameters for calculators comparison.

Radius	28.63 mm
Azimuth	−20.412°
Z	1.5 mm
Initial energy	50 eV
Dee voltage	34 kV
RF frequency	25.932 MHz
Starting RF phase (deg)	0 °

For the purpose of highlighting some interesting acceleration parameters and for showing the influence of the disturbance component of the magnetic field, i.e. the first harmonic component, the tested ion will be stopped at an azimuth of 0° and a radius of 515 mm. The achieved energy of the ion will be compared, its behavior in the vertical plane and special emphasis will be placed on the behavior of the centers of the orbits. A graphical representation of these parameters is shown in Fig. 5.15.

Because the Durycnm calculator uses a coordinate system where the x axis is aligned with the dee central symmetry line, i.e is rotated by 90° clockwise with respect to the SNOP coordinate system, the figures of the centers are rotated 90° anticlockwise to fit the SNOP coordinate system. Then the Durycnm output figures are reproduced in the resolution as produced on the screen by the program and supplemented with axis labels.

Table 5.6: Results for an arbitrarily defined ion. See text for further details.

Final radius at 0°	Calculator	Ion radius (mm)	Ion Energy (MeV)
500 mm	Durycnm	500.6	36.800
	SNOP	500.28	36.801
515 mm	Durycnm	516.2	38.785
	SNOP	517.8	38.76

The numerical values shown in Table 5.6 show good agreement of the obtained results. Energy values and thus the number of revolutions show minimal deviations. The radii reached by the ion after exceeding the radius of 515 mm differ by approximately 0.33 %. The course of the dependence of the Z-coordinate in Figures 5.15c and 5.15d indicates a slightly more optimistic course of the azimuthal focusing calculated in the SNOP calculator, by approximately 25 %. The Z-coordinate curves for both calculators show a strong vertical focusing just before reaching the 515 mm radius at 0 ° azimuth. Beyond this radius, there is a sharp increase in the vertical coordinate and the entire beam blows up and is completely lost vertically. From the moment when the ion trajectory passes through to enter the magnetic fringe field, its phase deviation from the RF phase of the accelerating voltage increases, as can be seen in Figures 5.15a and 5.15b. The RF frequency shift introduced in SNOP to obtain a minimum RF phase drift for the ion with the zero RF initial phase is −3 kHz, which corresponds to 0.012 % of the nominal RF frequency.

The graphs of the position of the center of the tracks also show a high degree of similarity, although there are easily observable deviations. In order to achieve a well-centered particle as in the Durycnm program, which is shown in Fig. 5.15e, it was necessary to slightly adjust the acceleration conditions in the SNOP program. For the centering shown in Fig. 5.15f, it was necessary to introduce an additional first harmonic component at a radius of 13 cm with a magnitude of 0.6 Gauss and a phase of 55 °. The initial position of the center, i.e. after leaving the ion source slit is marked with the red circle in Fig. 5.15f. The center coordinate evolution calculated in the SNOP seems to be shifted by 1 − 2 mm to the azimuth 270 °. An important piece of information displayed in the center position graphs in Figures 5.15f and 5.15e is the orbital drift during the last few revolutions before reaching the 515 mm radius. This drift is manifested by a significant shift of the center of the orbits towards the first quadrant of graphs and its cause is the first harmonic perturbation component of the magnetic field which directs the beam in an undesirable direction. Section 3.3 was devoted to the origin of the first harmonic perturbation amplitude and

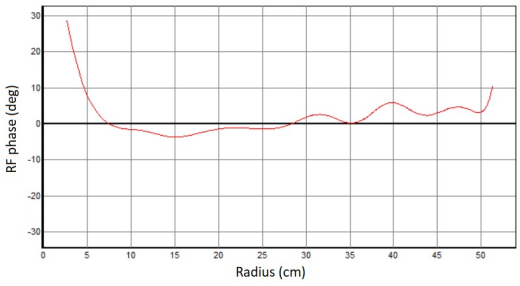

(a) RF phase Durycnm.

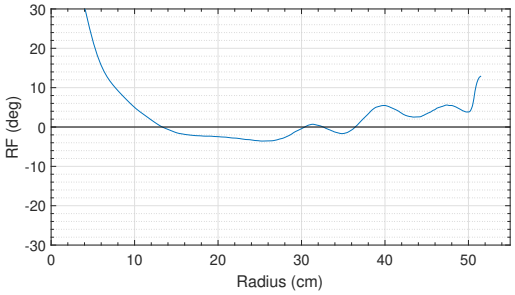

(b) RF phase SNOP.

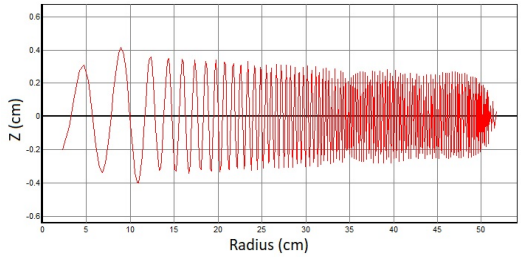

(c) Z coordinate Durycnm.

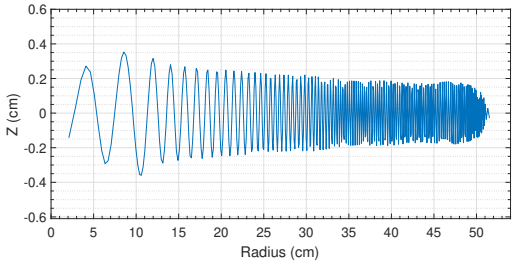

(d) Z coordinate SNOP.

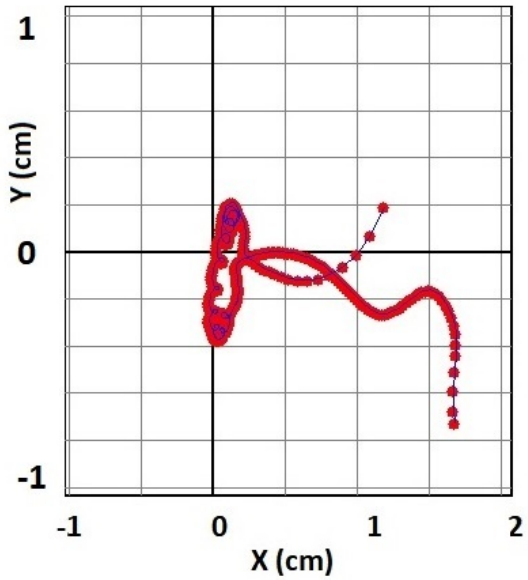

(e) Orbit center positions Durycnm. Acceleration starts in the lower right corner.

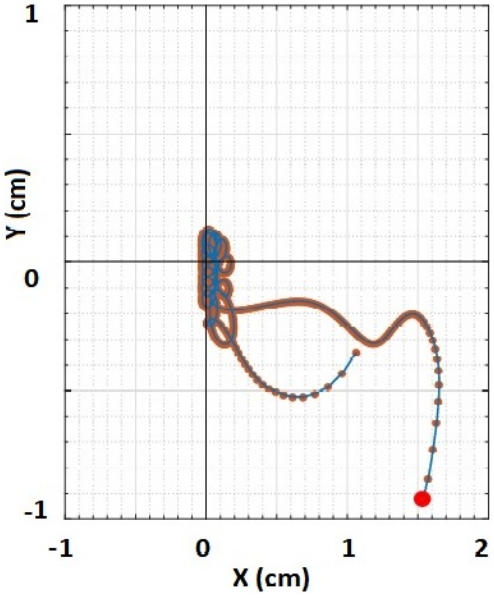

(f) Orbit center positions SNOP. Start position indicated by the red circle.

Figure 5.15: Comparison of calculations done by SNOP and Durycnm for an arbitrarily defined ion. See text for further details.

its limitation.

Based on the above agreements, the two beam acceleration dynamics calculators can be considered very well matched. I leave the minor deviations that are manifested by the necessity of additional centering by the external 0.6 Gauss first harmonic component and a slight change in the acceleration frequency of 3 kHz for later analysis, as the results provided by both programs are in good agreement for the needs of this dissertation.

5.2.2 Single ion extraction

Orbital separation at an extraction radius of 50 cm is approximately 0.6 mm according to 2.28. This value does not provide a good perspective for high extraction efficiency even when using a very thin electrostatic deflector septum. Moreover, in the initial state of the magnetic field, i.e. without limiting or modifying the first harmonic component at higher radii, the beam tends to drift into the I. quadrant as shown in Fig. 5.15e and the beam does not even reach the extraction radius at the azimuth of the first deflector 210°. Due to the fact that the Deflector I is located in the III. quadrant, it is necessary to externally adjust the amplitude and the phase of the first harmonic component such that the drift direction of the beam orbit induces a shift to the III. quadrant. The electromagnetic exciter described in section 5.1.1 is used for this purpose in the current version of the extraction system.

After exciting the electromagnetic exciter with current −250 A and shifting its position to 48 cm, the orbit centers shift to the third quadrant and the orbit separation increases by 1.2 mm to the value of approximately 1.8 mm. The desired movement of the orbit centers is shown in Fig. 5.16, where a comparison of the Durycnm and SNOP outputs is presented. Fig. 5.16b shows the drift of the orbit centers for various currents in the electromagnetic exciter coil. Corresponding orbit separation at azimuth of the first electrostatic deflector calculated by SNOP is shown in Fig. 5.17. It is worth noting that the exciter coil has satisfactory capabilities to split the orbits by a sufficient distance so that a deflector septum can be inserted between them. However, the angle under which the beam drifts away from the center of the cyclotron is determined by the combination of the exciter current and the actual value of the first harmonic perturbation amplitude at the extraction radius, and it is therefore not possible to independently change the size of the orbit separation and the direction of the beam drift.

As the beam is transferred to the extraction radius of 50 cm and coherent oscillations providing the orbits separation are excited by the electromagnetic exciter coil, it is possible to import the Deflector I CAD model and its electrostatic field map into the SNOP simulator. After fine-tuning the exciter current to −242 A, the particle passes the Deflector I for the deflecting voltage −100 kV, which corresponds to a mean electric field along the ion path inside the deflector of approximately −240 kV/cm. At the azimuth of the beam probe No. 3 at azimuth 300°, the ion orbit radius is 575 mm, which is sufficient for further extraction to the extraction point (EP) by the following deflectors. The path of the ion through Deflector I is shown in Fig. 5.19, where it can be seen that the focusing section of the deflector is not fully optimized. Although the ion leaves the first non-focusing section of the deflector roughly midway through the gap, the path at the end of the focusing section almost touches the voltage electrode. The highly unoptimized shape of Deflector I is confirmed in the following section by introducing a bunch of particles and extracting them through this deflector.

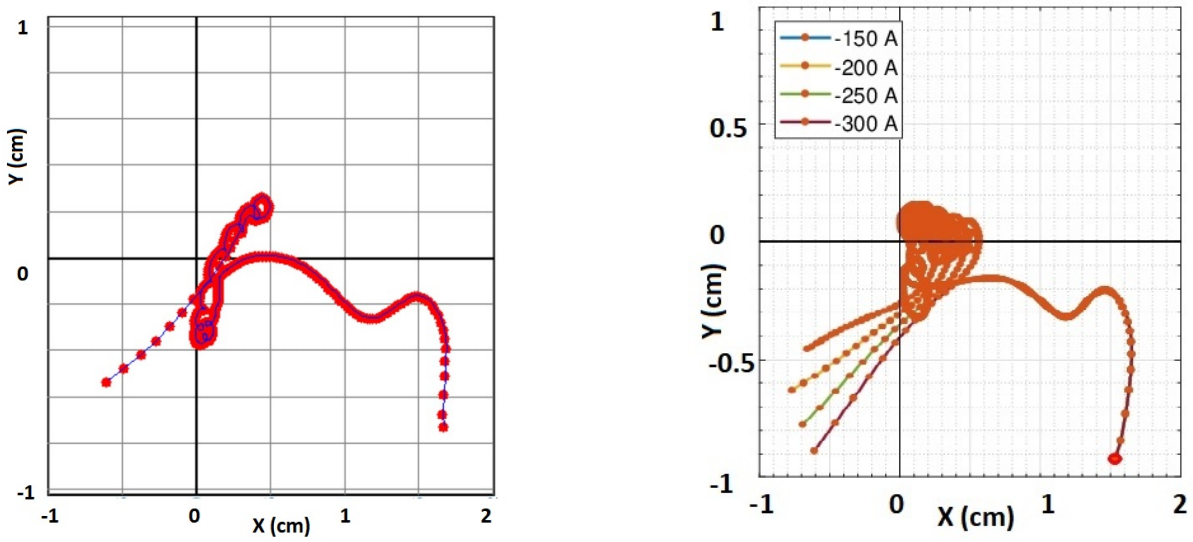

(a) Orbit center positions Durycnm.

(b) Orbit center positions SNOP.

Figure 5.16: Comparison of calculations done by Durycnm for the exciter current −250 A and SNOP calculation for various exciter currents. The acceleration starts in lower right corner. See text for further details.

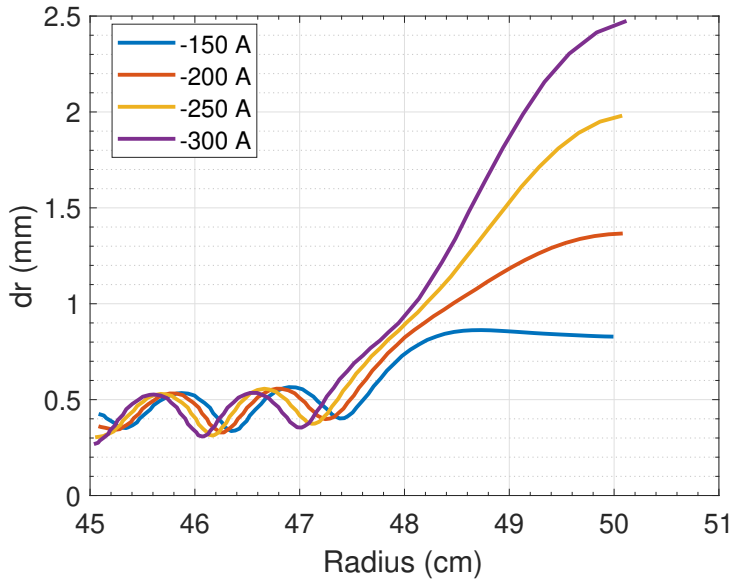

Figure 5.17: Orbit separation at azimuth of the first deflector 210° for various exciter currents.

5.2.3 Bunch extraction

The initial bunch of particles is defined relative to the previously introduced initial ion. The 1×1.75 mm ion source slit region is covered by uniformly distributed ions with parameters listed in Table 5.7. The bunch is defined within the RF phase range of 180° according to the Child-Langmuir law [58].

From the initial 997 ions, 291 ions are lost in the first turn on the geometry of the ion source and the puller. From the remaining 706 ions 685 ions are accelerated to the extrac-

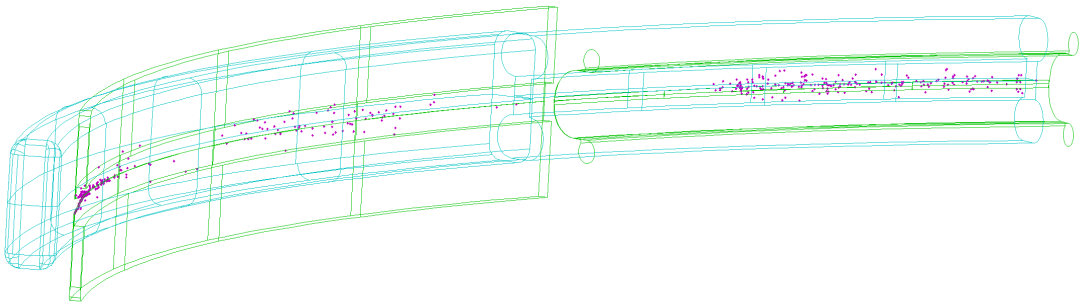

Figure 5.18: Beam losses along Deflector I. Blue structures represent the HV electrodes, the green structures are the septa. The particle losses are indicated as magenta dots. See text for further details.

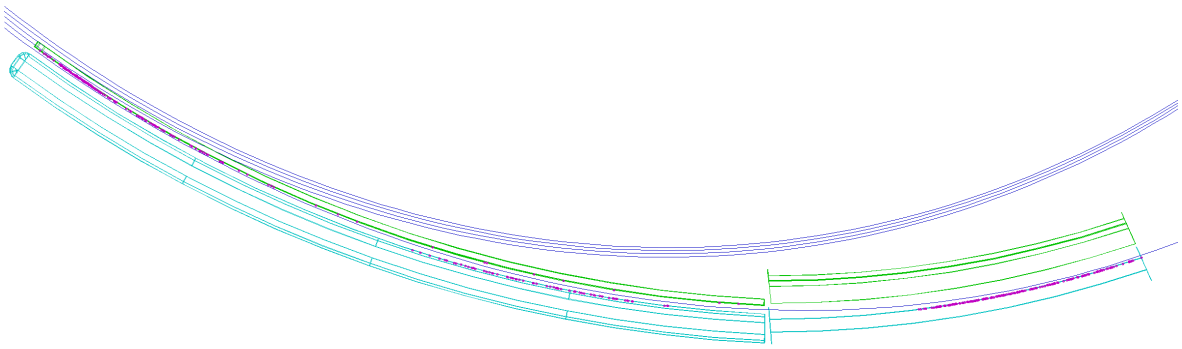

Figure 5.19: Central ion path through Deflector I. Blue structures represent the HV electrodes, the green structures are the septa. The particle losses are indicated as magenta dots. See text for further details.

Table 5.7: Initial particle bunch parameters.

Bunch center radius	28.63 mm
Bunch center azimut	−20.412 °
Bunch center z	0 mm
Radial size	1 mm
Vertical size	3.5 mm
Radial emittance	140 π mm mrad
Vertical emittance	100 π mm mrad
RF phase range	180 °
Number of ions	997

tion radius and the remaining 21 ions are lost on the walls of the acceleration chamber. From the bunch entering the first deflector, i.e. from the 685 ions in the acceleration process 156 ions passed the Deflector I and reached an average radius of 574 mm on beam probe No. 3. The transparency of Deflector I is then 156/706 = 22.1%. Although this value may seem low, in the usual ratios of extraction efficiency on the U-120M cyclotron it is a relatively high value. Proton beam extraction has the lowest efficiency compared to other types of particles and the usual value achieved during experiments is in the region of around 5% in the long term. Due the very high electric field the extraction of protons with energies above ∼25 MeV is not possible at all.

The detailed distribution of losses in the central area and along Deflector I is shown in Table 1. From Fig. 5.18 and 5.19, where the sketch of Deflector I and the distribution of losses on it are shown, it can be seen that the largest part of the beam is lost on the voltage electrode in the focusing section and a significant part of the losses happens also roughly in the middle of the septum of the non-focusing part. In the figures, the voltage electrode has blue color and the septum electrode has green color. Losses occurring at the origin of the deflector in the V-shape region can be considered unavoidable due to the insufficient separation of the orbits. However, losses in the other parts of the deflector can be reduced by appropriate adjustment of the shape of the electrodes and the distance between them.

Table 5.8: Distribution of the losses and properties of the extracted bunch.

	Count	% of total	% of accelerated
Number of ions in total	997	100 %	–
Losses in central region	291	29.2 %	–
Accelerated beam	706	70.8 %	100 %
Losses on chamber walls	21	2.1 %	3 %
Losses on Deflector I:	529	53.1 %	74.9 %
V-shape region	228	22.9 %	32.3 %
Straight section	80	8 %	11.3 %
Focusing section	221	22.2 %	31.3 %
Extracted beam	156	15.6 %	**22.1 %**

5.2.4 Extraction system modification

Based on the performed simulations it seems the shape of Deflector I was optimized for a different settings of the extraction process. It is likely that the shape of Deflector I is based on the beam parameters of the very original regenerative extraction system. The performed beam extraction simulations indicate that for the use with the electromagnetic exciter coil the Deflector I has a smaller bending radius than is necessary. Currently, the bending radius is 627 mm, but according to simulations, more appropriate bending radius would be in the range of 650–680 mm.

The non-optimal shape of the deflector in the actual configuration with electromagnetic exciter and beam losses on the deflector body encourage minor changes to its layout. Preliminary analysis suggests that the size of the gap between the electrodes in the

non-focusing section should be 6–8 mm. When increasing the deflector gap to 8 mm and rotating the focusing section by $-3°$ with respect to the deflecting section, the transparency of the Deflector I increases to 78 %. A simulation for the modification of the old Deflector I described above is given in Sec. 5.3.5.

5.3 New extraction system properties

The demand for redesign of the extraction system is driven mainly by low extraction efficiency and the related high activity of the deflectors after their usage. This applies in particular to Deflector I, on which the vast majority of the extracted beam is lost, as was shown in the paragraph 5.2.3 and which is the most radioactively activated. This deflector suffers from significant susceptibility to high voltage surges and requires the most maintenance among the three deflectors. Upgrade of the Deflector I is therefore highly desirable.

The inability of the Deflector I to maintain the necessary high voltage for a long time is closely related to the extraction radius from which this deflector is able to efficiently extract the beam. As the radius from which the beam is deflected increases, the necessary electric field required for the deflection to a constant final radius decreases. Thus, one way to reduce the required electric field of Deflector I would be to increase the extraction radius. However, this is not possible in the case of Deflector I, because, as mentioned in the previous paragraph, its bending radius is too small.

Another effective way to reduce the required voltage is to increase the angular length of the Deflector I. The electric field would then act along a longer path of the extracted particle and a lower electric field would be needed to deflect the particle to the same radius. An option to achieve this effect is to replace the currently used electromagnetic exciter with a short deflector, which effectively increases the length of Deflector I. This solution is used on the AIC144 cyclotron in Crakow [8, 11], which is very similar in design to the U-120M cyclotron. For this reason, during the shutdown of the accelerator in spring of 2022, we installed a new set of electromagnetic harmonic coils in the accelerator chamber, which have the task of taking over the function of the electromagnetic exciter and thus enabling its replacement by a short deflector.

In the following paragraphs of this chapter, I will present the achieved results of the design of the modified extraction system of the U-120M cyclotron. An overview of the properties of the new harmonic coils and their use to increase the extraction radius will be provided. Furthermore, Deflector 0 will be introduced as a replacement for the electromagnetic exciter. The current Deflector I will be replaced by a new one with a profiled electrode shape for additional beam focusing. Deflectors II and III will be replaced by magnetic channels. Finally, the extraction efficiency of this new system will be assessed.

5.3.1 Extraction radius

The highest demands on the electrical strength of Deflector I are required when accelerating protons at the highest energies, i.e. currently protons with an energy of 37 MeV. Fig. 5.20 shows a comparison of the electric field required to deflect a 37 MeV proton from different extraction radii to a defined radius of 600 mm at an azimuth of 300° for two different azimuthal lengths of the deflection path. The azimuthal length 58° corresponds to the current length of Deflector I, azimuthal length 80° is the sum of the lengths of Deflector I and the new Deflector 0 (22°). For all other available proton acceleration

modes at lower energies and for all other particle modes, the required deflection voltage is lower than shown in the figure. The old extraction system simulation presented in Sec. 5.2.3 reflects the past system and consist of only the electromagnetic exciter coil. The simulation of the modified old extraction system in Sec. 5.3.6 includes the use of the electromagnetic exciter together with the new harmonic coils and the simulation of the new extraction system in Sec. 5.4.1 includes the new harmonic coils only.

According to the simulations, reaching an extraction radius of 530 mm seems impossible. At this radius, there is already a considerable increase in the vertical dimension of the beam due to the occurrence of the parametric $\nu_r - 2\nu_z = 0$ resonance. The furthest attainable radius at which the beam with a vertical dimension smaller than 3 mm can be maintained is most likely a radius of 524 mm.

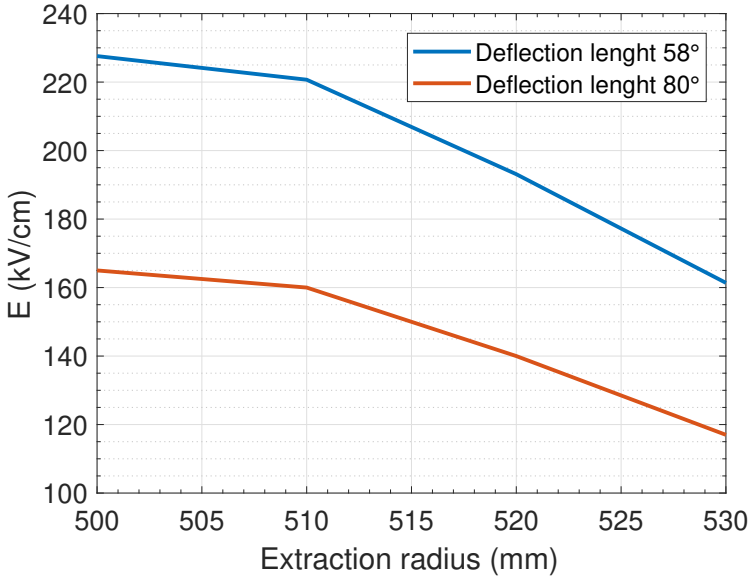

Figure 5.20: Electric field necessary to extract proton beam to the radius 600 mm at 300°. See text for further details.

5.3.2 Harmonic coils

The new harmonic coils were briefly introduced in section 3.2.4, where it was said that the cyclotron has two sets of double pair harmonic coils installed. Originally, the U-120M cyclotron was equipped with only one pair of internal harmonic coils at a radius of 14 cm. However, these were constructed with only one coil turn and their beam centering effect was insufficient. A new set of harmonic coils with four coil turns was installed in 1984 at two selected radii. The first pair of enhanced harmonic coils was re-installed at 14 cm radius and their performance is excellent. The second pair of coils was installed at a radius of 42 cm and was intended to serve as an additional fine-tuning of the beam centering. The effect of the outer coils begins to show up at a radius of 30 cm and ends at 50 cm with a maximum of the first harmonic amplitude at 42 cm as is can be seen in Fig. 3.13. However, the external harmonic coils at the radius 42 cm did not show any significant improvement in beam parameters. If the first harmonic component of the field should be useful for the beam extraction, its maximum should be directly at or very close to the region where $\nu_r = 1$, usually at the extraction radius. For this reason, the effect of the

external harmonic coils to ensure effective beam extraction was minimal.

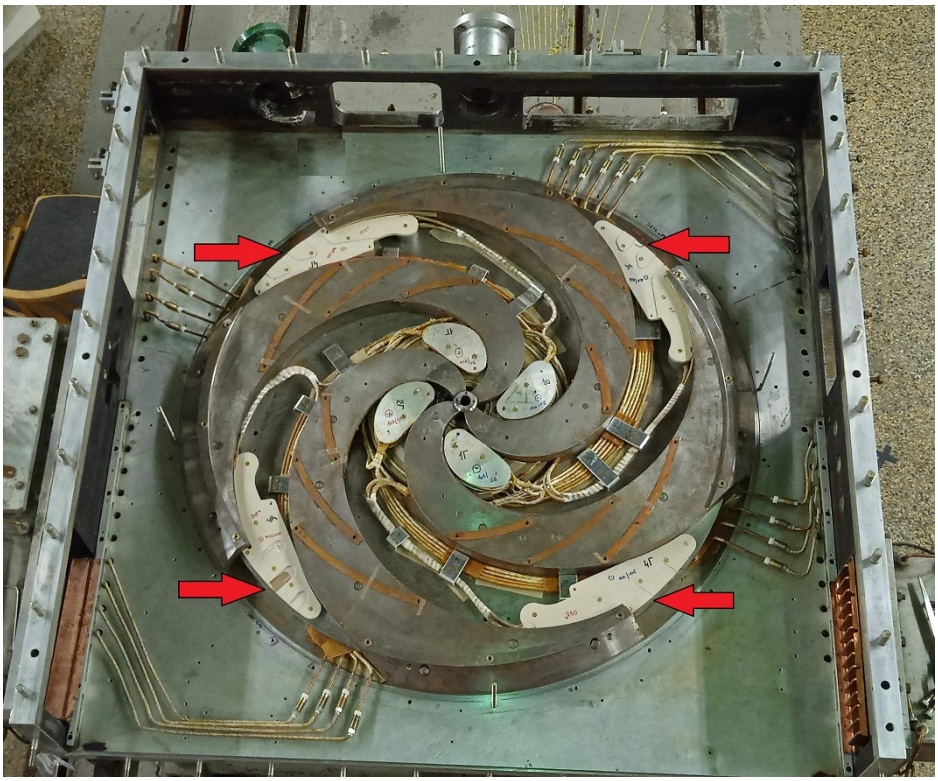

Figure 5.21: New harmonic coils installed between the cyclotron sectors. Red arrows indicate the position of the coils.

As an integral part of the new extraction system, I designed a set of new harmonic coils acting at a higher extraction radius. The new coils are able to compensate the internal first harmonic perturbation of the cyclotron magnetic field at final radii such that a higher beam acceleration radius can be achieved. Therefore the maximum energy that can be achieved at the accelerator can be increased by 5–8 %. In particular, however, these new coils make it possible to achieve a sufficient separation of the orbits at the extraction radius. The performed simulations indicate that the new harmonic coils enable very efficient extraction while maintaining the radial dimension of the beam at the entrance of Deflector 0 within approximately 2–2.5 mm.

The goal of the design was to create such a configuration of the coils that will allow us to compensate for the error in the magnetic field of the cyclotron and that would help to guide the center of the beam orbit to an azimuth of approximately 270° with a sufficient separation at the azimuth of Deflector 0 at 182°. The simulations showed the need for coils capable of exciting the first harmonic component of the magnetic field with a size of at least 30 Gauss. The new harmonic coils installed at the extraction radius are shown in Fig. 5.21, where the position of the coils is marked by the red arrows.

The design of the new harmonic coils proved to be a difficult task due to the mechanical arrangement of the cyclotron magnetic system. As it is described in Sec. 3.2.3, the magnetic structure consists of the spiral sectors and a set of 18 concentric trim coils. The first five trim coils are built into the sectors on the radii up to 180 mm and the rest are placed at the copper trim coils' holder, see Fig. 5.22, the spiral sectors are shown in Fig. 5.21. The new harmonic coils were installed at the only possible place in the valley space, i.e. between the magnet spiral sectors and below the trim coils' holder. At the radii where

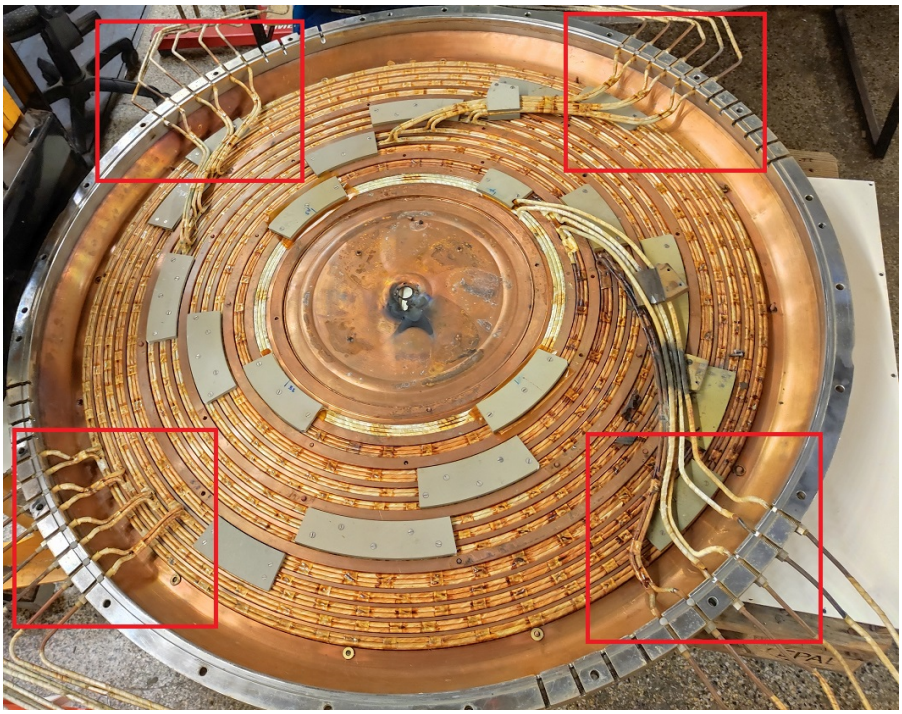

Figure 5.22: Bottom holder of the trim coils No. 5 – 18. The red squares mark the location of the new harmonic coils. The dark spots are traces of electrical breakdown of the trim coil No.6 insulation. Details are given in the text.

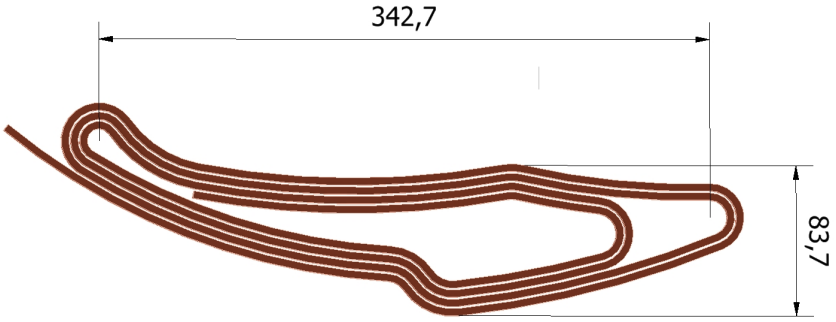

(a) New harmonic coil 4×4 mm.

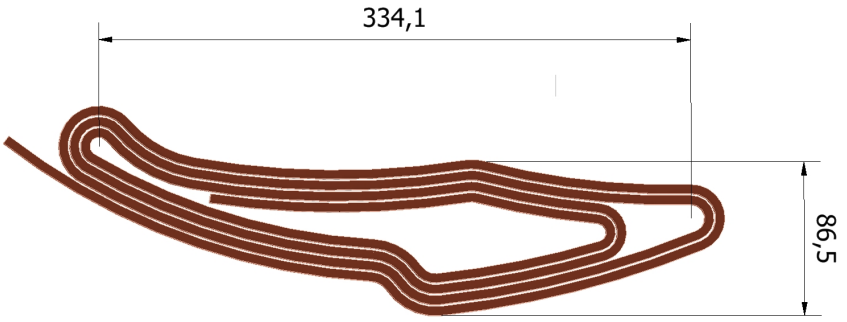

(b) New harmonic coil 5×5 mm.

Figure 5.23: Overall dimensions of the new harmonic coils.

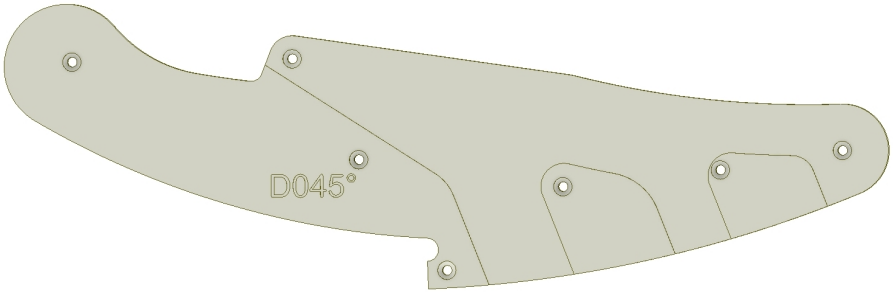

(a) Support for the HC coil at azimuth 45°.

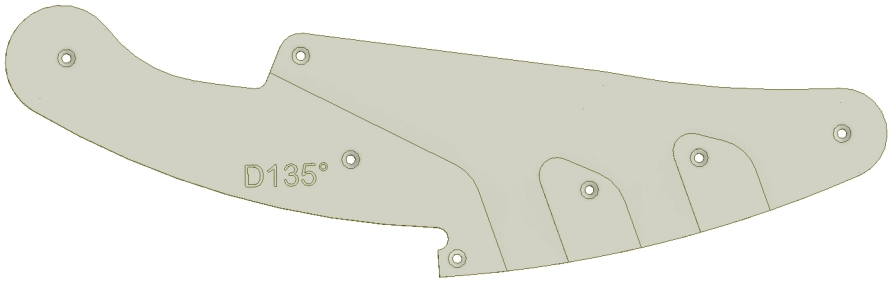

(b) Support for the HC coil at azimuth 135°.

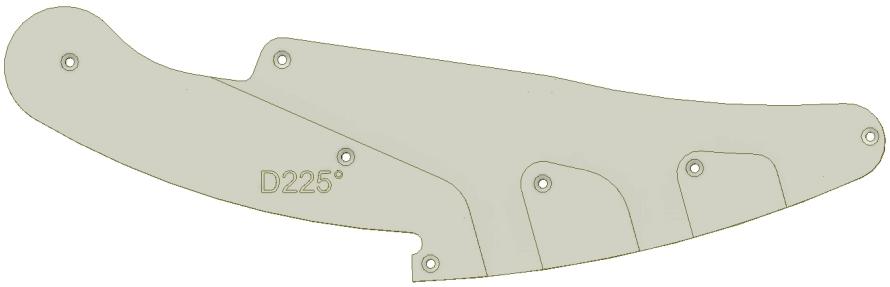

(c) Support for the HC coil at azimuth 225°.

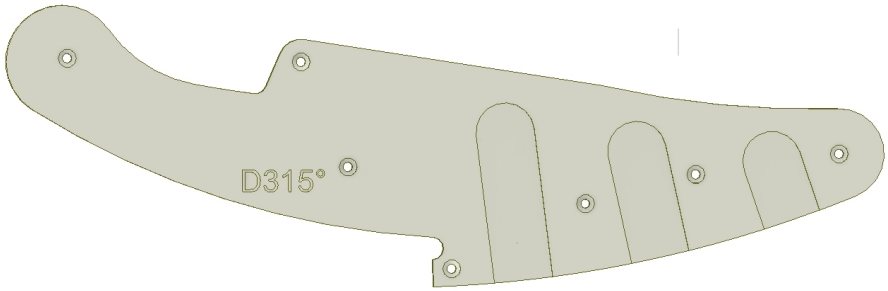

(d) Support for the HC coil at azimuth 315°.

Figure 5.24: Design of the holders for individual harmonic coils. Details are given in the text.

the new coils were installed, the sectors are connected by an iron sector liners providing magnetic field shaping at final radii.

Figure 5.25: Aluminum mold for forming coils.

The space between sector liners and the trim coils' holder, where the new harmonic coils were installed, serves for current and cooling water inlets for the trim coils. The sector liners limit the free vertical gap between the trim coil inlets and cannot be modified. An intervention into the coil inlets could lead to a micro rupture of the heavily age-hardened copper tubes which could potentially cause water leakage problems in future. From this reason only a non-invasive solution into the current magnetic system was possible.

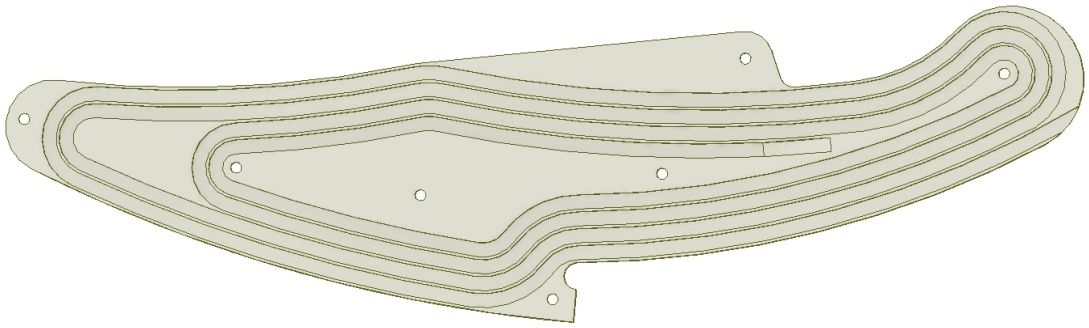

Figure 5.26: Harmonic coil support at azimuth 225° with 1 mm thick wall between individual turns.

Two of the sector liners limit the free vertical gap between the trim coil inlets to 8 mm, third liner has free gap 6 mm and the fourth one has only 5 mm of the free space. The harmonic coils' design resulted into two slightly different coil pairs to fit into the free gap. The coils are fabricated from hollow rectangular copper tubes with a cross-section 4×4 mm and 5×5 mm. The remaining 1 mm free space is occupied by an electrical insulating support housing the coils. The situation is schematically drawn in Fig. 5.27 where the trim coils inlets are not shown. The design of both coils with overall dimensions can be seen in Fig. 5.23.

The limited vertical clearances above the liners resulted in the need for individual design of electrical isolation supports for each individual coil located at azimuths of 45°, 135°, 225° and 315°. As can be seen in Fig. 5.22, for each of these azimuths the trim coil inlets have different arrangements. In order that the harmonic coil supports fit into the space above the liners, it was necessary to make cutouts in each of them copying the trim

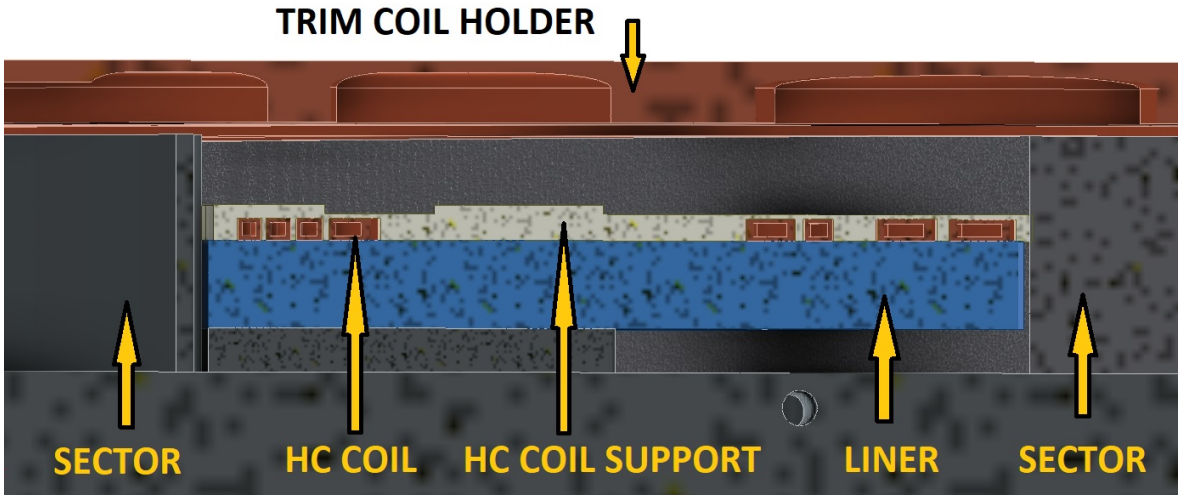

Figure 5.27: Schematic plot of the installation gap for harmonic coils. The sector liner has blue color.

coil inlets at a specific azimuth. The resulting shapes of the harmonic coil supports are presented in Fig. 5.24. Fig. 5.25 shows the mold used to shape each 4×4 mm coil, the form for a 5×5 mm coil is similar. After forming in the mold, the coil was pressed into the insulating support and screwed to the liner. The insulation gap between individual turns of the coil is 1 mm and it is defined by the thickness of the wall created in the insulation support as shown in Fig. 5.26. Due an exceptional radiation resistance, excellent vacuum behavior and good mechanical and electrical properties, the coils insulation housing is made from high-performance plastic PEEK (polyether-ether-ketone) [68].

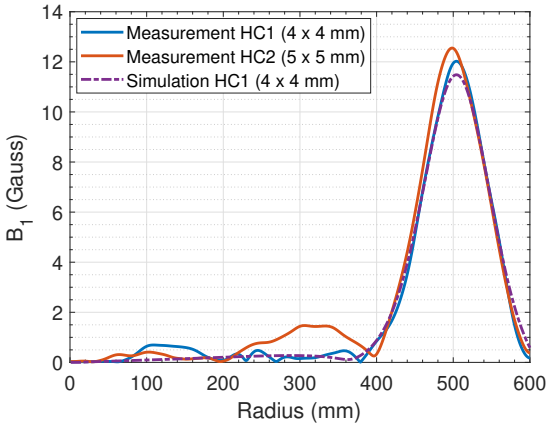

(a) Overall influence over radius.

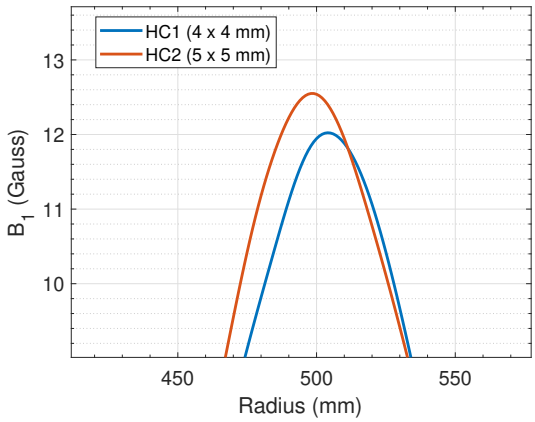

(b) Detail of the HC coils' peak tip.

Figure 5.28: Comparison of the measured and simulated first harmonic component of the new harmonic coils for current 200 A. See text for further details.

Due the usage of different tubes size the difference in the radial length of the coils is approximately 3 mm and position of the coils radial center lines differs by 4 mm. The CST [67] simulation showed a difference of 5 mm in the radial position of the maximum contribution and this result was confirmed by the magnetic measurement. Comparison of the measured contribution of the first harmonic magnetic field component of HC1

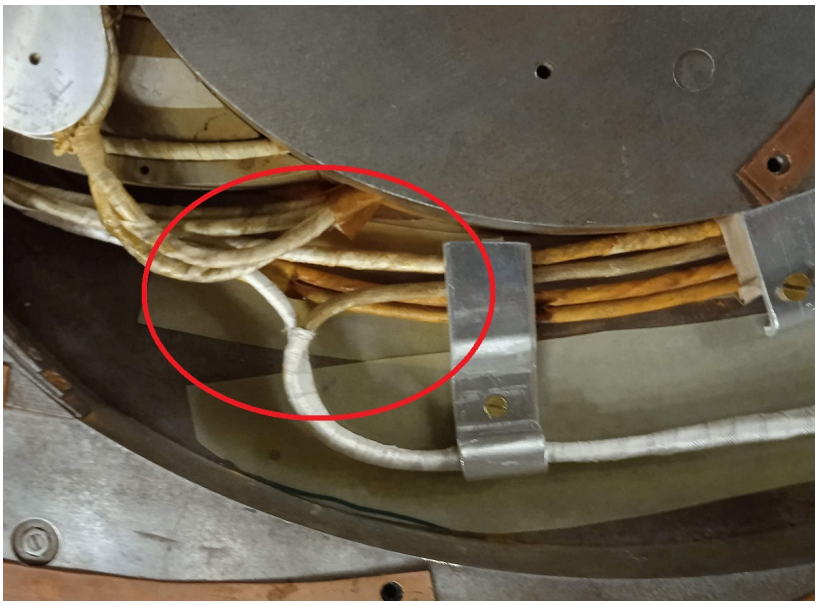

Figure 5.29: Detailed view of the imperfect connection of the HC2 coil. The false coil is inside the red ellipse. See text for further details.

(4×4 mm) and HC2 (5×5 mm) coils for 200 A current is presented in Fig. 5.28. Figure 5.28a also includes contribution of HC1 coil as obtained from the CST simulation. The measured data revealed also a presence of a weak parasitic component that spans over radii 200—400 mm. This is most likely caused by the imperfect connection of the HC2 coil, which is shown in Fig. 5.29. The insufficient overlap of the supply wires marked by the red ellipse has caused the magnetic field of the flowing currents not to be perfectly compensated for each other, which yields to the formation of a false coil creating a parasitic contribution at lower radii approximately 14.5 % of the HC2 coil contribution. From the performed simulations of the effect of the HC2 false coil on the acceleration process and from the experiments performed during the tests of the new harmonic coils' effect on the beam, it appears that this parasitic contribution is not destructive to the beam.

Fig. 5.28b shows a detail of the peak tip at a radius of approximately 500 mm. A small variation in the peak amplitude is due to the different geometry of the coils. In this figure, there is also visible a deviation of 5 mm in the radial position of the maxima of the two coils. The magnetic field map of the new harmonic coils is shown if Fig. 3.12.

5.3.3 Harmonic coils effect on the beam

From now on, the 4×4 mm coils at azimuths 135° and 315° will be called HC1 and 5×5 mm coils at azimuths 45° and 225° will be called HC2.

If internal harmonic coils are mentioned in the text, it will be explicitly stated that they are the coils at the inner radius such that there is no confusion with the new harmonic coils installed in 2022, i.e. with the HC1 and HC2 coils.

5.3.4 Effect on negative beams

First, I will verify the effect of the new harmonic coils on the magnetic field map 36.4A for negative hydrogen of final energy 36.4 MeV. The magnetic map of this mode was measured during the verification magnetic measurements at the end of the cyclotron repair in the

fall of 2022. The analysis will be performed in the Durycnm program, in which the magnetic map of one of the new coils is imported. In this case, however, it is necessary to mention the limitations regarding the realism of the performed simulation. Due to its internal layout, it is not possible to insert both complete maps of the magnetic fields of the external harmonic coils HC1 and HC2 into the Durycnm program. The Durycnm program accepts only one partial magnetic map for one harmonic coil and internally creates a second map by rotating it by 90 °. This algorithm is based on the assumption that the two coils are identical, which is not the case. Moreover, for successful import, it is necessary to limit the map to the area of radii 280 – 600 mm and azimuthal range 138 – 225 °, where the original external harmonic coils were located. For this reason, the imported map of the new harmonic coils is incomplete and does not take into account the small deviations between the HC1 and HC2 coils.

The import of the HC2 coil magnetic map was thus performed by rotating the map by 30° and limiting the input data to radii accepted by the Durycnm program. For this reason, the ratios of currents in the HC1 and HC2 coils will not exactly correspond to the currents that must be set on the real coils to achieve the same effect. From the simulations performed on the positive beams in the SNOP program, the difference in the effect of the coils HC1 and HC2 on the beam centering emerges. The SNOP program contains complete magnetic maps of both coils and there is an assumption that it fairly faithfully simulates the real acceleration process.

Negative hydrogen mode 36.4 MeV

Without using the new harmonic coils, the beam is driven off-center due the first harmonic magnetic field perturbation and near radius 505 mm is completely lost vertically as it is shown in Fig. 5.30a. Before the cyclotron magnetic field repair in 2022, the final radius was even lower, at approximately 495 mm. By appropriately setting the currents, the negative influence of the first harmonic perturbation at the highest radii can be suppressed and the beam can thus be accelerated to a significantly larger radius. The optimum setting of the new harmonic coils was found manually. The best performance was achieved for -80 A for HC1 and +20 A for HC2. The HC1 and HC2 ensure that the beam can be accelerated without vertical blow up up to a radius of 520 mm with a final energy of 39.6 MeV. This is presented in Fig. 5.30b, where the simulation is done for a single ion with the RF phase 0°. The dependence of the beam energy on the extraction radius as calculated in the Durycnm and SNOP simulators is shown in Fig. 5.31. The difference in the harmonic coils' currents that is considered in the simulators reflects the incomplete magnetic field coils' maps in Durycnm. The settings for the coils in SNOP are for the HC1 and HC2 coil −90 A and 70 A, respectively.

Extraction of the beam into the negative beamline is possible with the current configuration of the stripper up to a radius of approximately 510 mm, which corresponds to a mean proton beam energy of 38.6 MeV. Graphical representation of the extraction process is shown in Fig. 5.32. The distance in which the beam passes from the beamline wall in the area of the bending dipole magnet in Fig. 5.32b is approximately 6 mm. The simulator Durycnm predicts that a beam with this energy can be extracted without any necessary modification of any of the cyclotron components. Basic properties of the extracted beam and parameters of the extraction process for the Durycnm simulator are given in Table 5.9.

For beam extraction from a radius of 520 mm, it will probably be necessary to adjust the stripper foil holder, or to slightly increase the range of motion of the arm on which

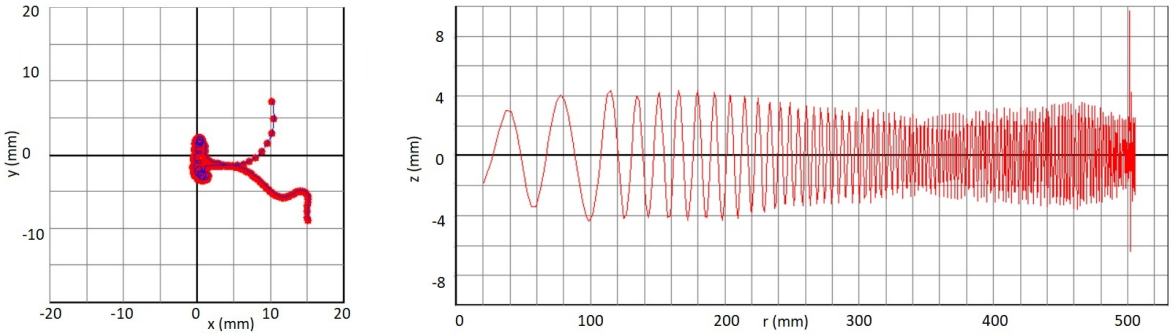

(a) Beam centering (left) and z-coordinate evolution (right) for HC1 = HC2 = 0 A.

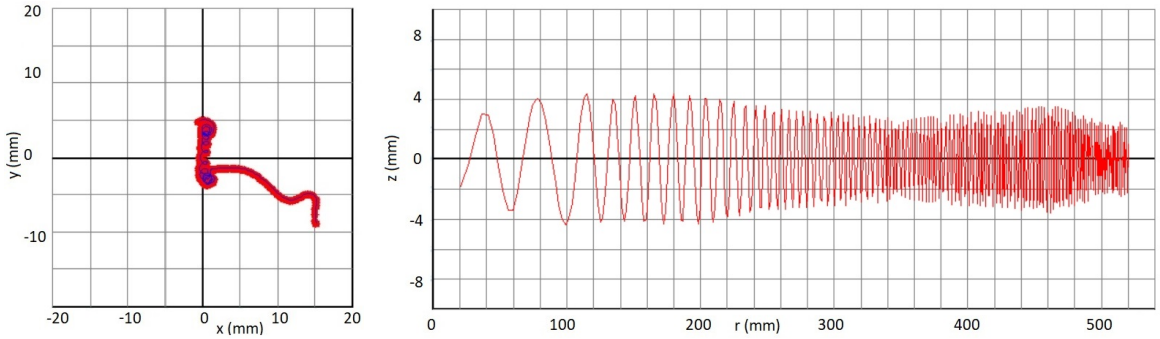

(b) Beam centering (left) and z-coordinate evolution (right) for HC1 = −80A, HC2 = +20A.

Figure 5.30: Comparison of single ion acceleration for the negative hydrogen mode 36.4A. It the centers plot on the left the acceleration starts at the right bottom corner. See text for further details.

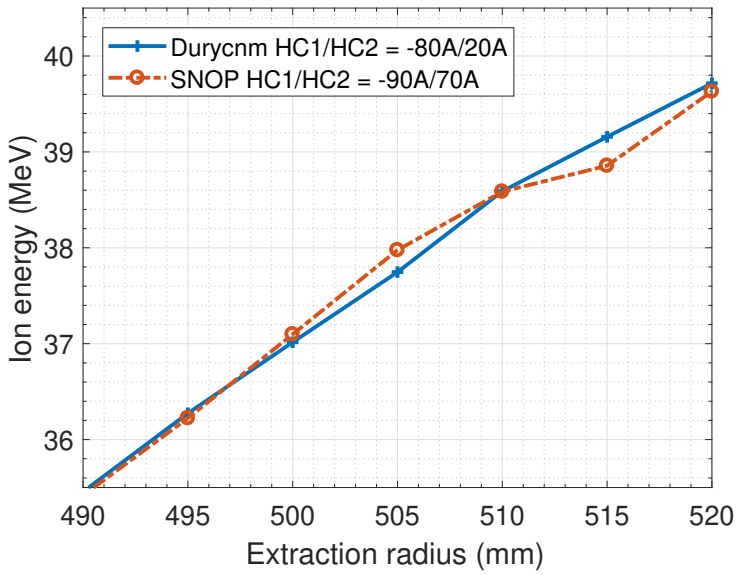

Figure 5.31: Ion energy as a function of the extraction radius for the negative 36.4A hydrogen mode. Comparison of predictions by SNOP and Durycnm.

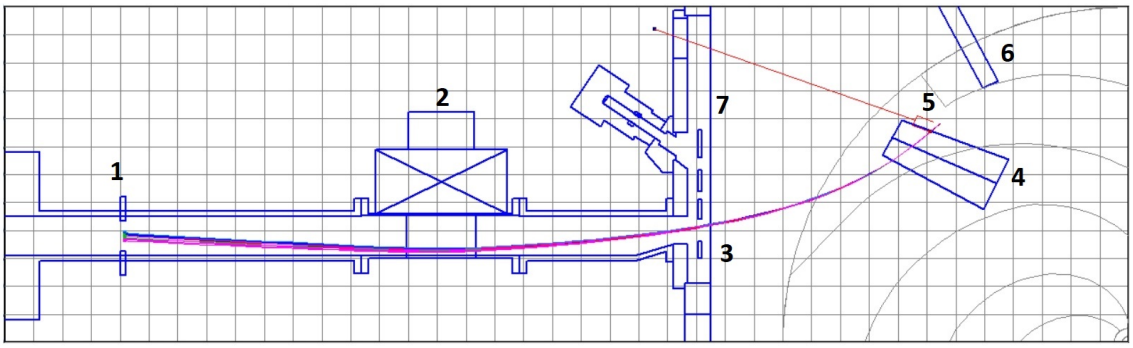

(a) 38.6 MeV proton beam passage through negative beamline.

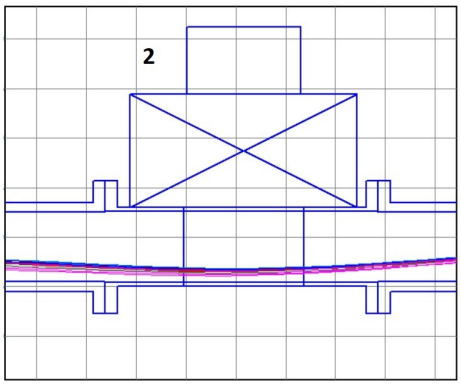

(b) Detail of the beam position in the beam-line in the dipole magnet region.

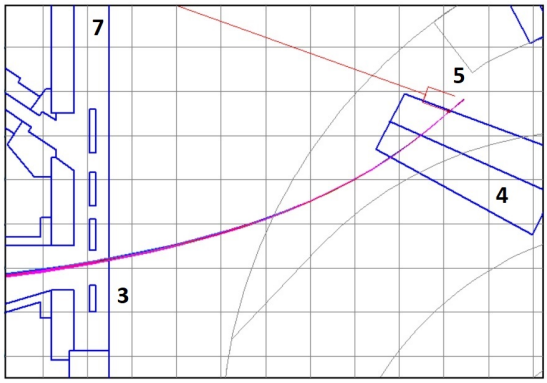

(c) Detail of the stripper foil position just at the limit of the allowed stripper positions.

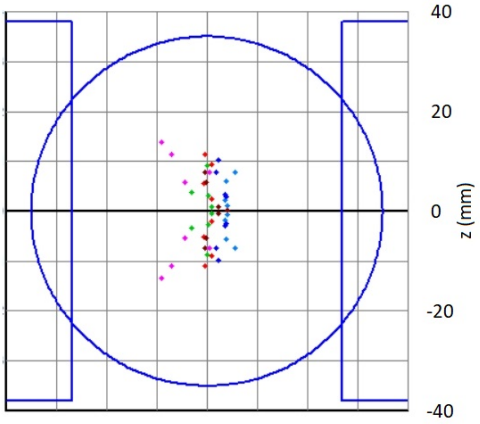

(d) Position of the beam inside the beamline collimator (pos. 1).

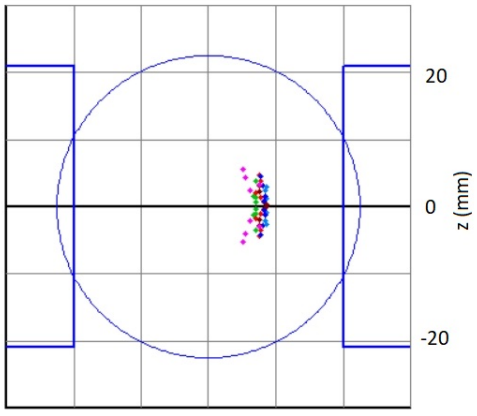

(e) Position of the beam inside the chamber collimator (pos. 3).

Figure 5.32: Graphical representation of the extraction process for 38.6 MeV negative hydrogen accelerated in the 36.4A mode usin new harmonic coils. 1 – beam-line collimator, 2 – dipole magnet, 3 – accelerating chamber collimator, 4 – allowed stripper position, 5 – position of charge stripping, 6 – beam probe No.2, 7 – accelerating chamber wall. See text for further details. Drawings were created using Durycnm [16].

Table 5.9: Settings for simulation of the 38.6 MeV protons extraction in the 36.4A mode.

Settings for Durycnm version 18	
Regime	HM-36-4A-rijen-corr
Acceleration frequency	25.812 MHz
Dee voltage	34.0 kV
Inner harmonic coils current	+52 A / -85 A
Inner harmonic coils current	−80 A / +20 A
RF phase range	-30 ° to +50 °
Radial ion source position shift	−0.8 mm
Final radius / azimuth	510 mm / 130 °
Stripper foil radius / azimuth	510.2 mm / 132.4 °
Bending magnet current	+80 A
Extracted beam properties	
Beam extraction efficiency	100 %
Mean energy	38.586 MeV
FWHM energy dispersion	270 keV (0.7 %)
Full radial beam size	14.6 mm
Full vertical beam size	27.1 mm
Horizontal RMS emittance	8.34 π mm mrad
Vertical RMS emittance	10.3 π mm mrad

the stripper foil is attached. Both of the options are technically feasible. If in the future it would be possible to restore the full frequency range of the RF resonance system and return the ability to operate the RF system at a frequency of 26.9 MHz, it should be possible to extract protons with an energy of more than 42.5 MeV from the 39.8A mode for negative hydrogen in a similar way.

The ability of the U-120M cyclotron to accelerate beams to 52 cm was experimentally verified in February 2022. In March 2022 a proton beam with energy 38.2 MeV was extracted to the negative-mode beamline using the above mentioned HC1/HC2 settings in the 36.4A mode. The energy value was calculated from the extraction radius and position of the beam center. The energy measurement of the extracted beam using the copper foil activation was not carried out at the time of writing this dissertation.

5.3.5 Effect on positive beams

Although the new harmonic coils seem very promising for operation on negative ions, their primary purpose is to enable efficient extraction of positive beams. Here, their role is not to increase the maximum achievable energy, but to excite coherent oscillations of the accelerated beam at the extraction radius and fine-tune the angle of entry of the beam into the deflector. To fulfill this purpose, it is necessary to excite the coils with significantly higher currents than in the previous case. In the acceleration region where ν_r is close to one, the azimuth under which the centers of the orbits move away from the center of the cyclotron can be chosen by the ratio of currents in the individual coils.

Fine-tuning of the harmonic coils' currents was done manually throughout the simulation process, optimizing the orbit separation at the extraction radius and the required voltage on the deflectors.

5.3.6 Modification of the old extraction system

The positive effect of the new harmonic coils can also be used in the existing extraction system by simultaneously using the influence of the electromagnetic exciter and the new harmonic coils. After the modification of the old Deflector I mentioned in Sec. 5.2.4, it is possible to extract a proton beam in the P36.7A mode with a total efficiency of approximately 67 %.

However, for the current extraction system consisting of a modified Deflector I with a gap of 8 mm and a focusing section rotated by -3 ° an unrealistically high voltage is required on the deflector. The necessary electric field is −227 kV/cm, corresponding to −182 kV, see Tab. 5.10, and greatly exceeds the limits specified in Fig. 5.36. The performed simulations are thus only illustrative and their importance lies in verifying the functionality of the adjustments made on the Deflector I, which can be used for proton modes at lower energies or other particle modes, where the required voltage does not exceed the specified limits.

Orbit separation at azimuth 210° and the beam center behavior is presented in Fig.5.33, where is shown a comparison for a case with the electromagnetic exciter used together with the new harmonic coils and for a case with the electromagnetic exciter only. The case with the harmonic coils currents HC1/HC2 = 400/−600 A manifest slightly smaller separation at the Deflector I entry, but the whole orbit at the extraction radius 514 mm is shifted towards azimuth 270° and allows to decrease the necessary Deflector I voltage. The phase diagrams in Fig. 5.34 show deformation of the phase space properties of the beam during the passage through the deflection system due to the inhomogeneous electric field gradients in the actual deflection system. The ellipses in the individual phase space plots are fitted to the plots and the ellipses axis are used to calculate the emittance values. Beam properties at the entrance azimuths of the individual deflectors and their transparencies are listed in Tab. 5.11. As the currents of the electromagnetic exciter coil and the harmonic coils are regulated down, the energy at the extraction radius rises, but the orbit separation at the extraction radius decreases and a drop in the extraction efficiency occurs. By changing the currents in the individual coils, it is possible to choose between higher output energy or higher extraction efficiency.

Table 5.10: Setting of the individual extraction elements.

	Def. I	Def. II	Def. III	HC1/HC2	E.Exciter
Deflector voltage	−182 kV	−70 kV	−90 kV		
Coil current				400 / −600 A	280 A

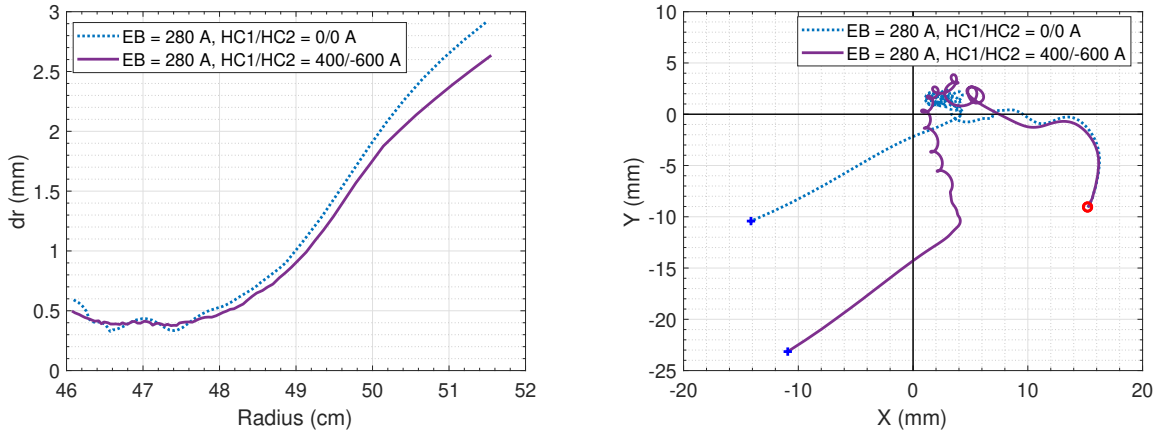

(a) Orbit separation at azimuth 210°.

(b) Orbit center positions.

Figure 5.33: Comparison of the orbit separation and the beam centering for the modified old Deflector I with and without the new harmonic coils. The electromagnetic exciter current is denoted as EB. The red circles indicate particle start position, the blue crosses indicate the last orbit.

Table 5.11: Calculated beam properties at azimuths corresponding to entrance of the individual deflectors for P36.7A proton mode with the modified Deflector I.

Parameter	Def. I	Def. II	Def. III	EP
	214°	270°	300°	346°
Mean Radius (mm)	515.9	567.8	597.5	706.8
Mean Pr (mrad)	21.4	103	96.8	350.4
mean Pz (mrad)	0	0	0	0
$\epsilon_{R,Z}$ (π mm mrad)	2.4	9.4	8.8	10.7
$\epsilon_{R,Pr}$ (π mm mrad)	6.9	14.4	12.2	13
$\epsilon_{Z,Pz}$ (π mm mrad)	7.9	4.1	5.4	9.8
Full radial size (mm)	2.4	10.3	9.6	8.7
Full vertical size (mm)	8.4	7.8	9.5	13.2
Mean Energy		35.8 MeV		
$2\sigma_E$		0.2 MeV		
Deflector transparency	78 %	95 %	92 %	–
Overall extraction efficiency		**67 %**		

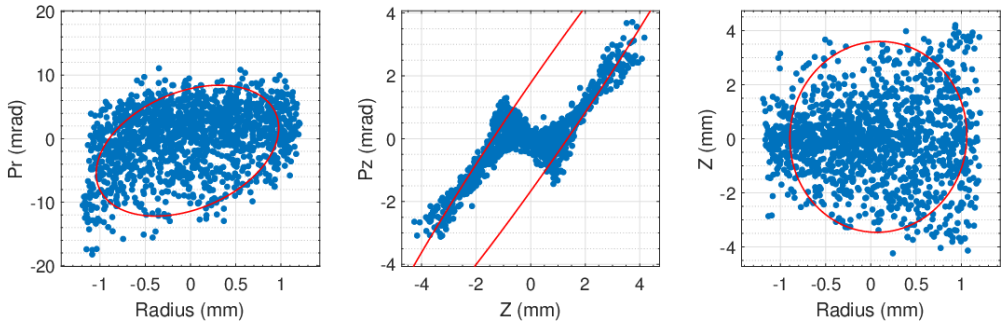

(a) Beginning of the Deflector I – azimuth 214°.

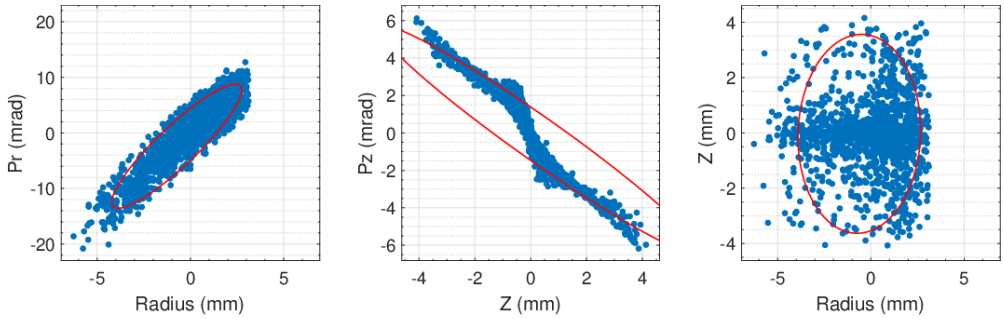

(b) Center of the Deflector I – azimuth 250°.

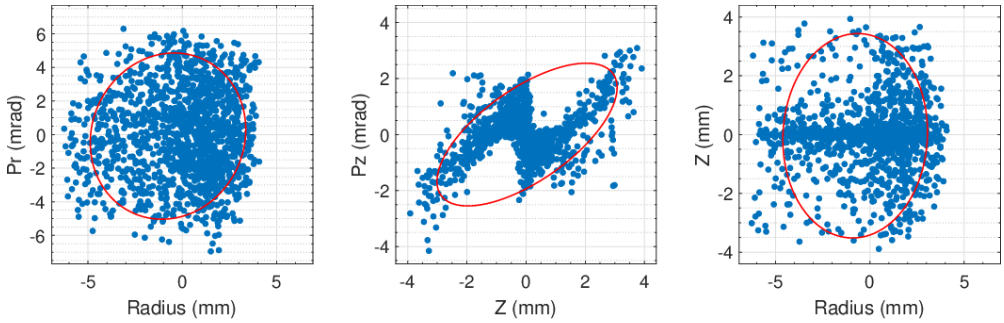

(c) Between the Deflector I and the Deflector II – azimuth 270°.

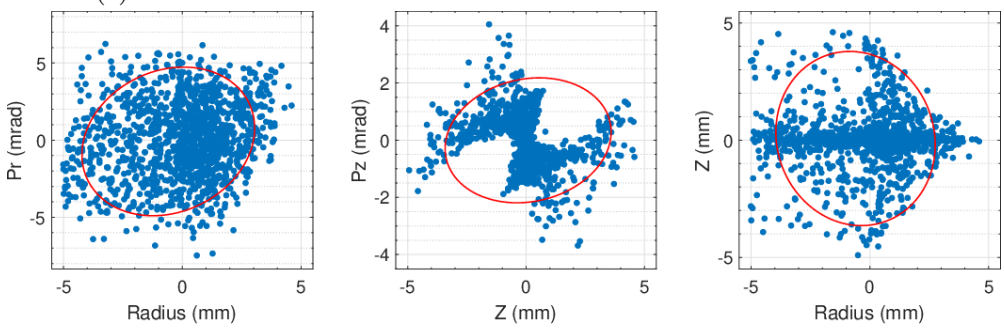

(d) Between the Deflector II and the Deflector III – azimuth 300°.

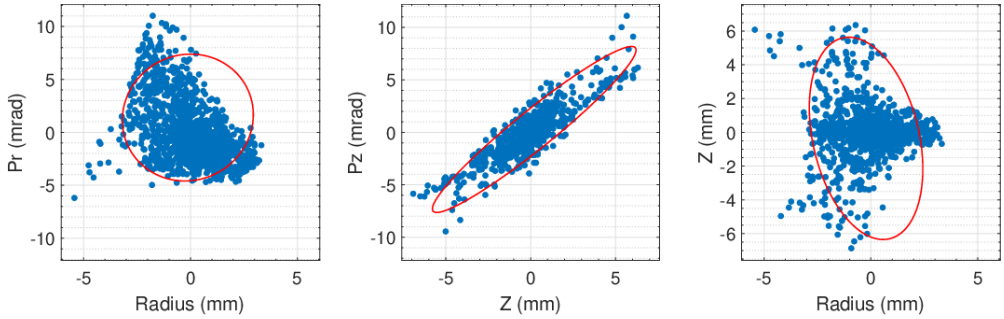

(e) Beam at the extraction point – azimuth 346°.

Figure 5.34: Beam properties of the old extraction system with the modified Deflector I for proton mode P36.7A. The ellipses in the individual plots are used for the emittance calculation.

5.4 Design of the new extraction system

When designing a new extraction system, it is necessary to start from the assumption that this system will serve for extraction of all types of particles available at the U-120M cyclotron and for the widest possible range of their energies. In experiments with positive particles, there is usually the highest demand for beams of the highest energies, and the highest demands on the extraction system itself are placed during the extraction of protons. For this reason, the design of the new extraction system for the U-120M cyclotron will be optimized for a proton mode of the highest energy 36.7 MeV currently achievable on the U-120M cyclotron, i.e. the P36.7A mode. As mentioned, extraction in this mode is not possible with the current extraction system due to the need for too high a voltage on the first deflector. The proposal will therefore be made with regard to achieving realistic parameters of the extraction elements. All other lower energy proton modes as well as all other particle modes will need lower deflector voltages for their extraction.

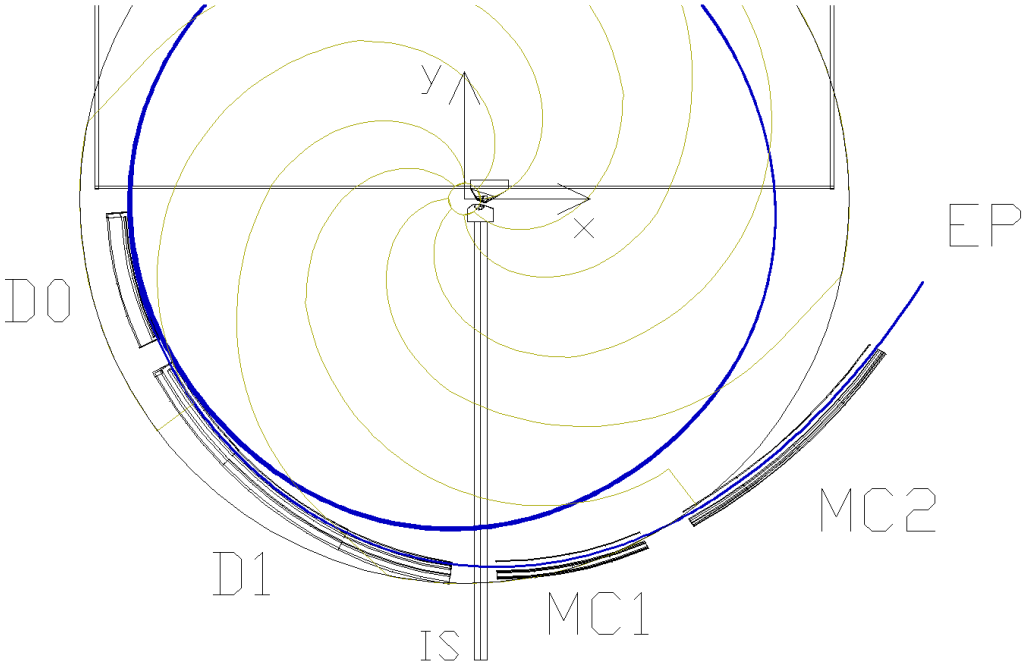

Figure 5.35: Layout of the new extraction system. D0, D1 – electrostatic deflectors, MC1, MC2 – magnetic channels, EP – extraction point. Details are given in the text.

Based on the ability of the new harmonic coils to effectively manipulate the beam at the end of the acceleration, the highest possible extraction radius can be chosen. As it was shown in Section 5.3.1, as the extraction radius increases, the required extraction voltage decreases. However, the choice of a too high radius is not possible due to the passage of the resonance $\nu_r - 2\nu_z = 0$, where the vertical dimension of the beam rapidly grows and limits the maximum possible extraction radius to 524 mm. At this radius and azimuth 182°, a comparison of the effect of the new harmonic coils on the separation of orbits will be made and a new Deflector 0 will be inserted and analyzed. Behind this deflector, a new Deflector I with focusing properties will be inserted, with the help of which the beam will be guided to a radius of 600 mm at an azimuth of 300°. Magnetic channels I and II

will be constructed for this partially extracted beam, which will additionally focus and extract it to the extraction point at the beamline entrance. It can be expected that the system created in this way, optimized for the extraction of protons of the highest energies, will also work well for other particles. Layout of the new extraction system is shown in Fig. 5.35 where the blue line represents several last turns of the deflected particle. The design of the extraction system is not yet fully completed and the presented results are the currently achieved state, which will be optimized during further development.

5.4.1 New electrostatic deflectors

Based on the experience of other cyclotron laboratories [33, 65] with long-term stable operation of high voltage electrostatic deflectors, prerequisites for the successful design of new deflectors can be summarized as follows. The value of the product of the voltage and the electric field in the deflector, the so-called VE value $VE = U \times E$ (kV×kV/cm), should not exceed the value of 1.5×10^4 kV^2/cm. The voltage of the deflector and the magnitude of its electric field should lie below the experimentally determined curves marked in Fig. 5.36. In this figure, the red crosses indicate the design values for the Deflector 0 with the gap size of 4 mm and for the Deflector I with the gap size of 6 mm.

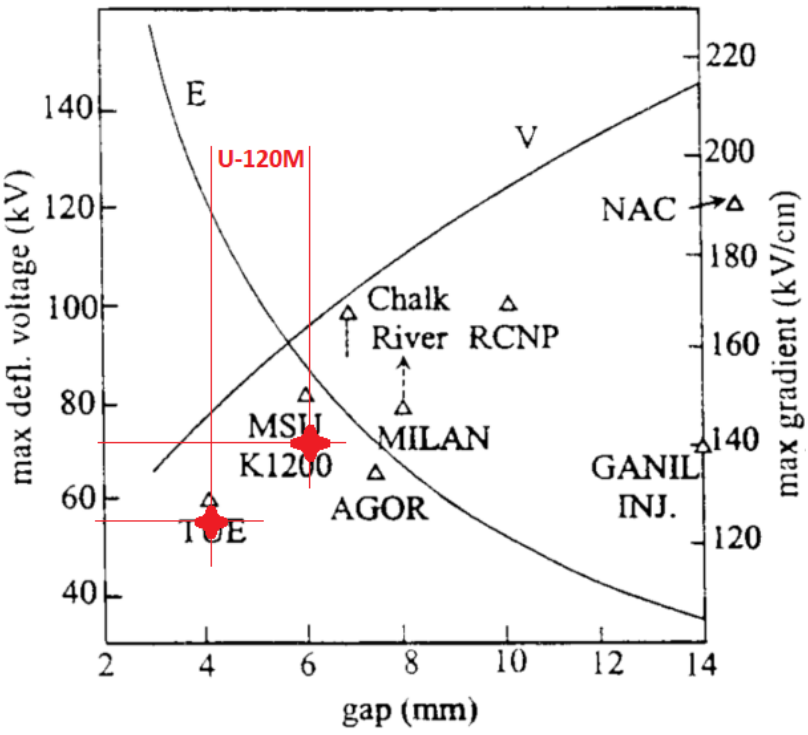

Figure 5.36: Empirical limits of deflector voltage and electric field for different electrodes gap sizes published in [33]. The red crosses indicate the design target values for the new U-120M deflectors.

5.4.2 Deflector 0

Thanks to the existence of the new harmonic coils, it is possible to replace the electromagnetic exciter with a new short deflector. This deflector is located at a radius of 524 mm and should serve as an extension of the azimuthal length of the current Deflector I, or

its replacement. As the beam orbits are not perfectly separated even at the aforementioned radius, this deflector comes into direct contact with the extracted beam. From the simulations carried out so far, it follows that this deflector is the only component of the entire new extraction system that inevitably comes into contact with the beam, and it is likely that the other components of the extraction system can be designed such that the extracted beam passes through them without any significant beam loss. For this reason, the extraction efficiency of Deflector 0 can be considered as a possible maximal efficiency of the entire extraction system for a given type of particle.

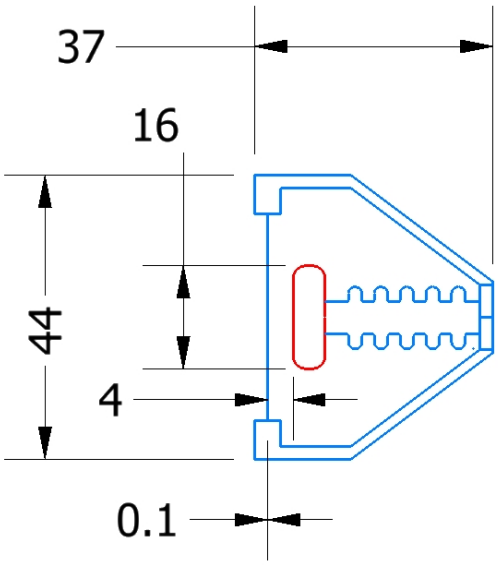

Figure 5.37: Deflector 0 cross-section drawing with basic dimensions in mm. The high voltage electrode has red color.

The choice of the shape of the deflector, i.e. its radius of curvature and the gap between the electrodes, is adapted to the characteristics of the beam at the extraction radius. When coherent oscillations are excited using the harmonic coils, the value of orbit separation at azimuth 182 ° is approximately 1.5 mm and in the P36.7A proton mode the radial width of the beam is approximately 2.4 mm, i.e the orbits are overlapping. For the electromagnetic exciter the radial size of the beam for similar orbit separation was practically the same. Due to the relatively short azimuthal length of the deflector, which is 22°, the radial size does not increase during the passage through the deflector. The size of the deflector gap is chosen to be 4 mm, i.e. large enough to accommodate the entire radial width of the beam with a small margin. From Fig. 5.36 the voltage limit for this gap size is approximately 70 kV. For the proton mode P36.7A the necessary voltage for sufficient extraction is 55 – 60 kV, i.e. far below the expected limit.

The septum is designed as a flat electrode with a thickness of 0.1 mm. The material used for the septum will likely be tungsten or tantalum, due to the high melting point. There is good experience with these materials when used as a deflector septum [56].

The high voltage electrode is constructed with a simple oval cross-section and a height of 8 mm. The height of the electrode is chosen as low as possible, but such that the entire height of the beam, even with an additional reserve, is located in a fully homogeneous electric field. The high voltage electrode is completely enclosed in a deflectors housing. Drawing of the Deflector 0 cross-section with basic dimensions is shown in Fig. 5.37. Parameters of the deflector are listed in Table 5.12. Electric potential distribution is

Table 5.12: Basic properties of Deflector 0.

Radial position of the septum	524 mm
Azimuthal position	182°
Azimuthal length	22°
Gap size	4 mm
Septum bending radius	508.4 mm
Septum height	32 mm
Septum thickness	0.1 mm
HV electrode bending radius	512.4 mm
HV electrode height	16 mm
Maximum expected operating voltage	~ -65 kV

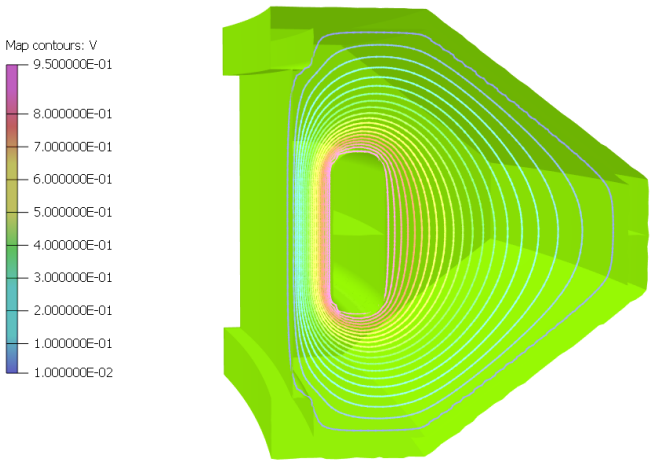

Figure 5.38: Electric potential distribution inside Deflector 0 for HV electrode potential +1 V. The color scale is in Volts.

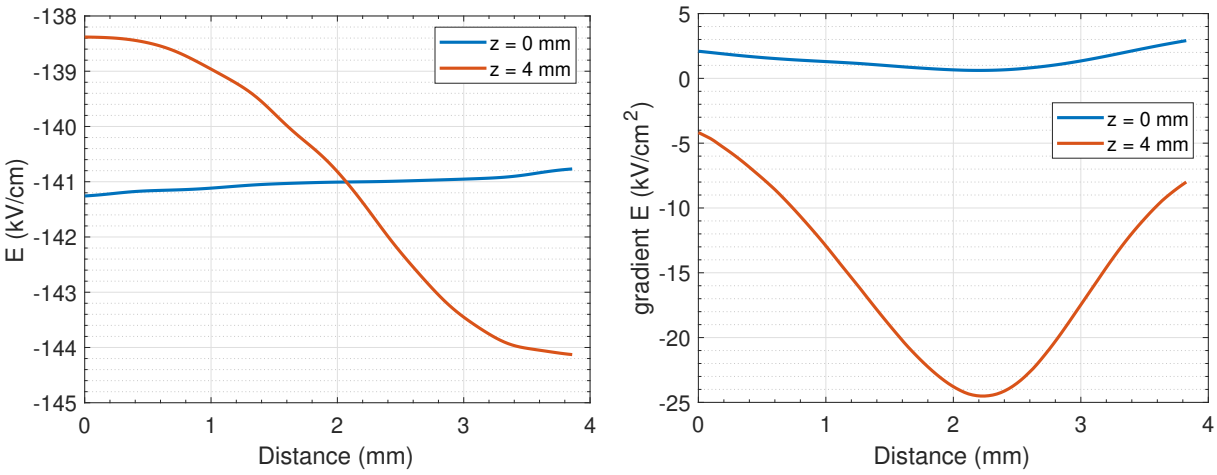

(a) Electric field

(b) Electric field gradient

Figure 5.39: Distribution of electric field and its gradient of the Deflector 0 for -55 kV at the HV electrode for different vertical coordinates. Details in text.

shown in Fig. 5.38 for applied voltage +1 V. Electric field and its gradient is shown in Fig. 5.39 for two vertical coordinates 0 mm and 4 mm. The electric field in cyclotron median plane, i.e. for z-coordinate 0 mm, is almost constant. For z-coordinate 4 mm the field becomes deformed due to the insufficient height of the high voltage electrode and the peak electric field gradient of approximately $-25\,\mathrm{kV/cm^2}$ appears in the middle of the deflector gap, see Fig. 5.39b. Thus the height of the deflector high voltage electrode should be probably increased to 10 – 12 mm.

5.4.3 Deflector 0 transparency

In this paragraph, the parameters of the beam at the entrance and exit of Deflector 0 will be presented and an analysis of the beam losses will be performed. The beam is first examined at azimuth 183°, i.e. just behind the entrance of the deflector which starts at azimuth 182°. This is a beam, part of which has already been lost on the leading edge of the deflector septum with a thickness of 0.1 mm as indicated by the straight left boundary of the $R-Pr$ phase ellipse in Fig. 5.40a. From the $R-Z$ phase ellipse in the same figure it can be seen that the full radial dimension of the beam just after entering the deflector is 2.4 mm. Fig. 5.40b shows the situation at the exit of the deflector, i.e. at azimuth 205°. Here the radial dimension of the beam has already increased to 3.5 mm, but in the ideal case it would fit fully into the deflectors gap.

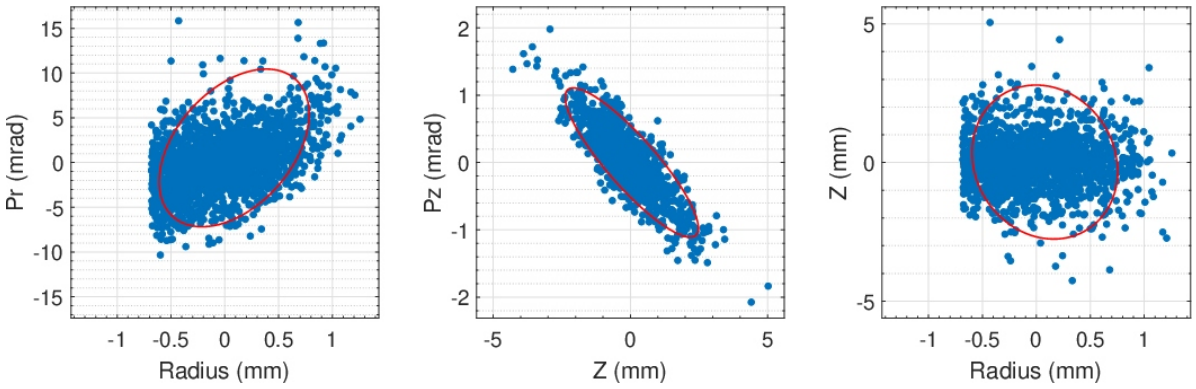

(a) Beam phase ellipses at azimuth 183°.

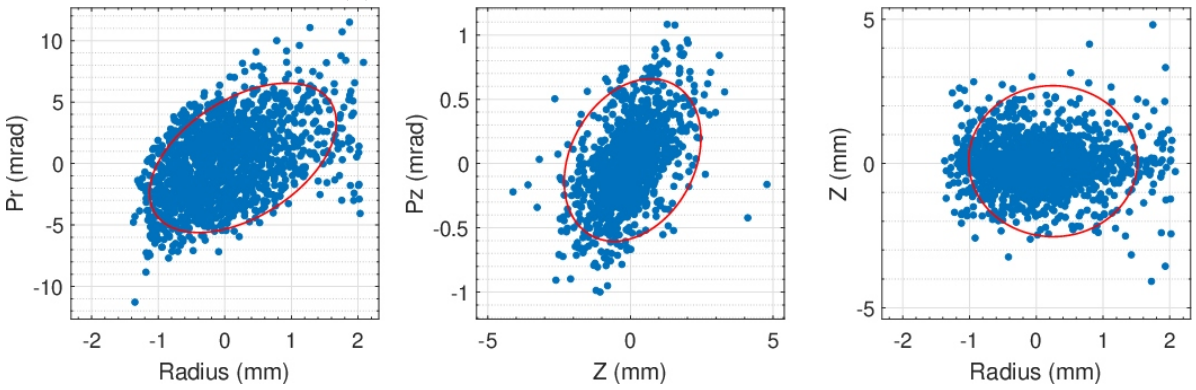

(b) Beam phase ellipses at azimuth 205°.

Figure 5.40: Beam properties at the Deflector 0 entry (183°) and its exit (205°). The ellipses in the individual plots are used for the emittance calculation.

The beam losses on Deflector 0 are shown in Fig. 5.41. The HV electrode losses indicated on the right side of Fig. 5.41b will likely be eliminated or significantly reduced

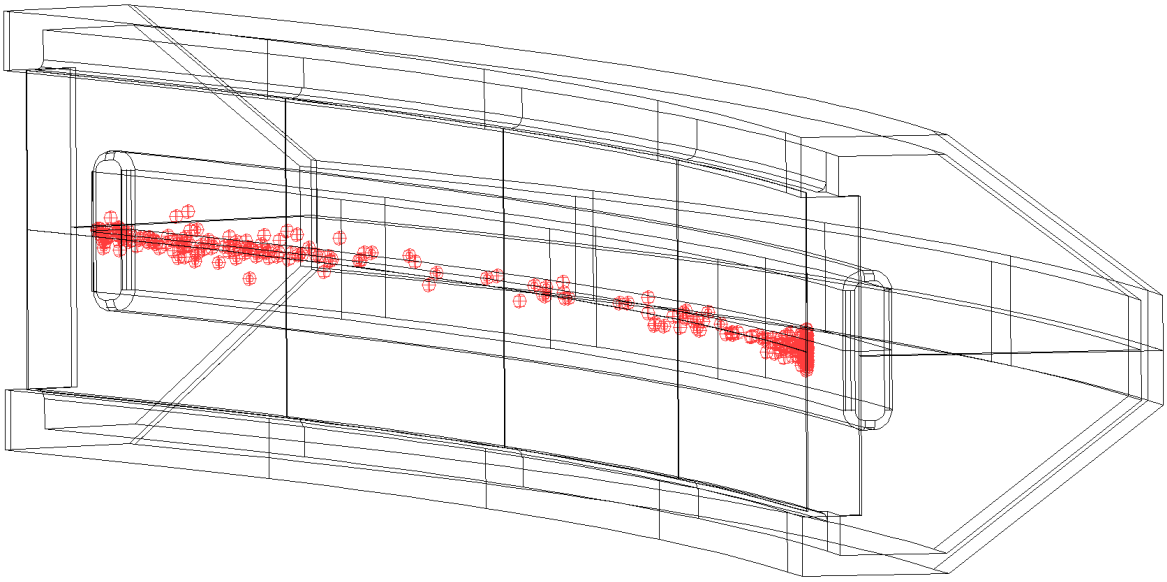

(a) Front view. Deflector entry on the right.

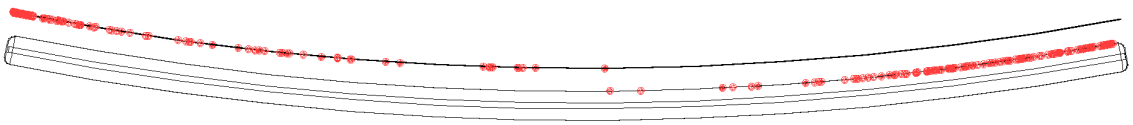

(b) Top view. Deflector beginning on the left.

Figure 5.41: Particle losses indicated as red points in the Deflector 0. For clarity, the top view contains only the septum end HV electrodes.

during further optimization. About 36% of the Deflector 0 losses are at the leading edge of the septum, which is about 7% of the total beam entering the extraction process. Based on this result, a total extraction efficiency for a fully optimized extraction system can be expected close to 90% for the mode, for which the extraction system will be optimized.

The simulations are performed for two levels of harmonic coils' currents HC1/HC2 equals to 800/240 A and 800/80 , respectively. For the HC2 coil current 240 A the orbit separation reaches 1.5 mm at the extraction radius and the Deflector 0 transparency is ∼86 %. Necessary voltage on the deflector for this case is near the practical limit −90 kV specified in 5.36. For the HC2 coil current lowered to 80 A the orbit separation drops to only 1.2 mm, but the necessary voltage of the Deflector I decreases to −73 kV. The ability to reduce the deflectors voltage is a much appreciated feature and for that reason the variant with lower HC2 current is preferred and the Deflectors 0 transparency in this case is 81 %. The orbit separation and orbit center position for various harmonic coil currents is shown in Fig. 5.42. An overview of the distribution of the losses in the Deflector 0 and beam parameters on its entrance and its exit is given in Tab. 5.13. The values in brackets refers to the simulations performed with HC1/HC2 currents 800/240 A and −90 kV on the Deflector I.

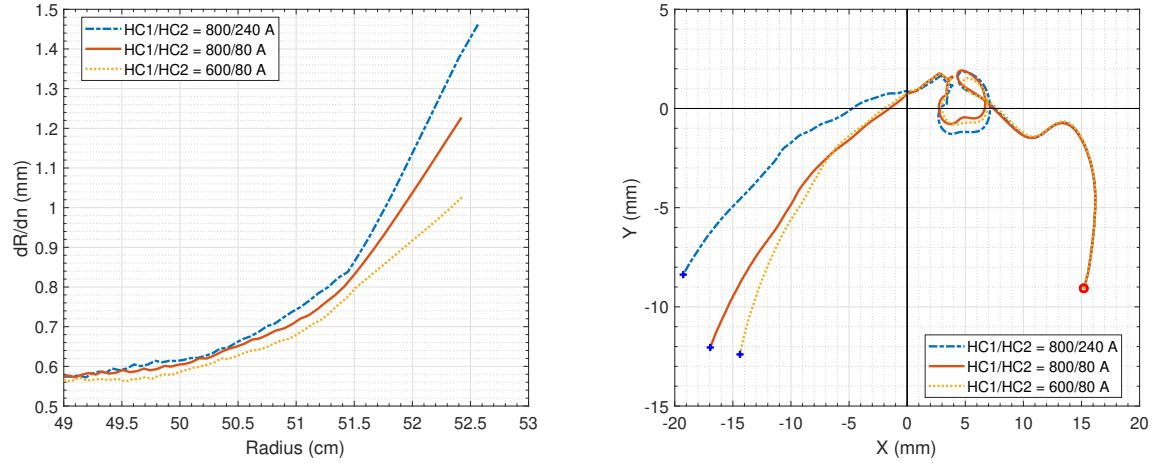

(a) Orbit separation.

(b) Orbit centers evolution.

Figure 5.42: The orbit separation at the extraction radius 524 mm and the orbit centering for various HC currents in the proton mode P36.7A. The red circles indicate particle start position, the blue crosses indicate the last orbit.

Table 5.13: Beam losses distribution and calculated beam properties at the entrance and at the exit of the Deflector 0 for HC1/HC2 currents 800/80 A. The values in brackets refers to the simulations performed with HC1/HC2 currents 800/240 A. See text for further details.

Parameter	Azimuth 183°	Azimuth 205°
Mean Radius (mm)	524.8	527.0
Mean Pr (mrad)	4.8	12.9
mean Pz (mrad)	0	0
$\epsilon_{R,Z}$ (π mm mrad)	1.3	2.3
$\epsilon_{R,Pr}$ (π mm mrad)	3.9	5.3
$\epsilon_{Z,Pz}$ (π mm mrad)	0.9	1.0
$2\sigma_R$ (mm)	0.8	1.4
$2\sigma_{Pr}$ (mrad)	7.1	6.3
$2\sigma_{Pz}$ (mrad)	0.9	0.6
Full radial size (mm)	1.9	3.5
Mean Energy	36.8 (36.5) MeV	
$2\sigma_E$	0.2 MeV	
Number of particles entering the deflector	1820 (1824)	100%
Total losses in the deflector	346 (265)	19.0% (14.5%)
Losses on the septum	331 (184)	18.2% (10.1%)
Losses on the HV electrode	15 (81)	0.8% (4.4%)
Deflector 0 transparency	**81.0% (85.5%)**	

5.4.4 New Deflector I

At the entrance of the Deflector I at the azimuth 210° , the full radial size of the beam depends on exact extraction system settings and varies between 4 and 4.5 mm. In the case of using Deflector I without any radial focusing component, i.e. if the high voltage electrode has a simple rectangular cross-section, the beam radial size grows as it passes via the deflector into the magnetic fringe field. At the exit of the Deflector I at azimuth 268°, the radial beam size is approximately 14 mm. For the HC1/HC2 coils current 800/80 A and the orbit separation 1.2 mm associated with it, an electric field in Deflector I of approximately −120 kV/cm is required to pull the beam to a radius of 600 mm at an azimuth of 300°. For a deflector gap of 14 mm, the required voltage is −170 kV. However, such a deflector probably cannot be constructed in view of the limitations mentioned in paragraph 5.4.1. For this reason, I designed a deflector with a gap of 6 mm with an electric field gradient such that the radial width of the beam is maintained along the entire path of the beam passing through the deflector. The necessary voltage for the 6 mm gap is then −73 kV, with the electric field gradient 40 kV/cm^2 and VE value of 1.35×10^4 kV^2/cm. These values are under the limits mentioned in [33, 65]. I assume that by further optimization, especially by adjusting the harmonic coil currents and increasing the voltage on Deflector 0, the necessary electric field and thus the VE value will be further reduced.

Due to the complicated beam trajectory when passing through the deflector, the shape of the deflector electrodes cannot be approximated by a simple arc with one radius of curvature. For that reason, Deflector I is divided into three azimuthal sections of approximately equal length, each with slightly different bending radius. The design parameters of the deflector are listed in Table 5.14. The deflector, like the Deflector 0, is designed as enclosed in the housing. This is due to the possibility of introducing the so-called oxygen treatment [56], when pure oxygen is injected into the deflector space after a short-term shutdown of the beam. This procedure will treat the electrode surfaces in case of high voltage discharges so that further operation of the deflector is possible. The distribution of the electric potential and the electric field for a voltage at the HV electrode of +1 V is shown in Fig. 5.44. The electric field and its gradient for a voltage of −73 kV are shown in Fig. 5.45.

Table 5.14: Basic properties of the new Deflector I.

	Section I	Section II	Section III
Beginning azimuth	210°	228°	250°
Azimuthal length	18°	22°	18°
Center of curvature X / Y (mm)	107.9 / 59.33	91.33 / 36.44	56.35 / -28.33
Septum bending radius (mm)	645.72	617.88	544.32
HV electrodes bending radius (mm)	652.12	624.28	549.88
Septum height	36 mm		
HV electrode height	24 mm		
Septum thickness	0.4 mm		
Maximum expected operating voltage		~ -80 kV	

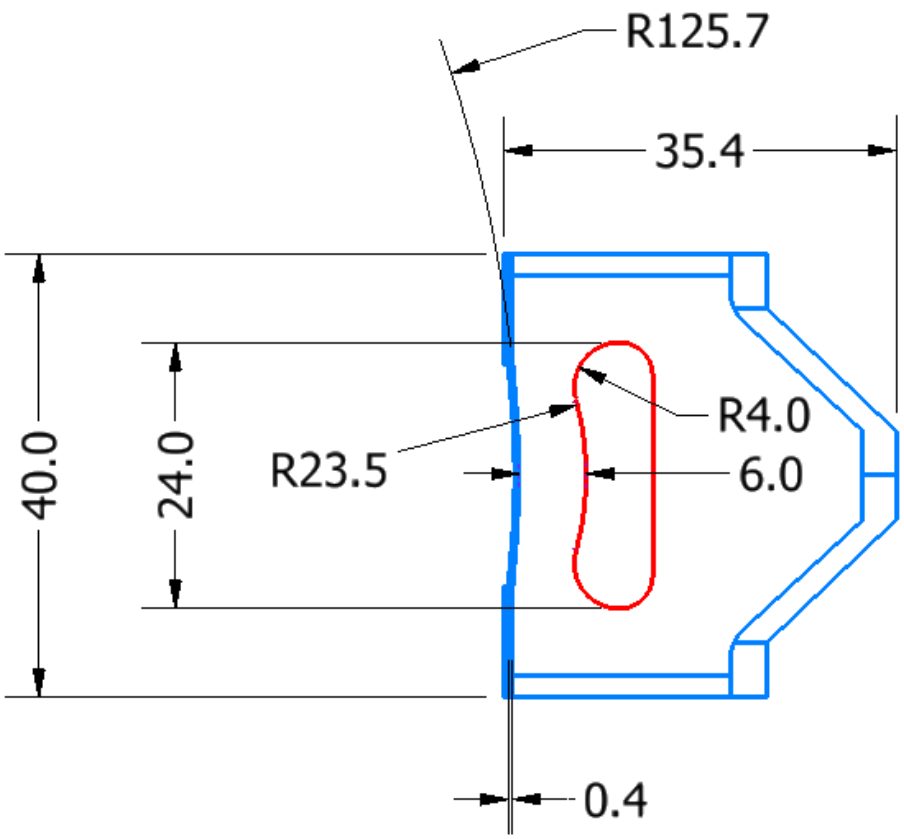

Figure 5.43: New Deflector I cross-section drawing with basic dimensions in mm. The high voltage electrode has red color, the septum and the casing is blue. The insulator is not shown for clarity.

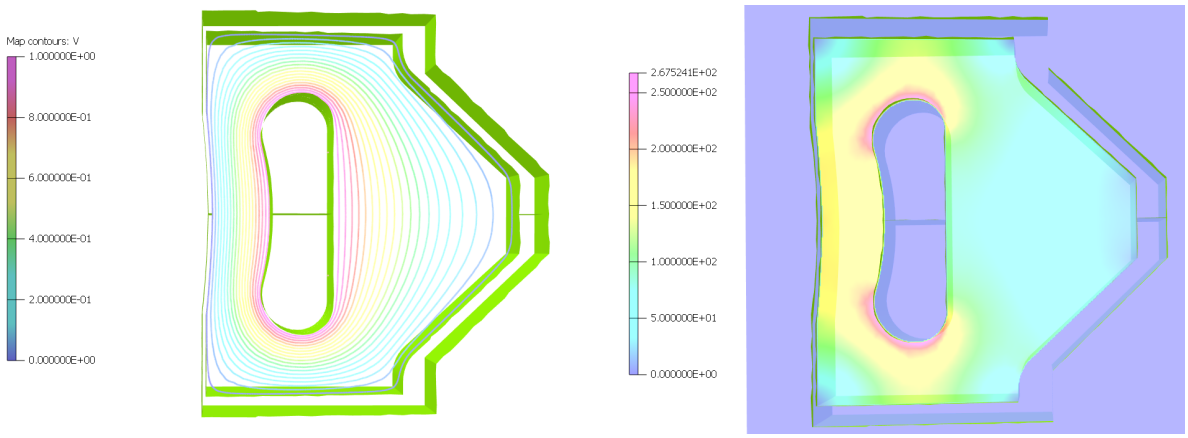

(a) Electric potential distribution. The color scale is in Volts.

(b) Electric field distribution. The color scale is in V/m.

Figure 5.44: Electric potential and electric field distribution inside the new Deflector I for HV electrode potential +1 V.

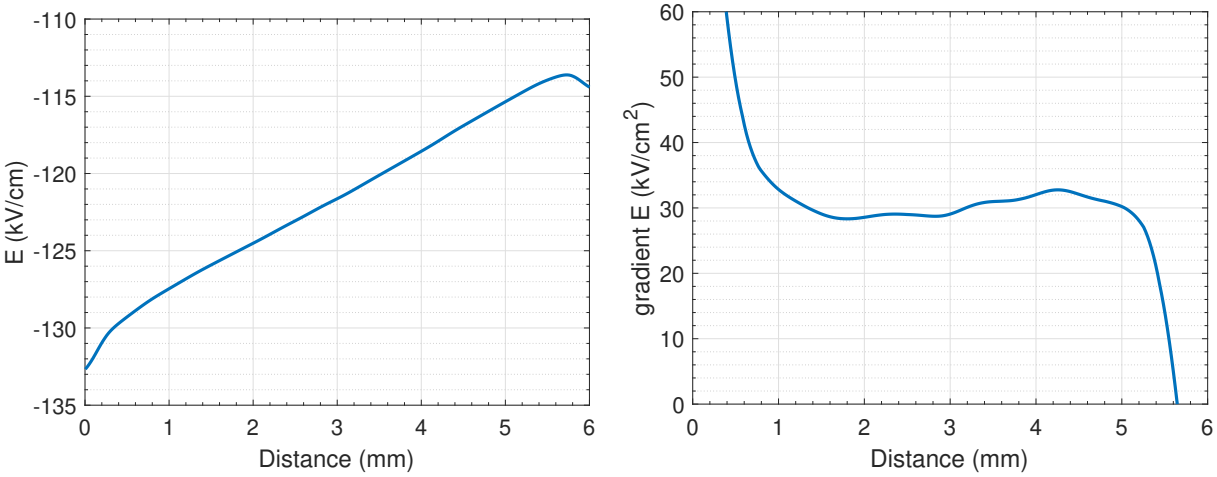

(a) Electric field.

(b) Electric field gradient.

Figure 5.45: Distribution of electric field and its gradient of the new Deflector I for −73 kV at the HV electrode. See text for further details.

For the mode with HC2 current 80 A the losses are distributed mainly at the deflector's end as can be seen in Fig. 5.46. The electric field gradient is not large enough to focus the beam to fit fully into the deflector gap. At the end of the deflector, losses appear on the high voltage electrode and on the septum, which clearly indicate this. It is likely that this deflector can be designed almost lossless after the electric field gradient is fully optimized.

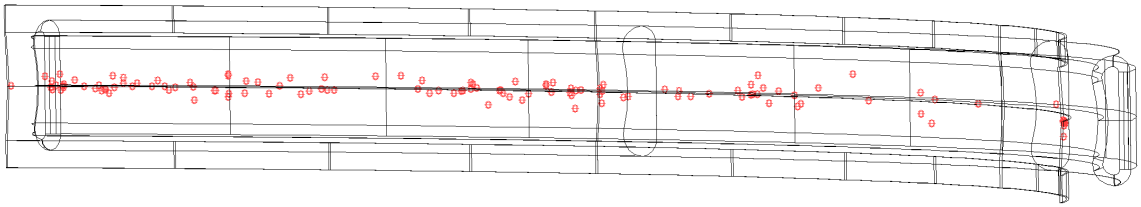

(a) Front view. Deflector entry on the right.

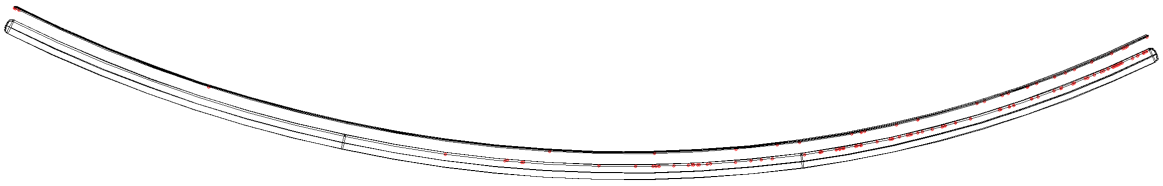

(b) Top view. Deflector entry is located on the left.

Figure 5.46: Particle losses indicated as the red points in the Deflector 1 for the mode with HC2 = 80 A. For clarity the deflector casing is not displayed.

Beam phase ellipses at azimuths 210 ° and 270 ° corresponding to the entrance and 2 ° after the exit of the Deflector I are shown in Fig. 5.15. Beam properties related to the phase ellipses are listed in Table 5.15.

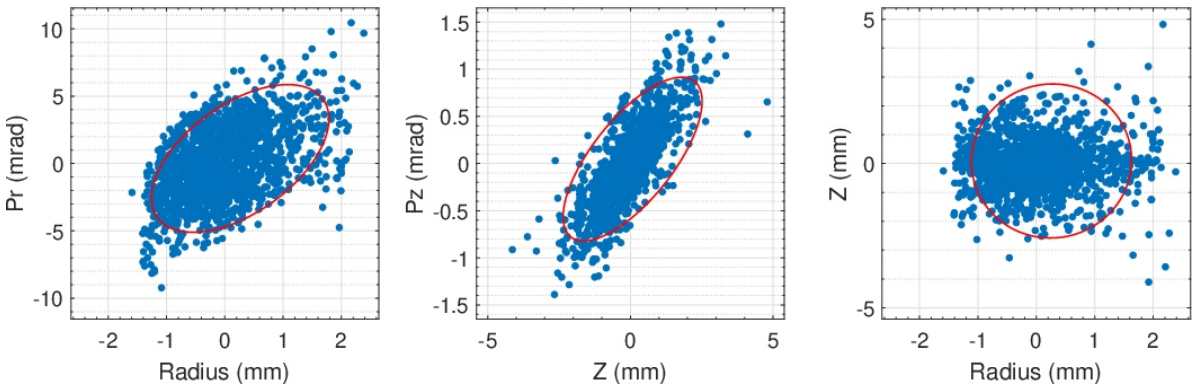

(a) Beam phase ellipses at azimuth 210°.

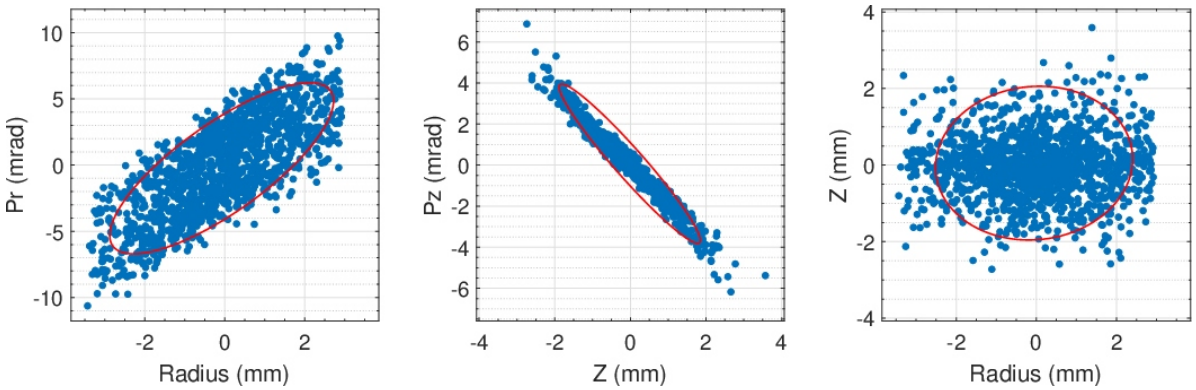

(b) Beam phase ellipses at azimuth 270°.

Figure 5.47: Beam properties at the Deflector 1 entry (210°) and 210° after its exit (270°).

Table 5.15: Beam losses distribution and calculated beam properties at the entrance and at the exit of the Deflector I for the HC1/HC2 currents 800/80 A. The values in brackets refers to the HC1/HC2 currents 800/240 A.

Parameter	Azimuth 210°	Azimuth 270°
Mean Radius (mm)	527.8 (525.7)	575.1 (573.3)
Mean Pr (mrad)	12.1 (4.8)	95.7 (101)
mean Pz (mrad)	0	0.1 (0)
$\epsilon_{R,Z}$ (π mm mrad)	2.6 (1.8)	3.5 (2.8)
$\epsilon_{R,Pr}$ (π mm mrad)	5.0 (5.2)	7.9 (7.5)
$\epsilon_{Z,Pz}$ (π mm mrad)	1.1 (0.8)	1.4 (1.2)
$2\sigma_R$ (mm)	1.5	2.9 (2.3)
$2\sigma_{Pr}$ (mrad)	5.5 (5.2)	7.3 (6.1)
$2\sigma_{Pz}$ (mrad)	0.8	3.1 (1.7)
Full radial size (mm)	4.0 (4.5)	6.4 (6.3)
Mean Energy	36.8 (36.5) MeV	
$2\sigma_E$	0.2 MeV	
Number of particles entering the deflector	1493 (1559)	100 %
Total losses in the deflector	126 (87)	6.9 % (5.6 %)
Deflector I transparency	**91.6 % (94.4 %)**	

5.4.5 Magnetic channels

Even in the case of a fully optimized electric field gradient of the Deflector I, the radial expansion of the beam in the magnetic fringe field does not allow an efficient extraction. Without the use of additional focusing elements, the radial width of the beam at the beam line entrance is approximately 60 mm. By constructing suitable passive magnetic channels (MC), i.e. magnetic channels consisting of only iron bars, the entire beam passing through the system of electrostatic deflectors can be focused to a spot of approximately 10×10 mm.

However, the construction of magnetic channels is a rather demanding process. Passive magnetic channels work on the principle of inserting a suitable ferromagnetic structure into the space of the magnetic field of the accelerator. The inserted structure is magnetized and influences the magnetic field in its surroundings. A suitable design of such element will create a proper focusing radial gradient of the magnetic field in the area of the beam passage. In addition to this effect, however, the embedded structure also affects the entire remaining magnetic field, i.e. the field in the entire acceleration region and thus changes the properties of the accelerated beam. There is a small change in the mean magnetic field on the order of a few Gauss shifting the RF phase of the beam and also an additional first harmonic component of the magnetic field. In the case of the U-120 cyclotron, which has a set of trim coils for the fine adjustment of the magnetic field, it is possible to compensate for the change in the mean field to a large extent by changing the setting of the currents in the trim coils. The contribution of the magnetic channels to the first harmonic component is usually compensated by inserting an identical structure at the opposite azimuth [64].

In addition to the magnetic field map of the real magnetic channel, the SNOP simulator can account for its analytical version into the acceleration process. This is a property that adjusts the acceleration field in a defined area by introducing the selected radial gradient of the vertical component of the magnetic field. The simplified channel created in this way does not affect the internal magnetic field of the accelerator and represents a kind of idealized version of the real magnetic channel. Using this property, the most suitable parameters of the constructed channel can be empirically found and a real magnetic channel can be created according to them.

The magnetic channels for the new extraction system are designed as replacements for the current Deflectors II and III. The first magnetic channel MC1, like the Deflector II, has an azimuthal length of 23 ° and starts at an azimuth of 272 °. The second MC2 magnetic channel replacing Deflector III has an azimuthal length of 55 ° and starts at an azimuth of 305 °. Additional parameters of the MC1 and MC2 channels are listed in Tab. 5.16. Parameters of the beam extracted to the extraction point using the analytical version of the magnetic channels are listed in Tab. 5.17.

The focusing properties of the designed magnetic channels are evident from Fig. 5.48, where a comparison of the beam phase ellipses of the beam at the cyclotron output is shown for the beam output without using a magnetic field gradient and for the beam focused using appropriate magnetic field gradients. In the next steps, the design of real magnetic channels and adaptation of the newly designed extraction system to their influence on the acceleration process will be carried out.

Calculation of the magnetic channels

For a first approximation and estimation of the parameters of the magnetic channels, the method by introducing the relevant gradients into the beam dynamics simulator is

Table 5.16: Basic properties of proposed magnetic channels.

Parameter	MC 1	MC 2
Beginning azimuth	272°	305°
Azimuthal length	23°	55°
Center of curvature X / Y (mm)	54.16 / 4.58	−125.53 / 330.3
Septum bending radius (mm)	565.6	939.16
Magnetic field deposit in the MC center (T)	0	0
Magnetic field gradient (T/m)	−10	−14
Radial length of constant gradient region (mm)	12	12

Table 5.17: Properties of the focused output beam at the Extraction Point.

Mean Radius (mm)	707.1
Mean Pr (mrad)	332.3
mean Pz (mrad)	0.1
$\epsilon_{\mathrm{R,Z}}$ (π mm mrad)	4.5
$\epsilon_{\mathrm{R,Pr}}$ (π mm mrad)	8.0
$\epsilon_{\mathrm{Z,Pz}}$ (π mm mrad)	1.1
$2\sigma_{\mathrm{R}}$ (mm)	2.8
$2\sigma_{\mathrm{Z}}$ (mm)	2.0
$2\sigma_{\mathrm{Pr}}$ (mrad)	14.7
$2\sigma_{\mathrm{Pz}}$ (mrad)	5.7
Full radial size (mm)	9.0
Full vertical size (mm)	7.9
Mean Energy	36.8 MeV
$2\sigma_{\mathrm{E}}$	0.2 MeV

very convenient. Based on the estimated parameters of the necessary gradients, a method based on the description of the magnetic field using infinitely long rectilinear shims can be used for further design step. The calculation is based on the assumption that the ferrous material is fully magnetized. It is then possible to calculate the magnetic field using the following analytical expressions [64].

The radial profile of the resulting magnetic field is calculated as

$$B(r) = M_0 \int_{h_1}^{h_2} (B_{loop}(r, r_2, h) - B_{loop}(r, r_1, h))dh, \tag{5.1}$$

where B_{loop} is calculated as

$$B_{loop}(r, R, h) = \frac{sc}{\sqrt{(r+R)^2 + h^2}} \times \left(K(r, R, h) + \frac{R^2 - r^2 - h^2}{(R-r)^2 + h^2} E(r, R, h) \right). \tag{5.2}$$

The coefficient sc equals $sc = \mu_0/2\pi$ and r_1, r_2, h_1, h_2 are the dimensions depicted in Fig. 5.49. They specify the radial and axial sizes and the position of the calculated iron bar.

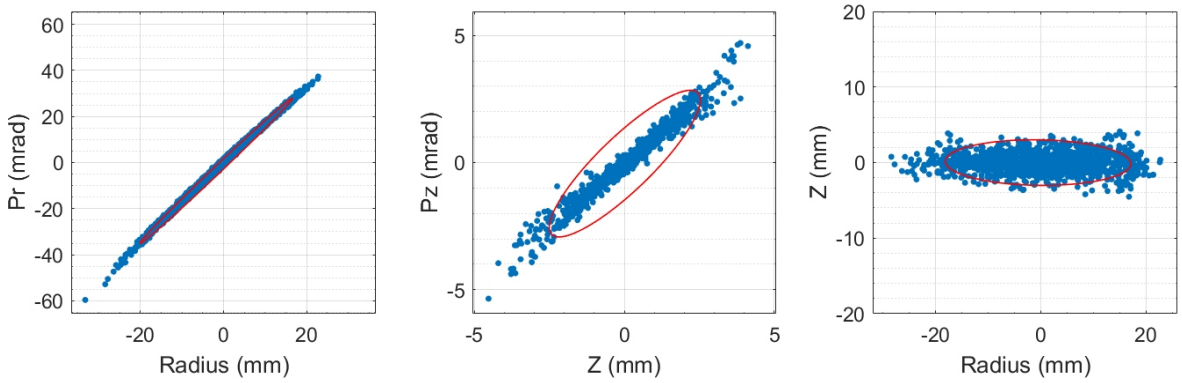

(a) Beam phase ellipses for the unfocused beam.

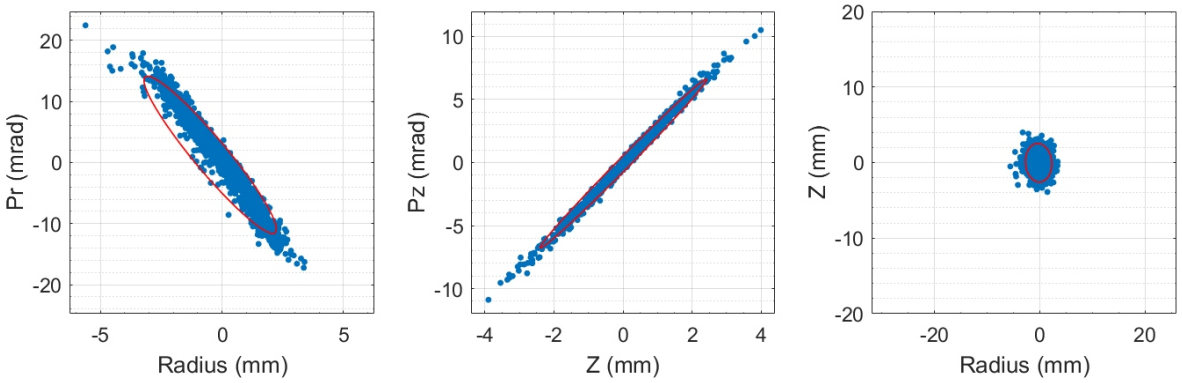

(b) Beam phase ellipses for properly focused beam.

Figure 5.48: Comparison of the phase ellipses for the beam at the Extraction point of the cyclotron. For clarity, the $R - Z$ planes have the same radial scale.

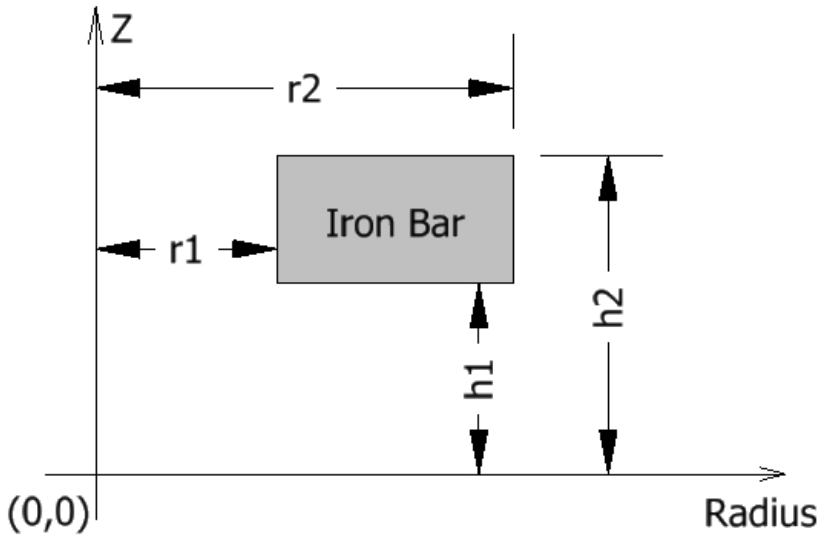

Figure 5.49: 2D cross-section of an infinitely long iron bar.

Magnetization coefficient M_0 describing the magnetic field strength inside the magnetized material is for the steel 1010 equal to $M_0 = 1697724.55$ A/m. The functions K and E can be expressed as

$$K(r,R,h) = \frac{\pi}{2}\text{FHYPER}\left(\frac{1}{2},\frac{1}{2},1,k,(r,R,h)\right), \tag{5.3}$$

$$E(r,R,h) = \frac{\pi}{2}\text{FHYPER}\left(\frac{1}{2},-\frac{1}{2},1,k,(r,R,h)\right), \tag{5.4}$$

where

$$k(r,R,h) = \frac{4rR}{(r+R)^2+h^2}, \tag{5.5}$$

and FHYPER is a hypergeometric function defined as

$$\begin{aligned}\text{FHYPER}(a,b,c,z) &= 1 + \sum_{k=1}^{\infty}\left[\prod_{l=0}^{k-1}\frac{(a+l)(b+l)}{(1+l)(c+l)}\right]z^k = \\ &= 1 + \frac{ab}{c}\frac{z}{1!} + \frac{a(a+1)(b(b+1)}{c(c+1)}\frac{z^2}{2!} + \ldots \quad .\end{aligned} \tag{5.6}$$

Analytical models of the field of the magnetic elements are derived from formulas for evaluating the magnetic field of a current coil [64]

$$B_{coil}(r) = \frac{sc_c}{\sqrt{(r+r_c)^2+h_c^2}} \times \left(K(r,r_c,h) + \frac{r_c^2 - r^2 - h_c^2}{(r_c-r)^2+h_c^2}E(r,r_c,h_c)\right), \tag{5.7}$$

where coefficient sc_c includes the current in the coil I in Amper$\times$ turns

$$sc_c = 2\frac{\mu_0}{2\pi}I, \tag{5.8}$$

and center radius r_c and center height h_c can be expressed as

$$r_c = \frac{r_2+r_1}{2}, \qquad h_c = \frac{h_2+h_1}{2}. \tag{5.9}$$

When an optimal 2D shape of the magnetic channel bars based on the desired gradient is found, see Fig. 5.50, a 3D CAD model of the real structure is created and simulated using Opera finite element simulator [66]. The analytical approximation usually shows very good agreement with simulations in 3D field simulators. In the case of the fringe field of the U-120M cyclotron, the field in the area of the proposed magnetic channels decreases very quickly, see Fig. 4.9a. Up to now the agreement between the results of calculations using the analytical 2D method and the finite element analysis for Magnetic channel II at radius 600–680 mm is not satisfying. Lower magnetizing field probably affects the results as it is shown in Fig. 5.51.

Each of the magnetic channels affects the magnetic field at lower radii to a different extent. Fig. 5.52 shows the influence of both channels up to a radius of 540 mm and the sum of their contributions. Without compensation of these contributions, there is an undesirable change in the mean magnetic field and a noticeable RF phase shift of the accelerated

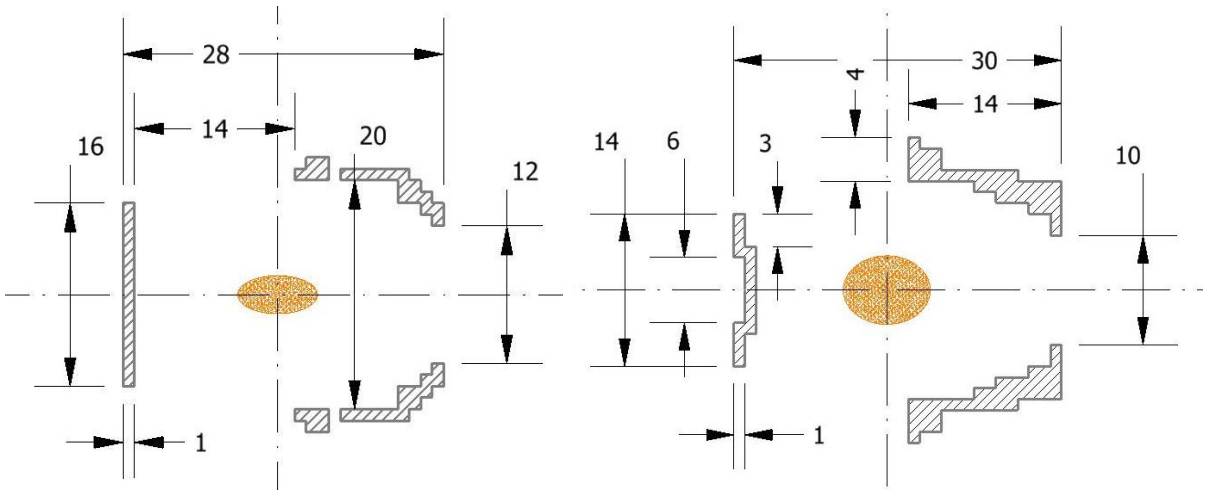

(a) Cross-section of MC I. (b) Cross-section of MC II.

Figure 5.50: Cross-section of the magnetic channels with overall dimensions. Position of the beam inside the channel center is marked with the ellipse. The iron bars are hatched.

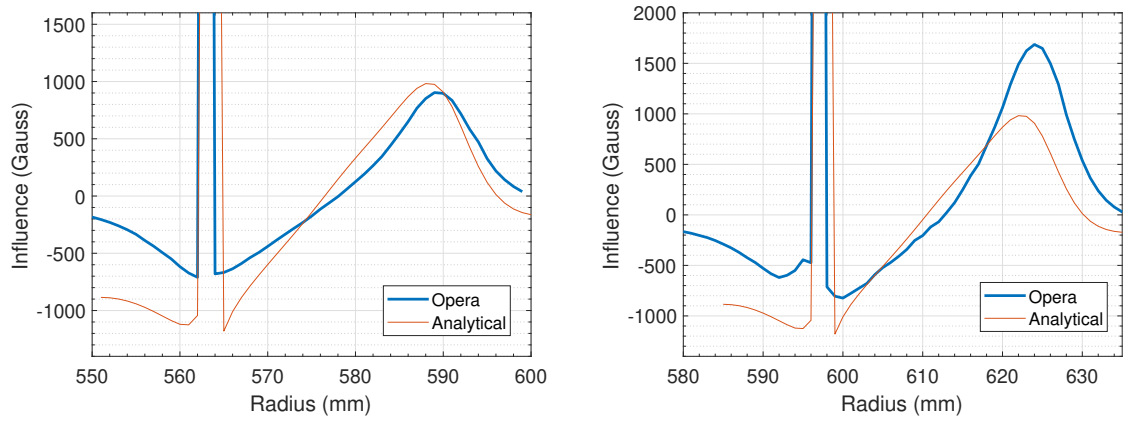

(a) Magnetic field of MC I with channels center at $r = 576\,\text{mm}$. (b) Magnetic field of MC II with channels center at $r = 610\,\text{mm}$.

Figure 5.51: Comparison of theoretical calculation results and finite element analysis of the magnetic channel magnetic field along radius.

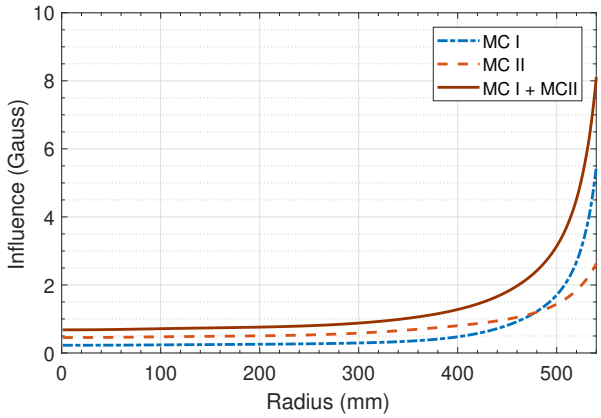

Figure 5.52: Influence of the magnetic channels to the magnetic field at lower radii.

particles, as shown in Fig. 5.53. Compensation of the contribution of magnetic channels is performed using the Nelder-Mead simplex algorithm [39] implemented in Matlab [46]. By searching for the minimum of the functional of the difference of trim coils deposit and influence of the magnetic channels, a suitable combination of trim coils currents can be found, see Fig. 5.54a. After introducing the main magnetic field correction made in this way, the beam RF phase deviation returns close to the original values.

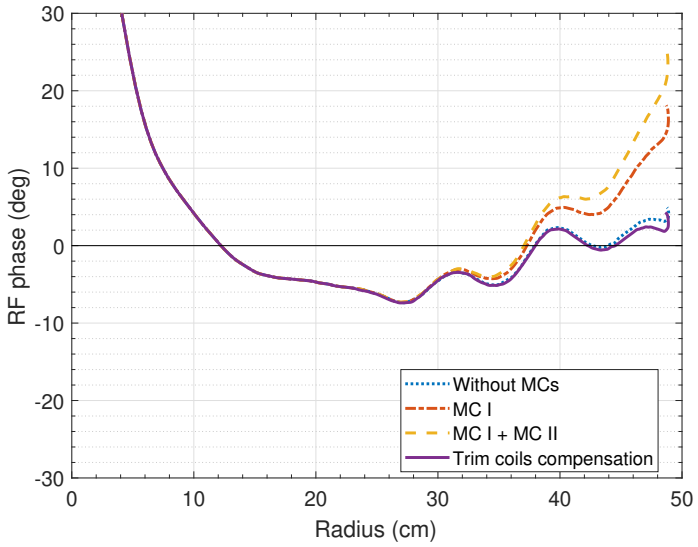

Figure 5.53: Change in the central particle RF phase after introducing the magnetic channels and after compensation using the trim coils.

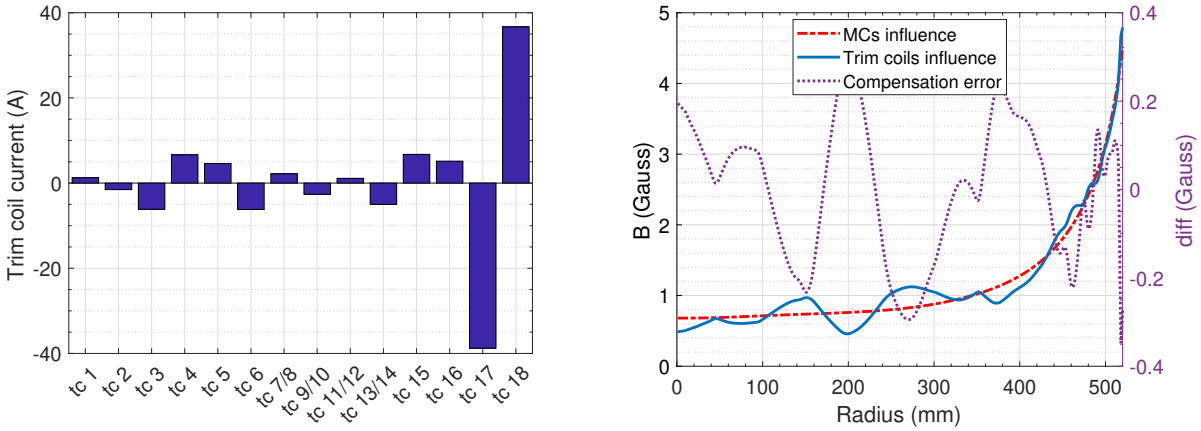

(a) Trim coils currents.

(b) Compensation of the magnetic channels.

Figure 5.54: Comparison of theoretical calculation results and finite element analysis of the magnetic channel magnetic field.

As the magnetic channels affect the acceleration process, minor setup changes have to be done after introducing them into the extraction system. Without additional correction of the position and voltage of the deflectors, the deflectors transparency drops to approximately 50 %. After increasing the voltage of Deflector 0 by 1 kV and rotating it by $-0.4°$ and moving Deflector I by approximately 1.5 mm towards a higher radius and reducing its voltage by 1 kV, the extraction efficiency gets largely restored. Passage of the extracted

beam though the magnetic channels structure is lossless and the total extraction efficiency in the proton regime of P36.7A is 74 % for the system defined in this way. An overview of the total extraction efficiency together with the efficiencies of the components of the extraction system is given in Table 5.18.

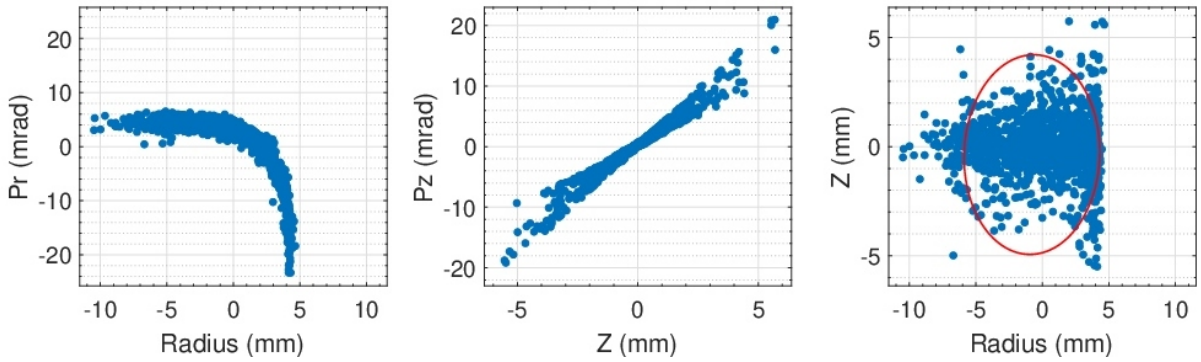

Figure 5.55: Phase ellipses of the extracted beam at the extraction point.

It should be mentioned that the design and optimization of the system of magnetic channels has not yet been completed. It is necessary to increase the gradient of the magnetic field in the magnetic channel II, since the optimal focusing of the beam at the extraction point is not achieved. It is also necessary to optimize the position of both magnetic channels such that there is no deformation of the phase ellipses, especially the deformation of the radial momentum, as it is shown in Fig. 5.55. Optimizing the entire extraction system is a rather complex process that involves a number of iterations. Any change in the parameters of an individual component or acceleration parameter affects the extraction efficiency. In the case of the deflectors, finding the optimal setting is a compromise between the extraction efficiency and the deflectors voltage, which should be kept as low as possible. In the case of magnetic channels, it should be bared in mind that the less ferromagnetic material is needed for their proper functioning, the less is the need to compensate for its negative effect on the magnetic field.

The proposed extraction system will be subsequently further developed and a complex sensitivity analysis to determine the key parameters of accelerator settings leading to optimized extraction process will be done at a final stage of the design.

Table 5.18: Overall parameters of the extraction system optimized for proton P36.7A mode.

Transparency of Deflector 0	84 %
Transparency of Deflector I	90 %
Transparency of Magnetic channels	100 %
Overall extraction system efficiency	**74 %**

5.4.6 Extraction efficiency for other modes

It can be expected that for the other acceleration modes it will be possible to achieve similar or better extraction efficiency as for the proton mode at the highest energy due

to the change in the positions of the individual extraction system elements. In the case of magnetic channels, for the lower energies of protons and other ions, it will probably be necessary to develop a modular system that will allow for each channel to adapt the shape of its magnetic field and the generated gradient to the lower magnetic field at low energy regimes, where the magnetization of the iron may not be sufficient. This idea has not yet been elaborated in detail, but its principle should be to assemble the final ferromagnetic rod of the magnetic channel from smaller rods of size, for example, 1×1 mm and enclose it in an adaptive housing.

For the ^{3}He mode at 54 MeV, the full radial size of the beam at the extraction radius is equal to 2.9 mm and the orbit separation reaches 2.4 mm. Transparency of Deflector 0 is 74 % after rotating it by $-0.4°$. For the 40 MeV α particle mode, the separation at the extraction radius 524 mm is only 1.5 mm. After the extraction radius increases to 530 mm the orbit separation rises to 3.3 mm. The full size of the beam at this radius is 3.8 mm and the transparency for Deflector 1 is 65 %. For this case, it will be advantageous to slightly widen the gap of Deflector 0 to 5–6 mm so that the radial dimension of the beam fit into the deflectors gap with a reserve. Accordingly the gap has to be widened also on the Deflector I.

5.5 Central region modification

Based on the simulations carried out as part of this dissertation, it seems the central region can be easily modified to increase beam intensity by reducing the losses on the inner wall of the puller. Part of the useful beam is the current central region configuration is blocked by an edge of the inner wall of the puller, which is 6 mm longer than it should be. In the Durycnm program, the length of the edge is defined to be 6 mm, but in the actual version of a real puller this wall has a length of 12 mm. It will be advantageous to remove the excess length of this edge by cutting the puller edge at an angle of 45° as it is indicated in Fig. 5.56, where the magenta dots represent the particles lost at the puller surface. The proposed treatment will increase the intensity of the inner beam for high magnetic field modes, especially for the light particles. For the ^{3}He 54 MeV mode the central region beam losses decreases by 32 %.

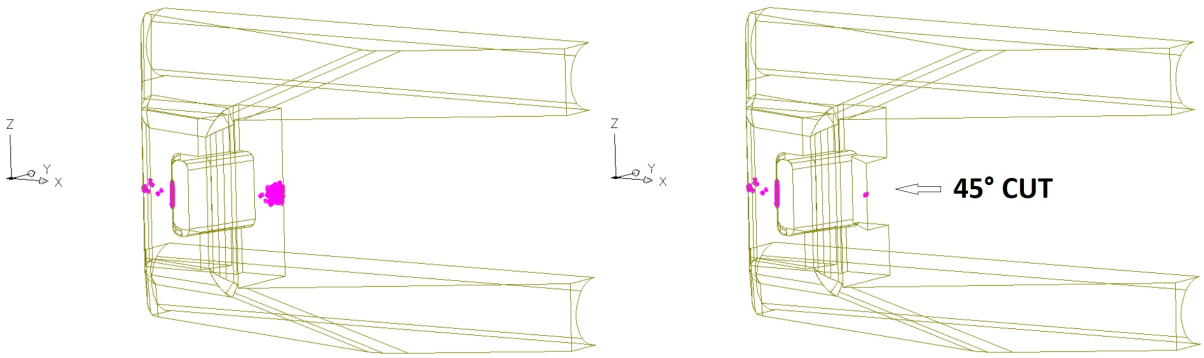

(a) Actual puller configuration. (b) Proposed puller modification.

Figure 5.56: Puller side view with the proposed 45° cut. The magenta dots indicate particle losses on the puller surface.

6 Conclusion

Based on the results achieved in this dissertation, it can be assumed that the construction of a new system for the extraction of positive particles at the U-120M cyclotron is feasible and that the new design will provide satisfactory efficiency. Performed numerical simulations of the extraction process, including realistic 3D maps of the electric and the magnetic fields of the extraction elements, indicate an extraction efficiency in the region of 70–80%.

The simulations were carried out for the proton mode with an energy of 36.7 MeV. This mode can not be performed using the original extraction system consisting of three deflectors at all due to the impractically high intensity of the electric field on the electrode of the first deflector of −230 kV/cm. In the newly designed extraction system, the electromagnetic exciter was replaced by a new short deflector, and the second and third electrostatic deflectors were replaced by new magnetic channels. Thanks to the change of the radius from which the extraction takes place from 50 cm to 52.4 cm it was possible to reduce the electric field of the deflectors required for extraction to approximately −140 kV/cm. Based on the experience of other cyclotron laboratories, deflectors with such parameters can probably be realized. For the proton modes with the highest electric field, the operation of the deflectors can be expected to be at the limit of their capabilities. For the other ion modes, where the required electric field is lower, the proposed deflectors should work with a sufficient voltage and electric field reserve.

Thanks to the precise measurement of the cyclotron magnetic field it was possible to successfully optimized the horizontal placement of the acceleration chamber and minimize the negative influence of the first harmonic disturbance component in magnetic field. The residual component of this disturbance can now be compensated with the newly developed harmonic coils, which were incorporated into the accelerator's magnetic structure during the shutdown in 2022 and are now being continuously tested.

The positive effect of the new harmonic coils is evident from simulations with positive ions, especially during the separation of orbits at the extraction radius, when by using a suitable combination of currents it is possible to achieve such a separation of the last orbits that the losses on the septum of the first deflector with a thickness of 0.1 mm are minimized and the transparency of the deflector reaches 90 %.

For negative beam experiments, by choosing a different combination of coil currents, it is possible to reduce the influence of the first harmonic disturbance component of the magnetic field to the extent that the acceleration region can be extended to higher radii than previously possible. By verifying the simulated negative hydrogen mode of 36.4 MeV at the actual accelerator, it was possible to accelerate the beam to a radius of 52 cm and extract it with a mean energy of 38.2 MeV, corresponding to a 5 % increase in the cyclotrons output energy. The precise determination of the beam energy will be done by measuring the parallel reactions of the control copper foils in the future.

In future work, optimization of the magnetic channels will continue in adaptation of the final design of the entire extraction system to lower energy regimes, when the cyclotron magnetic field is significantly lower. It may be necessary to develop a modular system

allowing each of the magnetic channels to be assembled so that its resulting magnetic field reflects the lower magnetizing field of the cyclotron. This could be achieved, for example, by constructions that allow to assemble the final ferromagnetic rod of the magnetic channel from smaller rods of size, for example 1×1 mm enclosed in an adaptive case.

The focusing gradient of the second deflector decreases with decreasing electric field and for particles of lower energies, when the necessary extraction electric field is low, it may be advantageous to create a customized deflector with a different shape of the septum and the high voltage electrode providing higher electric field gradient than the new Deflector I proposed in this work.

If the new extraction system can be implemented at the lower limit of the expected extraction efficiency, i.e. close to the value of 70 %, this would mean an increase in the extraction efficiency 4–10 times, depending on the type of accelerated particles. In such a case, it would be possible to revive the project of axial beam injection into the central region of the accelerator and replace the existing ion source with an external one. This exchange would make it possible to significantly expand the number of accelerated particles and allow full use of the potential of the U-120M cyclotron.

References

[1] K. J. LeCouteur A. V. Crewe. "Extracted Proton Beam of the Liverpool 156-Inch Cyclotron". In: *Rev. Sci. Instr* 26 (1955), p. 725.

[2] SENIS AG. *Teslameters*. 2023. URL: https://www.senis.swiss/magnetometers/#teslameter-digital.

[3] Alenickij. "Magnetic field of the isochronous cyclotron U-120M with deep energy variation." In: *JINR 9-10627, in russian* (1977).

[4] J.G et.al. Alenickij. "Isochronous cyclotron with deep energy variation." In: *JINR 9-10382, in russian* (1977).

[5] J.G. Alenickij. "Magnetic field of the isochronous cyclotron U-120M". In: *JINR P9-10091, in russian* (1976).

[6] V.N. Anosov et al. "Control system of the isochronous cycklotron U-120M". In: *JINR, U-120M conferenc Ceske Budejovice 1973, in russian* (1973).

[7] Autodesk. *Autodesk Inventor*. URL: https://www.3ds.com/products-services/simulia/products/opera/.

[8] Edmund Bakewicz et al. "A new extraction system for the upgraded AIC-144 cyclotron". In: *Nukleonika* 46.2 (Jan. 2001), pp. 51–57. URL: http://www.ichtj.waw.pl/ichtj/nukleon/back/full/vol46_2001/v46n2p051f.pdf.

[9] C. Baumgarten et al. "A beam profile measurement in the ACCEL 250MeV medical proton cyclotron". In: *Nuclear Instruments and Methods in Physics Research* (Dec. 2006). DOI: 10.1016/j.nima.2006.09.077.

[10] R. Běhal. *Private communication*. 2022.

[11] O. N. Borisov et al. "New beam extraction system for the AIC-144 cyclotron". In: (May 1998).

[12] Canada's particle accelerator centre. *TRIUMPH*. https://www.triumf.ca/research-program/research-facilities/main-cyclotron-beam-lines.

[13] June 1979 CERN Courier Volume 19 Number 4. *Dubna isochronous cyclotrons in operation*. 1979. URL: https://cds.cern.ch/record/1730440/files/vol19-issue4-p158-e.pdf.

[14] F Chautard. "Beam dynamics for cyclotrons". In: (2006). DOI: 10.5170/CERN-2006-012.209. URL: http://cds.cern.ch/record/1005052.

[15] R. Cieslik. "Operation regime of AIC-144 cyclotron for delivering 60 MeV proton beam to the radiotherapy of eye melanoma". In: *Instytut fizyki jadrowej, Report No.2057/AP* (2012).

[16] M. Cihak. *DURYCNM software – Beam dynamics simulator for U-120M cyclotron*. NPI ASCR, Cyclotron laboratory, 2022.

[17] M. Cihak. *Isochronous cyclotron new magnetic measurements methodics and results*. JINR P9-85-707, in russian, 1985.

[18] M. Cihak. *Mathematical model of the U-120M cyclotron*. JINR D9-89-708, in russian, 1989.

[19] M. Cihak, J. Lacman, and J. Stursa. *New control system for the isochronous cyclotron U-120M*. Proceedings 15th ICCA, 1999. URL: https://cds.cern.ch/record/460458.

[20] M. Cihak, O. Lebeda, and J. Stursa. *Beam dynamics simulation in the isochronous cyclotron U-120M*. Proceedings 18th ICCA, 2007.

[21] M. Cihak and J. Stursa. *Mathematical simulation and analysis of the cyclotron U-120M*. Nuclear Physics Institute Řež near Prague Biennial Report, 2001.

[22] D. J. Clark. "Ion sources for cyclotrons". In: *Proceedings of the 9th International Conference on Cyclotrons and their Applications Caen, France* (1981).

[23] J.N. Denisov, A.N. Ljubenko, and M. Cihak. "The system of automatic beam phase measuring and control for the isochronous cyclotrons". In: *Proceedings of the 7th International Conference on Cyclotrons and their Applications* (1975). DOI: https://doi.org/10.1007/978-3-0348-5520-4_120.

[24] Cyclotron department. *Nuclear Physics Institute ASCR, website*. 2023. URL: http://www.ujf.cas.cz/en/departments/department-of-accelerators/cyclotron/.

[25] C. Oliver *et* al. "Optimizing the Radioisotope Production with a Weak Focusing Cyclotron". In: *Proceedings of the 2013 Cyclotron Conference* 43 (2013), p. 429.

[26] E. Forringer. *Phase Space Characterization of an Internal Ion Source For Cyclotrons*. 1979. URL: https://groups.nscl.msu.edu/nscl_library/Thesis/Forringer,%5C%20Edward%5C%20Russell.pdf.

[27] E. R. Forringer and Henry G. Blosser. "Using the orbit tracking code Z3CYCLONE to predict the beam produced by a cold cathode PIG ion source for cyclotrons under DC extraction". In: *Conf. Proc. C* 0505161 (2005). Ed. by Charlie Horak, p. 1297.

[28] Pauli Heikkinen. "Injection and extraction for cyclotrons". In: *CAS CERN 94/01* (1994). http://cds.cern.ch/record/398439/files/p819.pdf.

[29] B. Holzer. *Introduction to Transverse Beam Optics, Twiss Parameters and Lattice Design*. https://www.cockcroft.ac.uk/wp-content/uploads/2014/12/Neil_2.pdf.

[30] LakeShore Inc. *HGT3030 Hall sensor*. 2023. URL: https://www.lakeshore.com/products/categories/specification/magnetic-products/hall-(magnetic)-sensors/inas-and-gaas-hall-sensors.

[31] Paul Scherrer Institute. *Villigen, Switzerland*. https://www.psi.ch/en/media/the-psi-proton-accelerator.

[32] National Instruments. *NI LabView Manual*. URL: https://www.ni.com/docs/en-US/bundle/labview/page/lvhelp/labview_help.html.

[33] H.L. Hagedoorn J. Botman. "Extraction from cyclotrons". In: *CERN document server* (1996). https://cds.cern.ch/record/399427/files/p169.pdf. DOI: DOI:10.5170/CERN-1996-002.169.

[34] S. Yamashita J. Kokame. “Electrostatic Deflection of a Cyclotron Ion Beam.” In: *J. Phys. Soc. Japan* 11 (1956), p. 332.

[35] JanasCard. *AD24USB*. 2023. URL: http://www.janascard.cz/aj_Vyrobky.html.

[36] W. Joho. “Extraction from medium and high energy cyclotrons”. In: *Proceedings of the Fifth International Cyclotron Conference* (1971). https://doi.org/10.1088/0031-9112/22/9/019.

[37] F. Krizek et al. “Irradiation setup at the U-120M cyclotron facility”. In: *Nuclear Instruments and Methods in Physics Research A* 894 (June 2018), pp. 87–95. DOI: 10.1016/j.nima.2018.03.066.

[38] J. Kroulík. *Private communication*. 2022.

[39] Jeffrey Lagarias et al. “Convergence Properties of the Nelder–Mead Simplex Method in Low Dimensions”. In: *SIAM Journal on Optimization* 9 (Dec. 1998), pp. 112–147. DOI: 10.1137/S1052623496303470.

[40] E.O. Lawrence and M.S. Livingston. “ The Production of High Speed Light Ions Without the Use of High Voltages”. In: *Phys. Rev.* 40.1 (1932), p. 9. DOI: http://dx.doi.org/10.1103/PhysRev.40.19.

[41] Group3 Technology Limited. *Digital teslameters/gaussmeters*. 2023. URL: https://www.group3technology.com/digital-teslameters-gaussmeters.

[42] John J. Livingood. *Principles of Cyclic Particle Accelerators*. D. Van Nostrand Reinhold Inc.,U.S., 1961. ISBN: 978-0442048228.

[43] M. S. Livingston. “The History of the Cyclotron”. In: *Proceedings of the 7th International Conference on Cyclotrons and their Applications, Zürich, Switzerland* (1975).

[44] J . H. Manley M. J . Jakobson. “Phase Properties of the Deflected Ion Beam from a Fixed Frequency Cyclotron.” In: *Phys. Rev.* 95 (1954), p. 600.

[45] MagWeb. *Properties of Soft Magnetic Materials*. URL: https://www.magweb.us/wp-content/uploads/2021/08/SMAG-Handook-Version-7.pdf.

[46] MATLAB. *version 9.2.0.538062 (R2017a)*. Natick, Massachusetts: The MathWorks Inc., 2010.

[47] T. Matlocha. “Modification of a classical penning ion source operating mode for sub-femtoampere beams at the U-120M cyclotron”. In: *AIP Conference Proceedings* (Sept. 2018). DOI: 10.1063/1.5053321. URL: https://aip.scitation.org/doi/pdf/10.1063/1.5053321.

[48] T. Matlocha and F. Krizek. “Ultra-low intensity proton beams for radiation response related experiments at the U-120M cyclotron”. In: *Acta Polytechnica CTU Proceedings* 14 (May 2018), p. 21. DOI: 10.14311/APP.2018.14.0021.

[49] M. McMillan. “The Synchrotron–A Proposed High Energy Particle Accelerator”. In: *Phys. Rev.* 40.1 (1945), p. 9.

[50] Alenickij J.G. Zaplatin N.L. Morozov N.A. “Tolerances of the U-120M magnetic system elements .” In: *JINR 9-10090, in russian* (1976).

[51] M. Nakao et al. “The multi particle simulation for the cyclotron NIRS-930”. In: *Proceedings of HIAT2015, Yokohama, Japan* (2015).

[52] MIT Course notes. *Runge-Kutta Methods*. 2023. URL: https://web.mit.edu/10.001/Web/Course_Notes/Differential_Equations_Notes/node5.html.

[53] Wikipedia online. *Magnetic reluctance*. 2023. URL: https://en.wikipedia.org/wiki/Magnetic_reluctance.

[54] E. N. Khaprov. P. P. Dmitriev N. N. Krasnov. "The Problem of Beam Deflection in a Cyclotron." In: *Soviet J. Atomic Energy 3* 7 (1957), p. 778.

[55] "Particle Source Emission Model Overview, The MIT Kavli Institute". In: (2023). URL: https://space.mit.edu/RADIO/CST_online/mergedProjects%20/3D/special_overview/special_overview_particle_source_emission_overview.htm.

[56] D Poe et al. "Status of Electrostatic Deflector at NSCL K1200 Cyclotron". In: (1999). URL: https://cds.cern.ch/record/460495.

[57] IAEA Office of Public Information and Communication. *Increasing Radiopharmaceutical Production with Cyclotrons*. 2022. URL: https://www.iaea.org/newscenter/news/increasing-radiopharmaceutical-production-with-cyclotrons.

[58] Scrivens R. "Electron and Ion Sources". In: *Cern Accelerator School, Varna,* (2010). URL: https://indico.cern.ch/event/73157/contributions/2076035/attachments/1039879/1481922/Scrivens-web.pdf.

[59] Rutgers University, Department of Physics and Astronomy. *Koeth 12-Inch cyclotron website*. http://koethcyclotron.org/?page_id=390.

[60] J. R. Schubert. *Extending the Feasibility Boundary of the Isochronous Cyclotron*. Ph.D. Dissertation, Michigan State University, 1997.

[61] P K Sigg. "Rf for cyclotrons". In: (2006). DOI: 10.5170/CERN-2006-012.231. URL: http://cds.cern.ch/record/1005053.

[62] V. Smirnov. *Central Region Design in a Compact Cyclotron*. Physics of Particles and Nuclei Letters, 2018. DOI: 10.1134/S1547477119010114.

[63] V. Smirnov and S. B. Vorozhtsov. "Modern compact accelerators of cyclotron type for medical applications". In: *Physics of Particles and Nuclei* 47.5 (Sept. 2016), pp. 863–883. DOI: 10.1134/s1063779616050051.

[64] V. L. Smirnov. "The Cyclotron and Its Modeling". In: *Physics of Particles and Nuclei* 52.5 (Sept. 2021), pp. 913–996. DOI: 10.1134/S106377962105004X.

[65] B H Smith and H A Grunder. "Electrical Design of Electrostatic Deflectors for Sector-Focused Cyclotrons". In: (1963). DOI: 10.5170/CERN-1963-019.304. URL: https://cds.cern.ch/record/862772.

[66] 3DS Dassault Systemes. *Opera electromagnetic and electromechanical simulation*. URL: https://www.3ds.com/products-services/simulia/products/opera/.

[67] 3DS Dassault Systems. "CST Studio Suite". In: (). URL: https://www.3ds.com/products-services/simulia/products/cst-studio-suite/.

[68] Marc Tavlet and H.G.J. Van Der Burgt. "Radiation resistance and other safety aspects of high-performance plastics by ERTA". In: *CERN TIS* (Aug. 1994). DOI: 10.5170/cern-1994-007.157.

[69] L.H. Thomas. "The Paths of Ions in the Cyclotron I. Orbits in the Magnetic Field". In: *Phys. Rev.* 54.8 (1938), p. 580. DOI: https://doi.org/10.1103/PhysRev.54.580.

[70] Z. Trejbal. "The beam extraction system and the axial injection for the U-120M cyclotron." In: *JINR 9-10388, spec. 01.04.13, Self-report in russian* (1977).

[71] Smirnov V. and Vorozhtsov B. "Modification of the central region in the Riken AVF cyclotron for acceleration at the h=1 RF harmonic". In: *Proceedings of the 10th International Conference on Cyclotrons and their Applications Lanzhou, China* (2010).

[72] S. Vorozhtsov V. Smirnov. "SNOP – beam dynamics analysis code for compact cyclotrons". In: *RuPAC 12* (Sept. 2012). DOI: DOI:10.13140/2.1.2035.9684.

[73] V I Veksler. "A new method of acceleration of relativistic particles". In: *J. Phys.* 9 (1945), pp. 153–158. URL: https://cds.cern.ch/record/109364.

[74] John B. Vincent et al. "The Ionetix ION-12SC Compact Superconducting Cyclotron for Production of Medical Isotopes". In: *21st Int. Conf. on Cyclotrons and Their Applications (Cyclotrons'16), Zurich, Switzerland, September 11-16, 2016* (Jan. 2017), pp. 290–293. DOI: 10.18429/jacow-cyclotrons2016-thb02. URL: https://accelconf.web.cern.ch/cyclotrons2016/export/THB02-ris.htm.

[75] H. Vogt-Nilsen. "Expansions of the characteristic exponents and the Floquet solutions for the linear and homoganous second order differential equation". In: *MURA - 118* (1956).

[76] E. Harms W. Barletta L. Spentzouris. "Emittance". In: *US Particle Accelerator School Notes* (). https://uspas.fnal.gov/materials/10MIT/Emittance.pdf.

[77] Z. Tang W. Chou J.R. Lackey. "Some physics issues of carbon stripping foils". In: *Particle Accelerator Conference, 2007. PAC. IEEE* (2007). DOI: DOI:10.1109/PAC.2007.4440862.

[78] S. Zaremba W. Kleeven. "Cyclotrons: Magnetic Design and Beam Dynamics". In: (2015). https://arxiv.org/pdf/1804.08961.pdf.

[79] Helmut Wiedemann. *Particle Accelerator Physics*. Springer-Verlag Berlin Heidelberg, 2007. ISBN: 978-3-540-49045-6. DOI: 10.1007/978-3-540-49045-6.

[80] H.A. Willax. "Proposal for a 500 MeV Isochronous Cyolotron with Ring Magnet". In: *3rd International Conference on Sector-focused Cyclotrons and Meson Factories* (1963). http://cds.cern.ch/record/862785/files/p386.pdf.

[81] C. Wouters et al. "Central region studies of the 250 MeV SC cyclotron for proton therapy". In: (2009).

[82] S Zaremba. "Magnets for cyclotrons". In: (2006). DOI: 10.5170/CERN-2006-012.253. URL: https://cds.cern.ch/record/1005055.